

Diagnosis of Gas Insulated Switchgear Based on Detection of CF₄ as an SF₆ Decomposition Gas

パンシリ, ニサルト

<https://hdl.handle.net/2324/4496075>

出版情報 : 九州大学, 2021, 博士 (工学), 課程博士
バージョン :
権利関係 :

**Diagnosis of Gas Insulated Switchgear Based on
Detection of CF₄ as an SF₆ Decomposition Gas**

SF₆分解ガス CF₄の検出によるガス絶縁開閉器の診断

Nisarut Phansiri

**Graduate School of Information Science and Electrical Engineering
Kyushu University**

2021

**Diagnosis of Gas Insulated Switchgear Based on
Detection of CF₄ as an SF₆ Decomposition Gas**

SF₆分解ガス CF₄の検出によるガス絶縁開閉器の診断

Nisarut Phansiri

**Graduate School of Information Science and Electrical Engineering
Kyushu University**

2021

Contents

Contents	i
Chapter 1	1
Introduction	1
1.1 Trends in the world electricity consumption	1
1.2 Gas-insulated switchgear (GIS)	5
1.3 Failures and possible defects in GIS	12
1.4 GIS diagnosis methods	13
1.5 Diagnosis techniques for partial discharge in GIS	15
1.6 SF₆ decomposition detection methods	17
1.7 Chemical detection-based GIS diagnosis	20
Chapter 2	21
Research objective and overview concepts	21
2.1 Objective	21
2.2 Decomposition product effect and why CF₄ is the detection target	22
2.2 Related studies	28
2.2.1 Nanomaterial-based gas sensor.....	29
2.2.2 Non-thermal plasma applications	29
2.3 Direct CF₄ detection	30
2.4 Indirect CF₄ detection	31
2.5 The details of each chapter in the dissertation	32
Chapter 3	34
Direct CF₄ detection by using nanomaterial-based gas sensors	34
3.1 Introduction	34
3.2 Nanomaterial-based gas sensors	34
3.2.1 Tin oxide (SnO ₂) and zinc oxide (ZnO)	34
3.2.2 Working principle of semiconducting nanomaterial gas sensor	36
3.2.3 Carbon nanotube (CNT)	38

3.3 Dielectrophoresis.....	38
3.4 DEP trapping based fabrication of nanomaterial gas sensor	40
3.6 Experimental apparatus for gas sensor performance	52
3.7 Effect of transducer material and operating temperature.....	55
3.8 Effect of nanoparticle suspension concentration	58
3.9 Reproducibility of SnO ₂ gas sensor	58
3.10 Discussion	61
3.11 Summary.....	62
Chapter 4	63
Indirect CF₄ detection by using nonthermal plasma application.....	63
4.1 Introduction.....	63
4.2 Experiments.....	68
4.2.1 DBD reactor and gas treatment chamber	68
4.2.2 Test gas.....	69
4.2.3 Analysis of generated CO and CO ₂	70
4.2.4 Experimental procedure	70
4.3 Gas analysis preparation.....	71
4.3.1 Determination of CO ₂ concentration	71
4.3.2 Determination of CO concentration.....	74
4.3.3 CO sensor performance under SF ₆ background gas and SO ₂ influence	76
4.3.4 DBD plasma characterization	79
4.4 Results	83
4.4.1 DBD plasma characteristics.....	83
4.4.2 Generation of CO ₂ and CO by DBD.....	85
4.4.3 Electrochemical CO sensor performance	88
4.5 Discussion	92
4.5.1 CF ₄ to CO and CO ₂ conversion rates.....	92
4.5.2 CF ₄ conversion selectivity	92
4.5.3 Effect of decomposition gases on the damage of the sensor	93
4.5.4 Prospects for on-site GIS diagnosis application	94
4.6 Summary.....	95

Chapter 5	96
Gas sensor fabricated by two-step dielectrophoretic assembly	96
5.1 Introduction.....	96
5.2 Nitrogen Oxide (NO₂)	96
5.3 Experiment	97
5.4 Result and discussion.....	100
5.5 Perspective for the detection of CF₄ and CO	110
5.6 Summary.....	110
Chapter 6	112
Conclusion	112
References.....	116
Acknowledgements	133

Chapter 1

Introduction

1.1 Trends in the world electricity consumption

Between 1870 and 1914, the second industrial revolution, the world electricity consumption has been increasing continuously. Electricity is one of the essential keys for driving economic growth. It has also become a part of modern life, and we cannot think of a world without it. Future energy demands should be met and improved efficiently and securely. According to the report of world energy consumption in the last two decades (2000-2019) shown in Figure 1.1 [1], it increases 3% per year on average worldwide. Figure 1.1a shows overall electric consumption in the world. Electricity consumption in Asia has increased, which is the highest when compared with other continents revealed Figure 1.1b. Figure 1.1c shows that China is the country where uses the highest electricity in the world. It has been predicted that the worldwide energy consumption in 2025 and 2030 becomes 665.4 and 721.6 quadrillions of British thermal units (BTU), respectively [2]. Another report estimates the average annual percent change for 2000–2030, around 2% per year. According to the notice of electricity demand by sectors [3], including industry, residential, service, transport, other final uses, and power service, it has increased in all sectors as shown in Figure 1.2 [3]. The trends indicate the growth of the power system in the future.

Normally, the power system, concluding generation, transmission, and distribution, is one of the most complex networks in modern society. The rapid evolution of its size and diversity, as well as the emergence of the smart grid, has brought many challenges including stability issues and the subsequent occurrence of blackouts. A summary of major blackouts occurred in recent years is presented in Table 1.1 [4]. These data show the effect of blackout, failure of the system, in the term of affected people and loose cost during the outage situation. For example, in the year 2012 in India, 670 million people were affected, and the 6000 million Dollars of the loose cost was estimated during the 2-8 h of blackout time. While the year 2003 in North America, the loose cost was estimated over 10000 million Dollars in North America. During 5-72 h of blackout time. However, after the outage situation, they tried to improve the system for increasing reliability. Typically, reliability of system is referred to standard such as IEEE Std. 1366-

1998 (Trial Use Guide for Electric Power Distribution Reliability Indices). Union for the Coordination of Transmission of Electricity (UCTE) shows the blackout classification in Table 1.2 [5], which is calculated from the population and the base of power corresponding to the whole system.

Table 1.3 [6] shows 66 surveyed major power systems blackouts in some parts of the world from 2011 to 2019. The survey is not comprehensive of all the power systems blackouts in the world but is an excellent indicative tool in analyzing the causes of power system blackouts. It can be seen that the highest number of blackouts was due to abnormal weather conditions such as severe winds and heavy storms, and trees are falling on the transmission line. However, bad weather conditions cannot be predicted with absolute certainty, therefore having a forecast of them and an improved power system monitoring a control platform can significantly safeguard power systems against such events. The second failure cause is faulty equipment or human error, shown at 31.8%. Apparently, the electrical apparatuses need to be improved continuously as well as power system protection.

Nowadays, there is an electrical power substation everywhere. The power substation is one of the essential parts of power system reliability. The study on the power substation and the equipment installed inside should be necessary for power system improvement. As described above, the power system needs a high degree of reliability. Therefore, the electrical equipment will be essential to make high quality and capacity.

For these reasons, the electrical apparatus diagnosis is required for the stability and reliability of the system. In this research, I focused on gas-insulated switchgear (GIS) diagnosis because of the trends of increasing GIS continuously, and GIS has many advantages. I would explain the details of GIS in the next section.

Moreover, taking environmental protection into account is also great attention. Because some ecological problems, such as acid rain, the greenhouse effect, and global warming, have already become a severe global problem, such as gas-insulated equipment, which is commonly used in the power system. Leak or emission of insulated gases affects the environment. Therefore, during the power system development, environmental influence is also a critical topic concerned in the future.

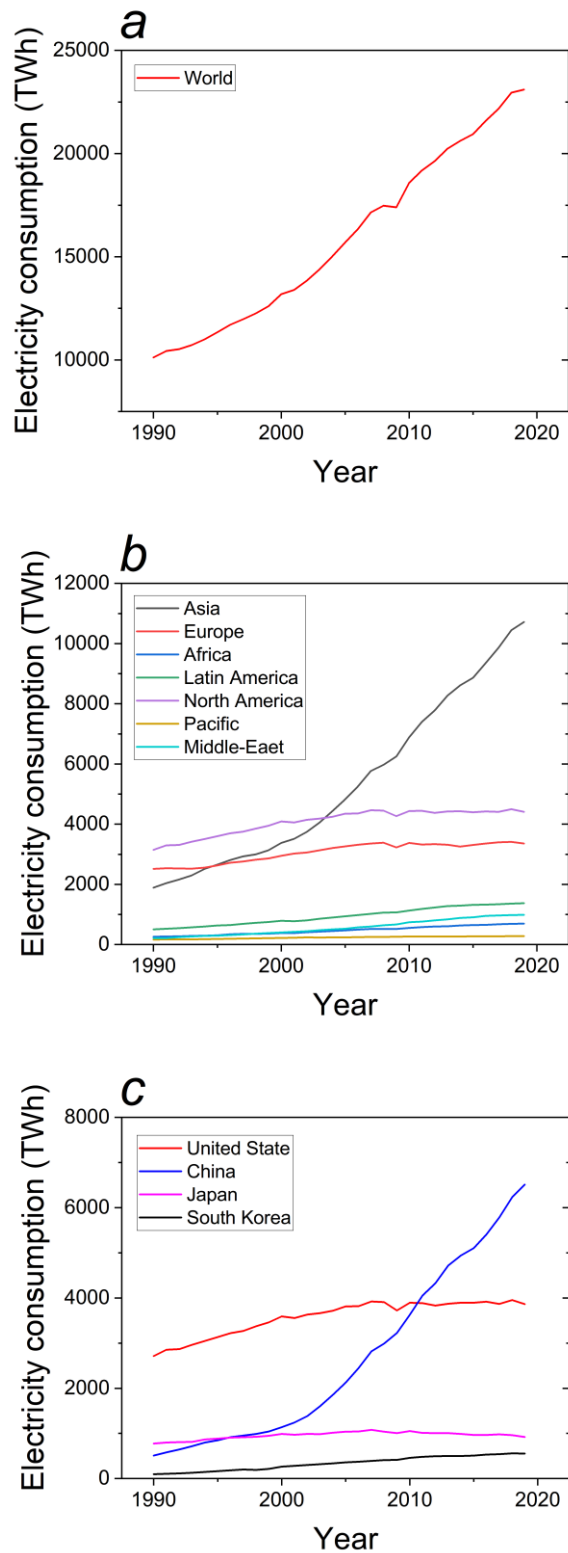


Figure 1.1. Electricity consumption in worldwide (a), continent (b), counties (c). (Data from World Power consumption, Electricity consumption, Enerdata [1])

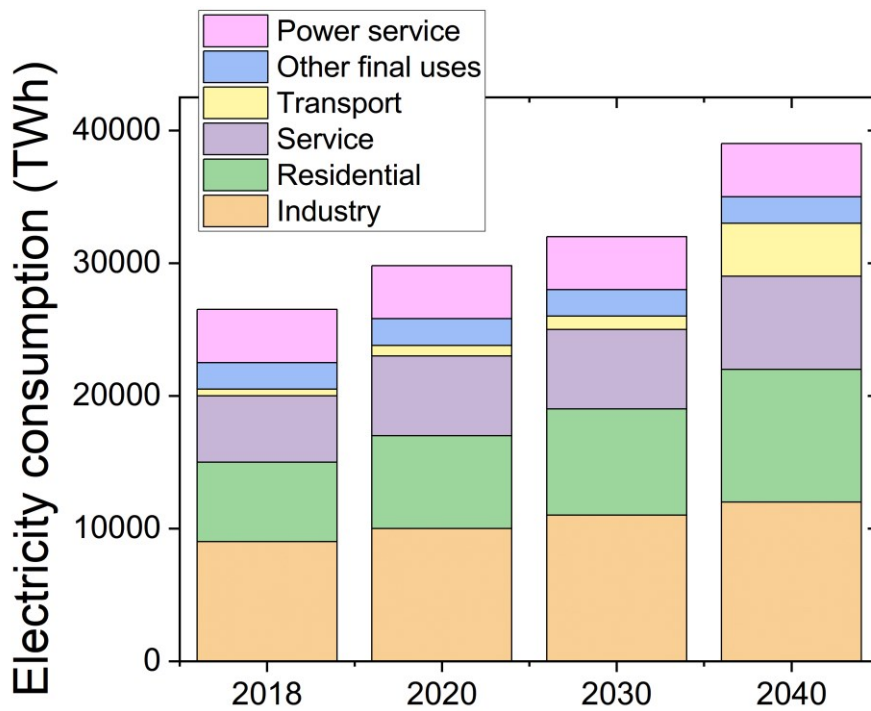


Figure 1.2. World electricity consumption by sectors. (Data from Electricity, World Energy Outlook 2019, Analysis - IEA [3])

Table 1.1. List of major blackouts since 2003 [4]

Blackout location	Date	People affected (Millions)	Loss of load (MW)	Estimated cost (Million Dollars)	Time duration	Improvement after blackout
Turkey	31 March 2015	70	32.2	700	7 h	Improve overload monitoring and protection of transmission line
India	30-31 July 2012	670	48	6000	2-8 h	New-load shedding strategies
Italy	28 September 2003	57	24	1200	5-9 h	Implement Day-Ahead Congestion Forecast (DAFC)
North America	14-15 August 2003	50	61.8	Over 10,000	5-72 h	Introduce higher reliability standards for North American electricity industry
London	28 August 2003	0.5	72.4	N.A.	> 30 mins	Enhance cooperation between utility companies

Table 1.2. Disturbance severity classification UCTE [5]

Classification (Level)	Severity (System – minute)	Interpretation
0	<1	Acceptable
1	1-10	Not severe
2	10-100	Severe
3	100-1000	Very severe
4	>1000	Catastrophic

Table 1.3. Analysis on blackouts around the globe and their percentage from 2011 to 2019 [6]

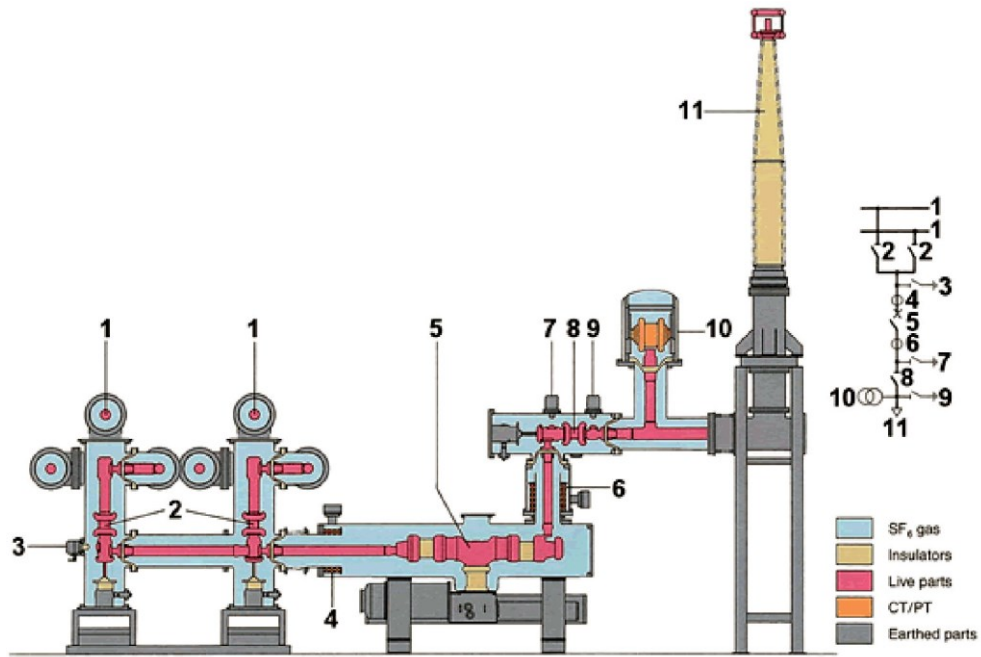
Blackout case	Number recorded	% of the recorded number
Weather/Trees	33	50
Faulty equipment or human error	21	31.8
Vehicle/Accidents	7	10.6
Animal	1	1.5
Over demand	4	6.1
Total	66	100

1.2 Gas-insulated switchgear (GIS)

At first, in this dissertation, the abbreviation “GIS” is used as an abbreviation of “gas-insulated switchgear.” There are two definitions used in standards: “Gas Insulated Switchgear” for International Electrotechnical Commission (IEC) and “Gas Insulated Substations” for Institute of Electrical and Electronics Engineers (IEEE).

Gas-insulated switchgear (GIS) is a compact grounded metallic housing in which multi-component assembly such as buses, switches, and circuit breakers are enclosed. In a GIS vessel, SF₆ is filled as the primary insulating medium. The typical structure of GIS equipment is schematically illustrated in Figure 1.3 [7].

For small sizing, typically, sulfur hexafluoride (SF₆) is used as an insulating gas due to its excellent insulation properties, such as that the breakdown voltage is higher than the air around three times, SF₆ can be heated to 500 °C without decomposition in the absence of a catalytic material, non-flammable, hydrogen, chlorine and oxygen have no reaction on it, insoluble in water, and not reacted by acids. Some physical parameters of SF₆ are listed in Table 1.4 [8-9]



- | | |
|--------------------------------|-------------------------|
| 1: Busbar | 2: Disconnector |
| 3: Maintenance earthing switch | 4: Current transformer |
| 5: Circuit breaker | 6: Current transformer |
| 7: Maintenance earthing switch | 8: Disconnector |
| 9: Earthing switch | 10: Voltage transformer |
| 11: Bushing | |

Figure 1.3. Sectional view of a 550 kV-class GIS [7].

Table 1.4. Some properties of SF₆ [8-9]. The asterisk *) denotes quantities that approximately pressure independent in the range $P \leq 700$ kPa.

Density (gas, 20 °C, 0.1 MPa) Density (liquid, 0 °C, 1.27 MPa)	6.07 kg/m ³ 1560 kg/m ³
Dynamic viscosity (20 °C, *)	1.06×10 ⁻⁵ kg/m/s
Thermal conductivity (20 °C, *)	0.0155 W/m/K
Velocity of sound (20 °C, *)	134 m/s
Isentropic exponent (20 °C, *)	1.08
Critical temperature	45.55 °C
Critical pressure	3.759 MPa
Critical density	740 kg/m ³
Special heat Cp (gas, 20 °C, *) (liquid, 20 °C, *)	524 J/kg/K 562 J/kg/K
Heat of sublimation	153,200 J/kg
Heat of melting	34,370 J/kg
Heat of vaporization (20 °C)	62,540 J/kg
Refractive index (20 °C, 0.1 MPa)	1.00073
Relative permittivity (20 °C, *)	1.0021
Loss tangent (gas, 20 °C) Loss tangent (liquid, -51 °C)	<5×10 ⁻⁶ <1×10 ⁻³
Pressure reduced critical breakdown field (20 °C, *)	89 V/m/Pa
Effective ionization coefficient	$\alpha = A \cdot p [E/p - B]$ α 1/m A = 2.8×10 ⁻² 1/V B = 89 V/m/Pa

Recently, the GIS market is moderately fragmented. Some of the key companies in the market include ABB Ltd, Siemens, Schneider Electric SE, General Electric Company, Mitsubishi Electric, Eaton Corporation PLC, and Toshiba International Corporation [10]. In the last two decades, the evolutionary development of gas-insulated

switchgear has resulted in higher integration of several new technologies to enhance performance and reliability by reducing defects, having more compact designs. These developments enable to reduce intervals and cost for the maintenance. Gas-insulated systems, such as gas-insulated lines and switchgear (GIL and GIS), are widely used in the electric industry to transmit and control bulk power, respectively. The concept of high voltage GIS with SF₆ has proved itself in several thousands of installations worldwide. It offers the following outstanding advantages: [11, 12]

- Minimal spacer requirements
- Complete protection against contact with human and animal
- Protection against pollution
- Free choice of the installation site
- Protection of the environment
- Longevity, lifetime > 50 years

Gas-insulated switchgear, components, and related equipment fall under a large number of standards. Both IEC and IEEE standards have standards for GIS, circuit breakers, switches, bushings, testing, instrument transformers, controls, cabinets, pressure vessels, and so on. Some of the current standards most relevant to GIS are as follows:

- IEEE C37.122: IEEE Standard for Gas-Insulated Substations
- IEEE C37.123: IEEE Guide to Specifications for Gas-Insulated, Electric Power Substation Equipment
- IEEE C37.122.1: IEEE Guide for Gas-Insulated Substations
- IEEE C37.1300: Cable Connections
- IEC 62271-203: Gas-Insulated Metal-Enclosed Switchgear for Rated Voltages above 52 kV
- IEC 62271-1: Common Specifications
- CIGRE Brochure 125: User Guide for the Application of Gas-Insulated Switchgear (GIS) for Rated Voltages of 72.5 kV and Above

Figure 1.4 [11] shows the percentage evolution and development of the different high voltage substations in the market from 1960 to 2020. If GIS and air-insulated switchgear (AIS) are compared in the needed space for the same function, the space reduction by GIS is in the ratio of 1:5. That means less than 20% of the area of AISs is

needed to install a GIS. For example, Figure 1.5 [13] shows a comparison of the installed area between AIS and GIS (ABB's ELK-3 GIS) of 380 kV, Pradella CH, Switzerland.

In 2007, more than 20,000 bays in over 2,000 substations were installed worldwide, in all kinds of environmental conditions and with the whole spectrum of voltage and current rating. Highly integrated switchgear (HIS) is a compact switchgear solution for a rated voltage of up to 550 kV. HIS is mainly used for the renewal or expansion of air-insulated outdoor and indoor substations. With the HIS solution, all electrical equipment is accommodated in compressed gas-tight enclosures and a minimum number of independent gas compartments. This makes the switchgear extremely compact. Gas-insulated modules have recently been seen at all voltage levels up to 550 kV as intermediaries between GIS and AIS. They are suitable for the following categories of application: standardization and optimization of new substations and/or extension in an extensive network, reconstruction or refurbishment of AIS with operational constraints and/or space limitation, and AIS extension with space limitation [11].

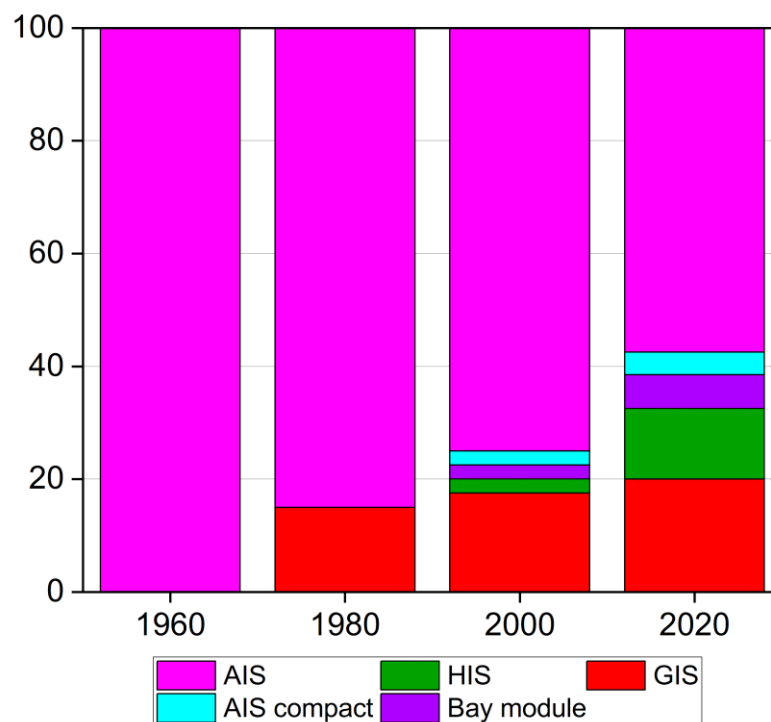


Figure 1.4. Percentage evolution and development of HV substation in the market. (Data from Technological progress in high-voltage gas-insulated substation [11]).

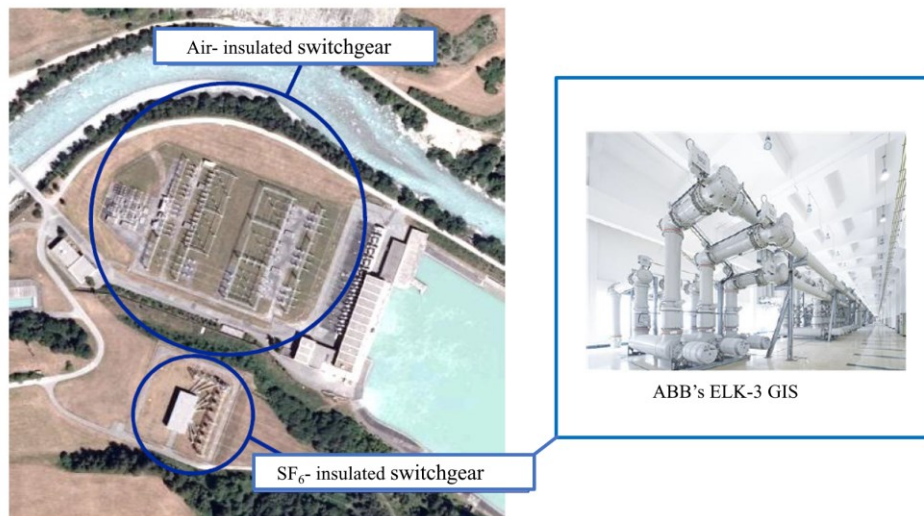


Figure 1.5. Comparison of the installed area between AIS and GIS 380 kV Data from ABB [13]).

The switchgear only makes a minor contribution to the total global warming potential of a representative urban distribution grid. On the contrary, other grid components such as cables and transformers play a decisive role regardless of whether AIS or GIS technology is used. Figure 1.6 [11] shows an overview of the percentage of environmental impact categories examined in a study at the switchgear level, and the details of environmental impact are described in [14]. It is based on a representative mix of all switchgear types in the MV range. A clear advantage for GIS compared to the AIS area is also shown regarding global warming potential, except the SF₆ emission. SF₆ gas is one of the most substantial human-made “greenhouse” gases, where its global warming potential (GWP) is estimated to be approximately 22,800 times larger than that of carbon dioxide (CO₂) gas. Table 1.5 shows the atmospheric lifetime and GWP at different time horizons for SF₆ and CO₂. It was estimated that the emissions would reach 4270 ± 1020 ton in 2020 [15], and the concentration of SF₆ in the atmosphere increased by 20% from 2010 to 2015 [16]. For this reason, many researchers have issued eco-friendly gases to replace SF₆. Beroual and Haddad [17] report the literature review. The review reports the main properties of candidate gases that are being investigated; in particular, natural gases (dry air, N₂, or CO₂) and polyfluorinated gases, especially Trifluoroiodomethane (CF₃I), Perfluorinated Ketones, Octafluorotetra-hydro furan, Hydrofluoroolefin (HFOs), and Fluoronitriles are presented, and their strengths and weaknesses are discussed with an

emphasis on their dielectric properties (especially their dielectric strength), GWP, and boiling point with respect to the minimum operating temperature for HV power network applications.

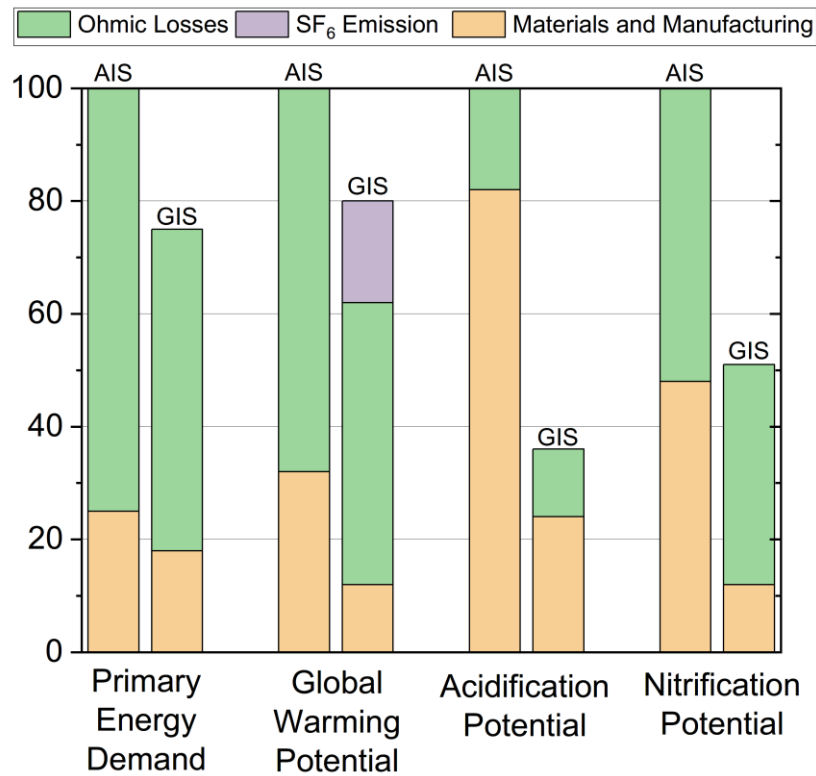


Figure 1.6. Environmental impact of AIS and GIS. The vertical axis indicates the percentage of environmental impact with categories in horizontal axis (Data from Technological progress in high-voltage gas-insulated substation [11])

Table 1.5. Lifetime and GWP at different time horizon for SF₆ and CO₂ [17]

Gas	Lifetime (Years)	Global Warming Potential (GWP) for Given Time Horizon		
		20 years	100 years	200 years
CO ₂	30-95	1	1	1
SF ₆	3,200	16,300	22,800	32,600

1.3 Failures and possible defects in GIS

GIS has been operated for more than 50 years with a low failure rate due to high reliability levels. However, some evidence shows the failure related to defects in the 300-500 kV insulation system, as shown in Figure 1.7 [11]. About 72% of total failure cases are caused by a circuit breaker, disconnector, and busduct and interconnecting parts. The most important defects can be found around a protrusion from live or grounded parts, moving particles, void, and inside the spacer, and the mechanical loose of the floating component as shown in Figure 1.8. The defects may be caused by an error in manufacturing, shipping, assembly, and poor electrical contacts. The main failure causes in GIS are shown in Figure 1.9 [11]. It can be seen from Figure 1.9 that the defects shown in Figure 1.8 represent about 53% of the total main failure causes in GIS. Therefore, when any failure occurred in GIS, the insulation level would decrease. So far, GIS diagnosis should be the essential method for monitoring and investigating the stability and reliability of GIS [11, 12].

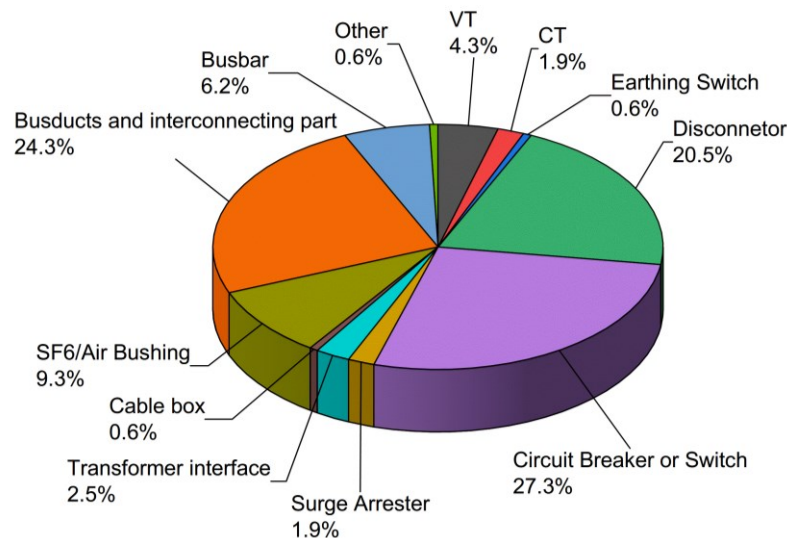


Figure 1.7. Main components involved in failures of 300-500 kV GIS. VT: voltage transformer and CT: current transformer. (Data from Technological progress in high-voltage gas-insulated substation [11])

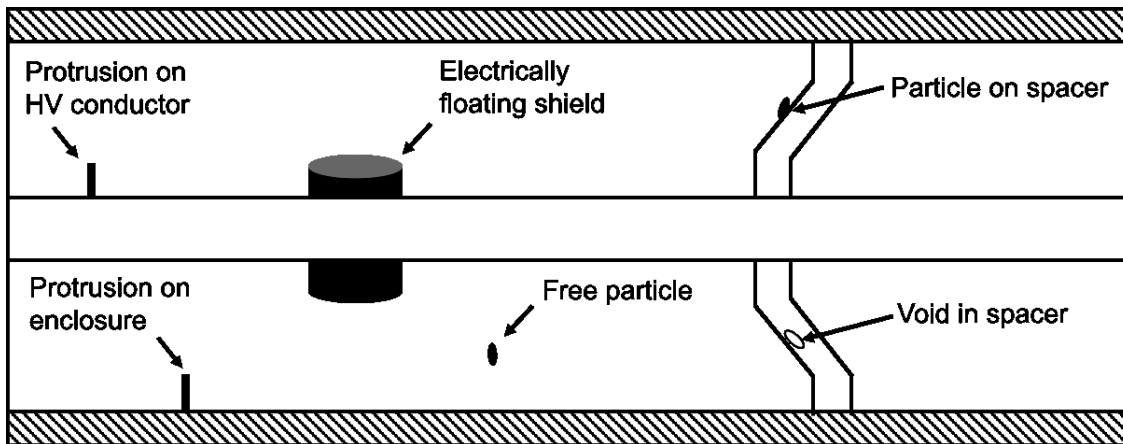


Figure 1.8. Possible defects in the insulation system of GIS.

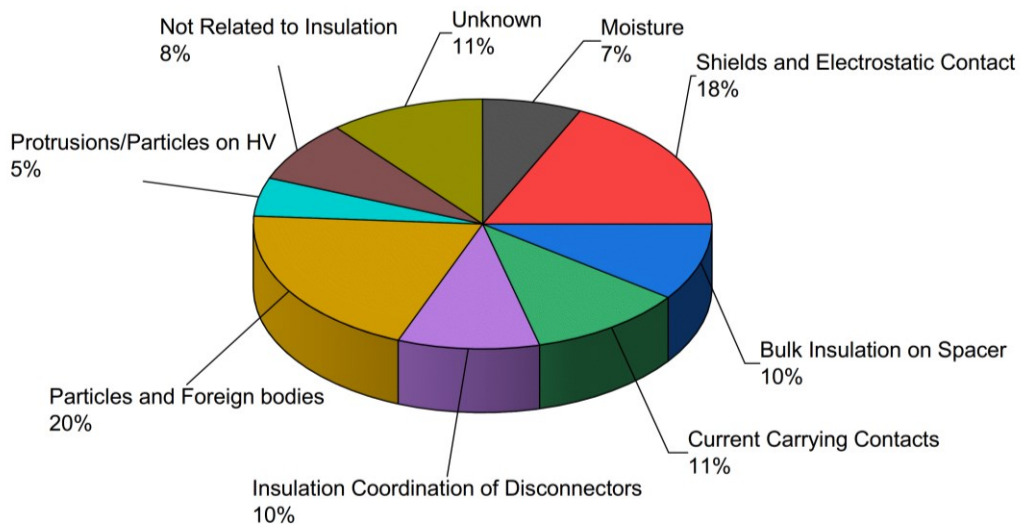


Figure 1.9. The main failure causes in GIS. (Data from Technological progress in high-voltage gas-insulated substation [11])

1.4 GIS diagnosis methods

The AC GIS range has recently reached up to 1,100 kV of the rated voltage, and 50 kA_{rms} of the rated short-circuit breaking current. Also, 1,200 kV AC GIS is going to be in the market very soon. Moreover, 500 kV DC GIS for the DC transmission system has become available. However, insulation faults may occur in the long lifetime of GIS, as described earlier. According to Figure 1.10 [18], a substation equipment can work maximum 45 years under the required reliability level (0.9–1), without maintenance it works only about 18 years (18.0149 years) and with optimal maintenance can work

maximum 45 years under the required reliability level. Therefore, the reliability of the power system has been essential in the new development trends. Mainly to keep GIS performance which can function, maintenance is necessary for its whole lifetime.

Usually, types of the maintenance of the power system equipment can be separated into three strategies: [19]

(1) Conventional breakdown maintenance (BDM): actions carried out after functional failure, *i.e.*, repair, overhaul, partial or total equipment replacement.

(2) Time-based maintenance (TBM): preventive actions carried out at predetermined intervals given by time or number of operations independent of the equipment.

(3) Condition-based maintenance (CBM): preventive actions are carried out depending on the equipment's condition. The condition is inspection on-line or at intervals that are fixed or dependent on the former inspection results.

The trend in GIS maintenance has shifted from BDM, in which devices are repaired, and parts are replaced only after a failure occurs. Apparently, BDM has demonstrated high risk of shutdown or blackout of system. To TBM, in which inspection, repair, and replacement are performed at regular intervals. However, TBM has the risk of over-maintenance, in the case of no failure in the system during some periods, which increases maintenance costs and even the failure rate. Instead, CBM, which detects GIS conditions, predicts their deterioration, and performs preventive maintenance, increasingly attracts attention. GIS monitoring and diagnosis by CBM can prevent the enormous failure as well as the unnecessary displacement of apparatus without damage.

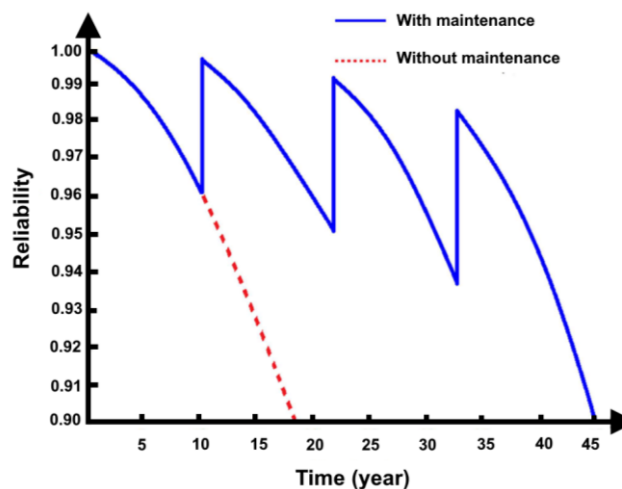


Figure 1.10. Reliability of substation equipment with and without maintenance [18]

1.5 Diagnosis techniques for partial discharge in GIS

IEC 60270 defined partial discharge (PD) as “localized electrical discharge that only partially bridges the insulation between conductors and which can or cannot occur adjacent to a conductor.” With the occurrence of partial discharge inside the GIS, high frequency switching pulses (voltage or current), sound, light, decomposed gases, electromagnetic waves, etc., are generated. Those phenomena and products can be an indicator for GIS diagnostics. The partial discharge detection techniques are classified based on parameters measured by sensors and other equipment. Each detection scheme has its detection range and physical quantity that limits its application. Diagnosis techniques can be divided into five techniques:

- (1) Electrical detection techniques: conventional electric method, pulse capacitive coupler method, and high-frequency current transducer method
- (2) Electromagnetic detection techniques: ultra-high frequency (UHF)
- (3) Acoustic detection techniques: acoustic sensor
- (4) Optical detection techniques: photomultiplier (PMT)
- (5) Chemical detection techniques: gas chromatography, Fourier transform infrared spectroscopy (FT-IR)

These techniques have demonstrated, for example, see references [20-26].

Each method has its advantages and disadvantages for practical application. UHF technique has a high sensitivity (a sensitivity in the MHz or more range), but the disadvantage is the attenuation of electromagnetic waves from PD, resulting in requiring many sensors, such as every 5 to 10 m for a typical GIS [12, 27]. The acoustic technique offers the advantages, such as a good sensitivity (a sensitivity in the kHz range) to detect most defect types, immunity to external noise, and defected can be localized, but the position of the sensor is limited because of the high attenuation of the acoustic wave signals which depend on structure of the GIS vessel [12, 27]. The electrical detection technique has a good sensitivity (a sensitivity in the pico-Coulomb range), but the on-site application is limited due to electromagnetic interference [12, 27]. Optical and chemical detection techniques are still under development. Here, I have proposed a new chemical detection-based GIS diagnosis method. I focused on the chemical detection in next section. The advantage and disadvantages of each technique are summarized in Table 1.6.

Table 1.6. PD detection techniques

Techniques	Typical methods	Advantage	Disadvantage	Reference
Electrical detection	IEC 60270 Conventional electric method, Pulse capacitive coupler method, High-frequency current transducer method	good sensitivity to defects	Inapplicable to GIS in service because of the need of an external capacitor On-site application is limited by electromagnetic interference	[28-30]
Electromagnetic detection	Ultra-high frequency (UHF) internal sensor and external sensor	High sensitivity	Sensitive to noise, attenuation of PD Complicated to install inside compact HV systems Require a large number of sensors for a whole GIS detection, 6-9 sensors per three-phase bay	[31-33]
Acoustic Detection	Acoustic sensor	High sensitivity to most defect type Immunity to external noise	High attenuation of the signal Not suitable to a permanently installed monitoring system, need many sensors to install	[34-36]
Optical Detection	Photomultiplier (PMT) Optical sensor	Discharges in gases which can be detected by optical sensors Detect emission of single-photon	Inaccessible GIS design for optical detection and due to expensive detection components	[37-39]
Chemical Detection	Gas chromatography Fourier transform spectroscopy infrared	free from noise, electromagnetic interference, and sensitivity up to 1 ppm Detect a permanent and cumulative byproduct of PD	limited to off-line preventive measures of GIS and require a long duration of time for the analyses	[40-42]

1.6 SF₆ decomposition detection methods

In this thesis, I have proposed a new chemical detection-based GIS diagnosis method. Basically, in an electrical arc, the decomposition products are formed in the presence of [43]:

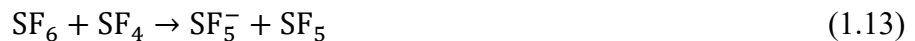
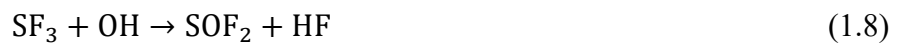
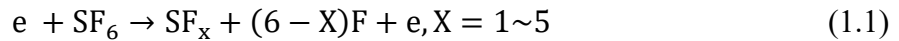
(1) an electrical arc formed by the opening of contacts normally comprising alloys based on tungsten, copper and nickel, containing residual quantities of oxygen and hydrogen

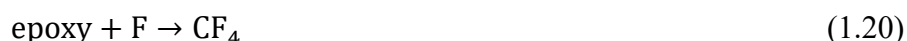
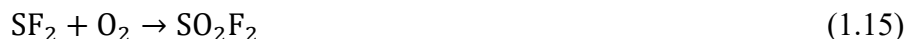
(2) impurities in the SF₆ such as air, CF₄ and water vapour

(3) insulating components comprising epoxy (C₂₁H₂₅ClO₅), plastic materials based on carbon, hydrogen and silica

(4) other metallic or non-metallic materials from which the equipment is constructed

As described above, which is the reason why the solid and gaseous decomposition products contain. This section describes the decomposition of SF₆. When SF₆ is exposed to PD or breakdown, it dissociates, then a part of the dissociated species recombines. Since the recombination occurs imperfect, many decomposition products such as HF, SO₂, CO₂, CF₄, SiF₄, SOF₂, SO₂F₂, S₂F₁₀, and SF₄ are generated. These decomposition products can be an indicator of PD, breakdown, or insulation failure in the system. The main reactions under PD are illustrated in the following equations [44].





In GIS practical application, decomposition gases are removed using active alumina or molecular sieves effectively. Suppose the adsorbent (molecular sieves or activated alumina) is present in the equipment in sufficient quantity in the gas compartment. In that case, the level of corrosion due to the SF₆ decomposition product (SO₂, HF in particular) is very slight, if not negligible. This is because the adsorbents have a very rapid and effective action such that the corrosive gases do not sufficient time to react with other materials.

In the real-world GIS, normally, for SF₆ byproducts analysis, an absorbent used for decomposition gas absorption is not installed in the compartment, the most common diagnostic gases are SOF₂ and SO₂F₂ measured by the gas chromatography and mass spectrometer they may be detected with sensitivities down to 1 ppmv (part per million by volume). Byproducts of SF₆ decomposition can be detected by different techniques, for example, gas detection tubes, gas chromatography, FT-IR, and gas sensors. Information such as insulation degradation type, property, and level can be measured by quantifying the gas decomposition components. These chemical detection tools are free from noise and electromagnetic interference. The sensitivity of the gas detection is typically below 1 ppm. GC and FT-IR have high sensitivity but are costly, time-consuming, and suitable for laboratory-based analysis rather than continuous on-line monitoring or portable detection. A detection tube can be used to detect major decomposition products, such as SO₂ and HF, at ppm levels. However, detection tubes have poor accuracy because the concentration of decomposition products is determined by color change, making these tubes unsuitable for on-line monitoring. A gas sensor can be installed in the GIS vessel to achieve on-line monitoring or portable detection. However, the sensitivity and interference are still under development. The advantage and disadvantages of each chemical technique are summarized in Table 1.7.

Table 1.7. Commonly used chemical detection method

Method	Accuracy	Speed	Anti-interference	Range	Portability	References
Gas chromatography	ppb	The complex operation, slow detection speed	Strong anti-interference ability	Most decomposition product	Just suitable for laboratory testing	[24]
Infrared transform spectroscopy	ppm	By IR band database, very fast operation	Strong anti-interference ability	Most decomposition product	Just suitable for laboratory testing	[20]
Detection tube	ppm	By color comparison, fast detection speed	Easily affected by cross-interference	Partial products, such as SO ₂ , HF, and other strong acid	Simple structure, easy to carry	[25]
Gas-sensitivity sensor	ppm	Calculate through the change of the sensor resistance fast detection speed	Poor gas selectivity, easy to be contaminated	SO ₂ , SOF ₂ , SO ₂ F ₂ , and H ₂ S	Good portability	[23]

1.7 Chemical detection-based GIS diagnosis

Recently, byproducts of SF₆ have been studied in many works, such as the analysis or detection of SF₆ decomposition, which will help verify the failure in GIS [45]. Furthermore, the analysis of generated decomposition gas can indicate the types of PD [46, 47]. In our lab, it was demonstrated that the SF₆ decomposition products, such as HF, SO₂, SOF₂, generated by DC corona discharge could be detected by using a carbon nanotube (CNT) gas sensor fabricated by positive dielectrophoresis (DEP), which is applicable to fabricate the gas sensors.

I proposed the new schemes for rapid, inexpensive, and on-site diagnosis of gas-insulated switchgear (GIS) in this work. It focuses on residual CF₄ in the GIS, one of the decomposition gases from SF₆ by partial discharge or breakdown. Among the variety of decomposition gases, only CF₄ accumulates for a long time because an absorber removes the others [48]. Therefore, the amount of CF₄ represents the condition of GIS (details are described in Chapter 2).

Chapter 2

Research objective and overview concepts

2.1 Objective

Studies described in the thesis aimed to develop methods for the detection of residual CF_4 in GIS. The methods are to realize rapid, inexpensive, and portable devices for GIS diagnosis. This section will explain the overview concepts for the CF_4 detection method and discuss the comparison between the current method and the proposed method for gas analysis for GIS diagnosis.

Typically, recommended maintenance plan of GIS consists of virtual inspection (ideally several times a year), minor inspection (every 5-10 years), and major inspection (every 15-20 years) [48]. As mentioned in Chapter 1, recently, CBM would be applied to the inspection method. Moreover, using the system integrity protection scheme (SIPS) [49] for power system and GIS condition monitoring is integrated with the machine learning and internet of things (IoT) and automated monitoring to increase the diagnosis performance [50-52]. To illustrate, the worst case occurred in GIS, about fault that occurred exceed the expectation. Therefore, inspection, protection, and recovery of the system should consider earlier under the right decision that it should be keep working or stop working then diagnosis. For these reasons, the GIS diagnosis method, which is easy, rapid, reasonable, and can be used whenever needed, has been required for GIS diagnosis.

The minor inspection of GIS is performed every 5-10 years. This inspection checks the impurity in SF_6 (if the GIS vessel is not equipped with absorbers). This maintenance does not require opening the vessel, but the inside gas is sampled for laboratory analysis. Generally, the sampled gas is analyzed by gas chromatography (GC) and Fourier transform infrared spectroscopy (FT-IR). Then, the decomposition gas was analyzed. These methods take time for analysis due to operation in the laboratory. For this condition, the rapid and on-site test method is interesting and high impact on the GIS diagnosis engineering field. We have researched the methods to be the one choice for GIS diagnosis. The proposed CF_4 detection would be required during the due date of minor inspection.

In this thesis, CF_4 in SF_6 was considered a detection target because it is retained for a long time in the GIS vessel after the generation. Details of the CF_4 and its generation

process are described below. The CF₄ detection methods were designed for an off-line diagnosis. Unfortunately, the gas sampling method needs some quantities of decomposition gas for gas analysis. In addition, the CF₄ analysis system might need some space for installation inside the GIS system, including concern of interference of any signal or noise from GIS. Therefore, I decided to take the gas sample from GIS and on-site analysis. However, we have not given up yet on an online diagnosis. In future work, we would improve the method as well as the performance of the system.

The gas analysis should be divided into two categories, SF₆ purity analysis and SF₆ decomposition analysis. The former is an analysis of SF₆. SF₆ can be sampled and analyzed. SF₆ gas samples can be collected in specially-prepared stainless-steel sampling bottles and sent to a laboratory for analysis. Moreover, in some cases, portable instruments are used. The tools are used to measure moisture – typically, 'dew point' hygrometers are used for this proposal. The latter is SF₆ decomposition analysis. Typical analysis may include N₂, O₂, CF₄, SO₂, SO₂F₂, and SOF₂ operated in the laboratory.

The fact [48] that the portable instruments have the advantage of immediacy measurement results is immediately available, but less detail is available. On the other hand, laboratory testing offers a more comprehensive analysis but with the inevitable delays and possibility of sample contamination and degradation en route to the lab. Nevertheless, in this study stage, we would research and study the potential of our concept on CF₄ detection and sizing of the detection system and discussion in some topic-issued cases.

2.2 Decomposition product effect and why CF₄ is the detection target

CF₄ is one of the decomposition products of SF₆ [48]. CF₄ has attracted attention as an indicator for the GIS diagnosis because CF₄ accumulates in the GIS vessel for a long time [45, 48]. This is because CF₄ is hard to be removed by an absorbent generally placed in the GIS [53]. According to IEC 60480, the maximum acceptable CF₄ level for re-used SF₆ is 3% in volume. Therefore, the CF₄ detection can be considered as the failure indicator of the GIS. CF₄ is generated when the reactions with the discharge involve carbon-including materials such as insulator solids and grease. The molecular structure and some properties of CF₄ are shown in Figure 2.1 [54] and Table 2.1 [55], respectively.

Chu [56] reports the decomposition products in the enclosed compartment affect the system performance in two ways. The presence of gaseous and solid by-products may

lower the dielectric strength of the system.

The former, Manion [57] tests the arc stability of electronegative gases. The results indicated that even for arc by-products up to 30% by volume, there is no degradation of dielectric strength of the gas gap. The relative dielectric strength of by-product at uniform field for SF₆, SOF₂, SO₂F₂, SO₂ and CF₄ are respectively 1.0, 1.4, 0.75, 1.0, 0.42. Because of the dielectric strengths of these arc by-products and their concentration, it is not surprising that there is little effect on the gas gap's insulation system. Although, these decomposition gases can chemically attach solid insulating material, which may eventually lead to a reduction of the dielectric strength.

The latter, Murakami and Menu [58] claimed a 20% reduction of flashover strength when the insulating surface was covered with by-products generated from arcing. Chu [59] reports that the fluoride powder formed during arcing has a very large surface area, and the powder can adsorb significant quantities of gaseous by-products. The surface adsorbed gaseous by-product reaction and the solid insulating surface when the solid by-product contact the surface are responsible for reducing the solid insulator's dielectric strength.

Fault, such as discharges and arcs between the contact of switching devices during operation, and accidents caused by a defect of the equipment, generates many by-product species. The most-reported SF₆ by-products are SF₄, SOF₂, SO₂F₂, SO₂, S₂F₁₀, and AlF₃ [45]. CF₄ is also generated. It is often found when the arcs occur on the polymeric insulators and grease used in the GIS [48]. In the practical application, it has been revealed that most of the decomposition gas is removed and controlled using an absorbent [45, 53]. However, the absorbent or filtration cannot effectively remove CF₄. Figure 2.2 [53] shows the decomposition gas removal efficiency with and without the absorbent. It is clearly understood that CF₄ cannot be removed completely. Typically, GIS manufacturers put the absorbent to the gas compartment. Other decomposition gases are removed. But CF₄ is still remains in the gas compartment. For these reasons, the unique diagnosis of CF₄ is we can apply CF₄ detection to any gas compartment in GIS, with and without the absorbent. Next, I explained why CF₄ cannot be removed by an absorbent, following some references below.

Table 2.2 [60, 61] shows the size of gas molecule including SF₆, CF₄, CO, and CO₂. Comparing SF₆ and CF₄, they are nearly the same of molecule size, 5.5 and 4.7 Å, respectively.

Figure 2.3 [62] shows the relationship between pore diameter of various zeolites and molecular diameter of molecules. There are many pore sizes for suitable gas specie removal. The company where provide an absorbent such as Sinopharm Co. Ltd. and Shandong Taikai High Voltage Switchgear Co, Ltd. [63]

However, Cai *et.at* [64] report a very little adsorption occurs in the pores smaller than 8 Å for SF₆ and CF₄. Moreover, Chu [45] explains the time constant for the absorbent to remove all decomposition gases will be in several days and indicates that the absorbent cannot effectively remove CF₄, for the same reason that it cannot remove SF₆ because both are nonpolar molecule. Therefore, CF₄ is retained for a long time after the generation by faults. The amount of CF₄ in GIS indicates that the number of the failure and the resulting insulation failure.

Chu [45] reports that when discharge in SF₆ occurs near a polymeric material, the CF₄ concentration increases as a function of discharge energy and duration. CF₄ concentration in a gas component has experienced partial discharge due to loose contact near an epoxy coating. In this case, CF₄ is generated greater than 1000 ppmv. According to Kyushu electric company's maintenance inspection data, the CF₄ amount (M_{CF₄}) in their 66 kV GIS in 2017 was investigated. M_{CF₄} was measured in overhaul inspection of the disconnectors that occurred from a loose connection, as shown in Table 2.3 [65]. Shinkai [66] reported that CF₄ was found in overhaul inspection of the disconnectors that occurred from a loose connection. The critical amount of the CF₄ analysis curve demonstrated in the relationship between number of operation and amount of CF₄ (mg) is shown in Figure 2.4 [66]. Based on a statistical analysis, a critical amount of M_{CF₄} is determined about 200 mg (abnormal condition) [66]. To assume that the quantity of the gas sample is 10 kg for a one-time GIS diagnosis. Then, we can estimate the parts per million (ppm) by volume (or ppm mass) of CF₄/ SF₆ is around 33.17 ppm by volume [67]. This value can be regarded as the sensitivity of CF₄ detection for GIS diagnosis.

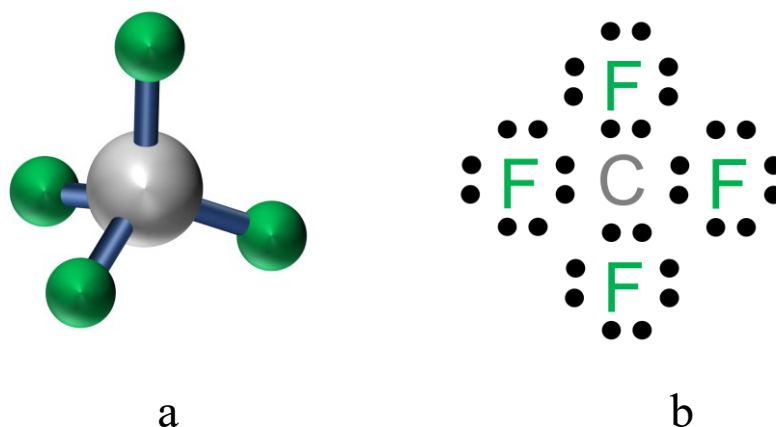


Figure 2.1. CF_4 molecule. (a) Molecular structure, and (b) Lewis structure of C-F bonding [54]. Green and gray spheres in (a) indicate fluorine and carbon atoms, respectively.

Table 2.1. Some properties of CF_4 . (Data from American Element [55], [57])

Properties	
Compound Formula	CF_4
Molecular Weight	88
Appearance	Colorless liquified gas
Melting Point	$-184\text{ }^\circ\text{C}$
Boiling Point	$-130\text{ }^\circ\text{C}$
Density	3.01 (vs. air)
Exact Mass	87.993613
Monoisotopic Mass	87.993613
Relative dielectric strength [57]	0.42

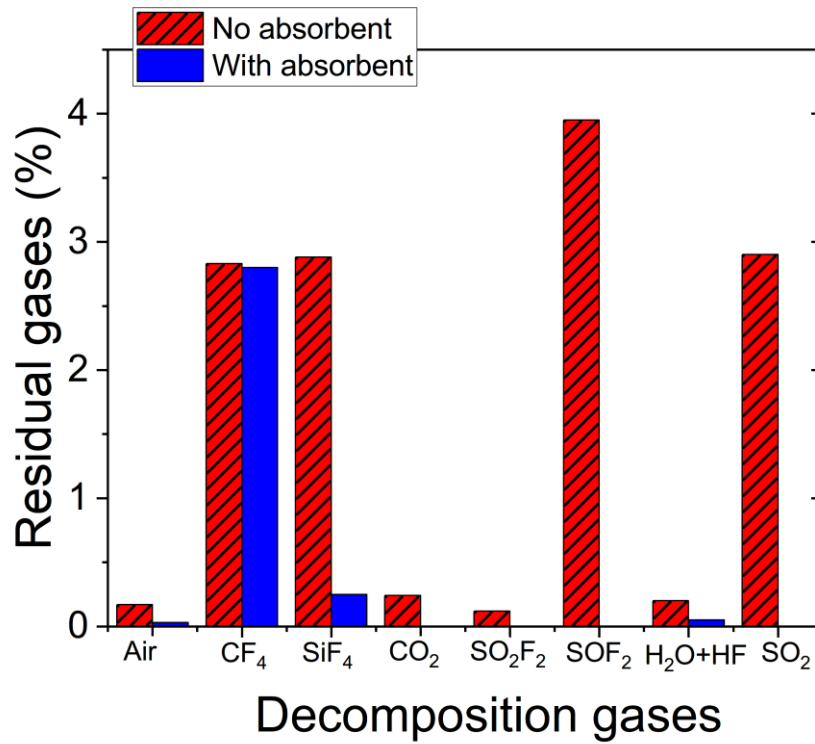


Figure 2.2. Results of analysis of SF₆ decomposition with and without an absorbent. (data from Cahier technique no.188, SF₆ properties, and use in MV and HV switchgear [53])

Table 2.2 Size of gas molecules [60, 61]

Gas	Diameter of gas molecule (Å)	Diameter of gas molecule (nm)
SF ₆	5.5	0.55
CF ₄	4.7	0.47
CO	3.7	0.37
CO ₂	3.3	0.33

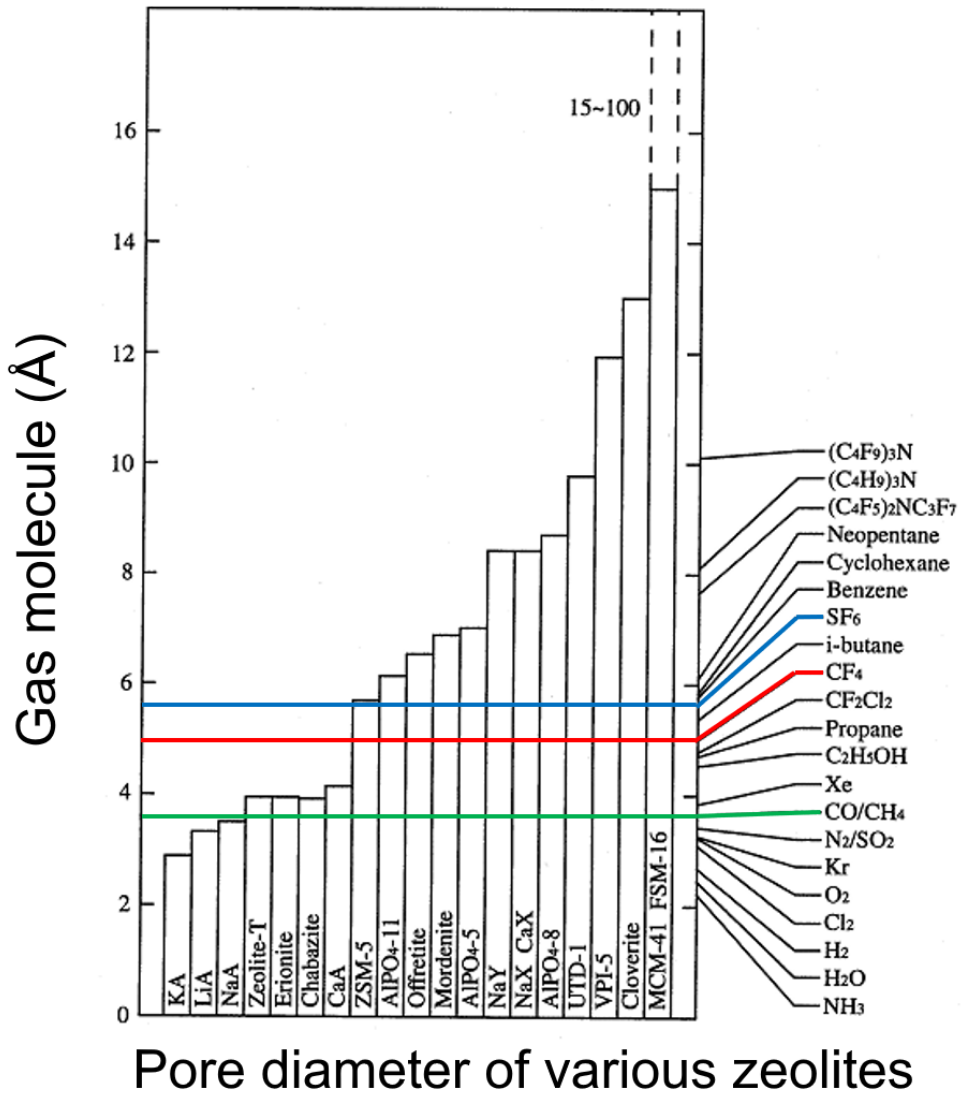


Figure 2.3. Relationship between pore diameter of various zeolites and molecular diameter of molecules (Data from <https://jza-online.org/magazines> [62])

Table 2.3. Amount of C_{CF_4} [ppm] and number of operation of 66 kV GIS [65]

電力中央研究所 2017 年度委託成果報告書「66kV GIS のガス分析に基づく状態診断と解体調査立会いにおける内部調査」

Number of operation	M_{CF_4} [mg]	M_G [kg]	C_{CF_4} [ppm]
388	0.082	7	0.02
554	0.212	12	0.03
-	$\cong 0$	32	<0.01
204	0.618	7	0.15
228	1.554	11	0.24
207	0.824	28	0.05

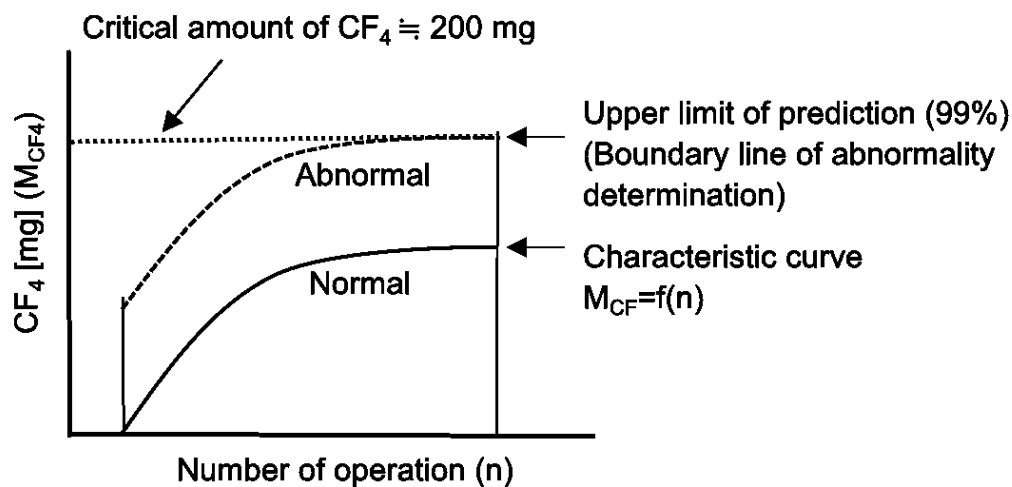


Figure 2.4. The characteristic curve of the loose connection diagnosis method [66]. This curve estimates the critical value of CF_4 for abnormal condition at 200 mg

2.2 Related studies

In this research, two types of CF_4 detection methods are considered. The first one utilizes nanomaterial-based gas sensors fabricated by dielectrophoresis (DEP). The another uses non-thermal plasma application. In this section, a brief review of the related studies is described.

2.2.1 Nanomaterial-based gas sensor

Recently, there are various kinds of metal oxide for gas sensor application, the structure including such as nanowire, nanotube, nanosphere, nanorods, and nanobelts as well as methods for sensor fabrication. The research in nanomaterial-based gas sensors is mostly achieving at high sensitivity and improved limit of detection. The nanomaterial-based gas sensors are widely used in industry and firefighting to detect explosive, flammable, air pollution, and toxic gases threatening human health and properties. The nanomaterial-based gas sensors have been made to increase the sensitivity, selectivity, response and recovery speed, and stability of the metal-oxide-based sensor [68]. I explained the sensor fabrication and CF₄ detection scheme in Chapter 3.

In the previous studies of our laboratory, it has been reported that PD detection by using a carbon nanotube (CNT) gas sensor. In the researches, SF₆ decomposition products, including HF, SO₂, and SOF₂, were detected by the CNT gas sensor. The sensor was fabricated by dielectrophoresis [69-71]. Our group has studied and applied the DEP technique for many applications such as gas sensor fabrication and DNA detection. The details of the applications can see elsewhere [72-75]. DEP and its application in gas sensor fabrication are described in Chapter 3. Features of the nanomaterial-based gas sensor are also described in Chapter 3. Several kinds of nanomaterials were demonstrated to detect CF₄ directly.

2.2.2 Non-thermal plasma applications

Inspired by many kinds of discharge plasma applications [76], I proposed indirect CF₄ detection.

From the late 1990s, it has been required to strictly control perfluorinated compounds (PFC) emission to the atmosphere for preventing global warming. Since then, various methods to remove PFC from the exhaust gas, including chemical adsorption, catalyst, plasma decomposition, and combustion, have been studied [77-78]. Discharge-plasma-based CF₄ decomposition techniques have been reported. Many of them used a discharge plasma generated in CF₄ mixed with O₂ to convert CF₄ to COF₂, CO, and CO₂, which have lower global warming potentials than CF₄ [79]. Yu and Chang [80] used a cylindrical reactor to generate dielectric barrier discharge (DBD) energized by a high-voltage AC (60 Hz). CF₄ conversion efficiency increased with O₂ concentration and reached 27.6% with 20% O₂ addition. Kim *et al.* [81] reported that using the DBD

streamer and glow mode enhanced the CF₄ removal efficiency. The optimal concentration of added O₂ to treat 500-ppm CF₄ was between 500 and 10,000 ppm. Kuroki *et al.* [82] used an inductively coupled plasma to decompose a CF₄/O₂ mixture. It was reported that CF₄ could be almost completely decomposed at 2 MHz with an O₂/CF₄ ratio of 1.0~1.25. Pan *et al.* [83] demonstrated that perfect CF₄ removal by combining non-thermal plasma with γ -Al₂O₃.

This motivated us to develop an indirect CF₄ detection method by converting it into easily detectable gas species, CO and CO₂. This concept was inspired by previous studies on CF₄ emission control in the semiconductor and optoelectronic industries. In the industries, PFC such as CF₄, C₂F₆, and C₃F₈, which contribute significantly to global warming, was used for cleaning chemical vapor deposition (CVD) chambers and for plasma etching processes.

Motivated by these previous studies, we proposed an indirect CF₄ detection method in which CF₄ is converted into CO and CO₂ by discharge plasma. Because there are many sensitive and inexpensive CO and CO₂ gas sensors commercially available, the proposed method has the potential of achieving reliable and cost-effective GIS diagnosis.

Following two sections, concepts of the direct and indirect detections of CF₄ are described.

2.3 Direct CF₄ detection

Figure 2.5 shows the concept of direct CF₄ detection by using several kinds of nanomaterial-based gas sensors. First, the gas is sampled from the GIS, and then residual CF₄ in the gas is investigated by the nanomaterial-based gas sensors.

To select the nanomaterials for CF₄ detection sensor based on the term of inexpensive material and commonly used in gas sensor application. The sensitivity (detection limit, ppm) and response characteristics (response and recovery time) of each sensor material would be investigated.

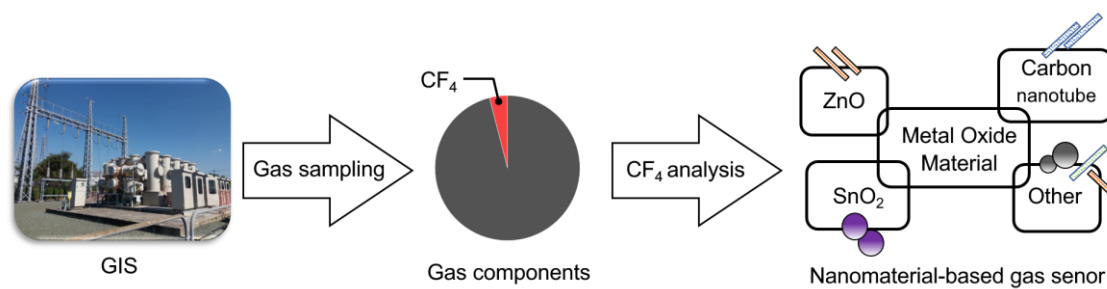


Figure 2.5. Direct CF₄ detection concept. (Sampled gas taken from GIS, including CF₄ and other decomposition gas, is analyzed by several kinds of nanomaterial gas sensors)

2.4 Indirect CF₄ detection

Figure 2.6 shows the concept of indirect CF₄ detection by CF₄ conversion by DBD application. The sampled gas is mixed with O₂ additive, then DBD-treated to generate CO and CO₂. The generated CO and CO₂ can be detected with gas sensors. In GIS, CF₄ is major decomposition gas containing carbon atom [45]. Even if CO and CO₂ have already existed in the sample gas, the proposed method should work by evaluating the increment of these gas concentrations after DBD treatment. This implies that CO and CO₂ detection in plasma-treated sample gas can be regarded as an alert for possible accumulation of residual CF₄ in the GIS.

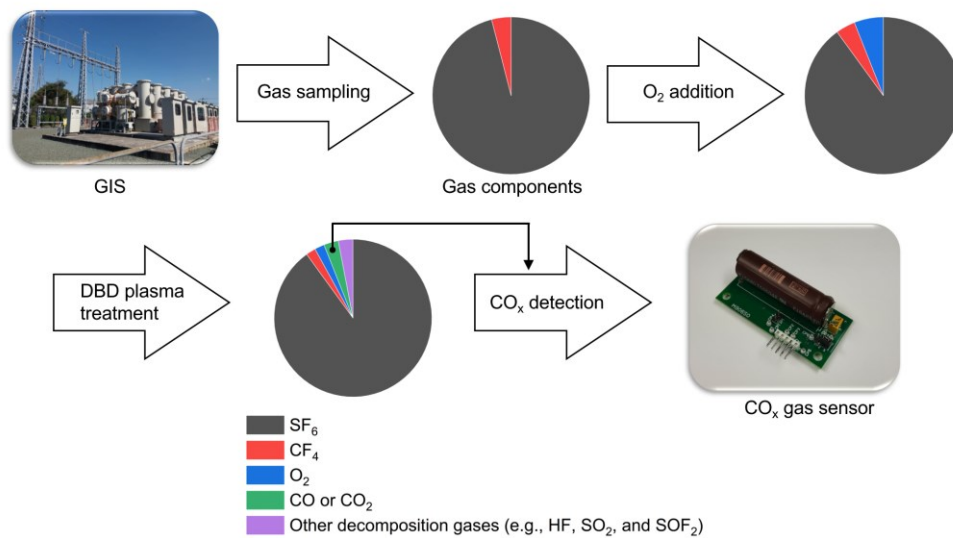


Figure 2.6. Indirect direct CF₄ detection concept. (Sampled gas taken from GIS, including CF₄ and other decomposition gas, is analyzed by CF₄ conversion into CO and CO₂ using DBD application)

2.5 The details of each chapter in the dissertation

This dissertation is based on direct and indirect CF₄ detection, as mentioned above, and consists of six chapters.

Chapter 1: introduction to world electricity consumption. How necessary of liability of the power system leading to power system improvement. GIS is one crucial key of the power system. Explanations of increasing the number of GIS substations, fault types and possible defects that occurred in the system, and diagnosis methods are the essential background knowledge to understand the real-world situation of GIS and to find the way to improve GIS in the future.

Chapter 2: research objective and concepts. This chapter describes the background of this research, including both direct and indirect CF₄ detection concepts. I explained my research based on three concepts, including rapid test, inexpensive, on-site test. Explanation of why CF₄ is interesting to be detection target gas and how to set CF₄ sensitivity target.

Chapter 3: direct CF₄ detection by using several kinds of nanomaterial-based gas sensors fabricated by the DEP process. Experimental results of CF₄ detection using several gas sensors are reported. Discussion about the sensitivity for practical application

is shown.

Chapter 4: indirect CF₄ detection by CF₄ conversion into CO and CO₂ by DBD application. The new proposed scheme is examined. The possibility and limitation of the detection system are discussed.

Chapter 5: after I tried to fabricate the CF₄ gas sensor with a single nanomaterial, SnO₂, ZnO, and SWCNT, the results showed a very low response against 1000-ppm CF₄. To demonstrate the new technique of hybrid nanomaterials. This chapter shows the new DEP-based nanomaterial sensor fabrication technique applying to NO₂ gas. The hybrid nanomaterial-based gas sensor fabricated by two steps of DEP was investigated to expose NO₂. This study is not related to CF₄ detection directly, but this point would be the starting point to study the hybrid materials gas sensors.

Chapter 6: summary of the dissertation and future works.

Chapter 3

Direct CF₄ detection by using nanomaterial-based gas sensors

3.1 Introduction

As described in Chapter 2, at first, I tried to detect the residual CF₄ by using several kinds of metal oxide nanomaterials. Nowadays, there are many kinds of metal oxide used to fabricated gas sensors [68, 84-86], such as tin oxide (SnO₂), zinc oxide (ZnO), titanium oxide (TiO₂). Several metal oxides are suitable for gas detection, which provide the sensor for the reducing or oxidizing gas. Summary of some studies of nanoparticles for the gas sensing is listed in [87]. The variety of the metal oxides [88] and the elementary forms of 1D metal oxide nanostructures [68] used for gas sensor applications are shown in Figure. 3.1a and 3.1b, respectively. To the best of my knowledge, there is no study to detect CF₄ using metal oxide nanomaterials. In these data, it seems that SnO₂ and ZnO should be the best candidate to select for the first trial of CF₄ detection because they are the most utilized material, inexpensive, variety of crystal structure, and familiar material on the earth. They are n-type granular material whose electrical conductivity is dependent on the density of pre-adsorbed oxygen ions on its surface. Metal oxide semiconductors (MOS) have to deal with the low response at room temperature [68]. Usually, MOS has to be heated by an additional heater for operation while carbon nanotube (CNT) gives high and fast responses at room temperature [89]. Therefore, SnO₂, ZnO, and CNT were investigated for the ability of CF₄ detection [90].

3.2 Nanomaterial-based gas sensors

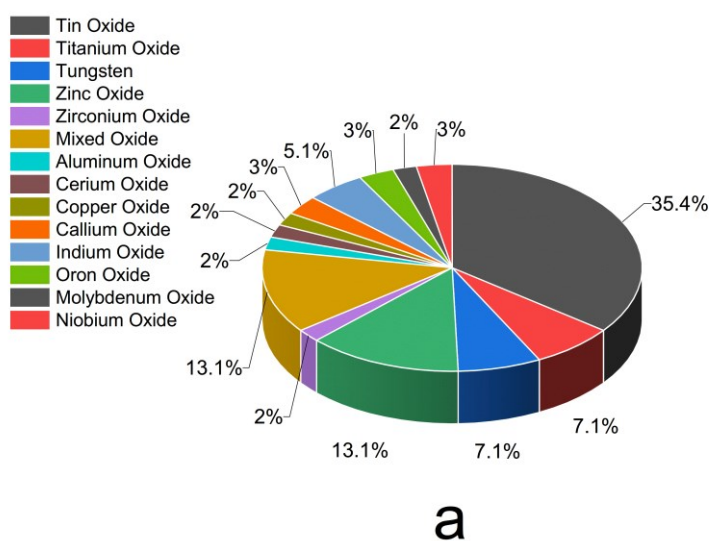
3.2.1 Tin oxide (SnO₂) and zinc oxide (ZnO)

Generally, a SnO₂ gas sensor was used to detect several gas species such as CO, CO₂, and NO₂ [68]. As mentioned above, SnO₂ was selected to detect the CF₄ because the SnO₂ gas sensor demonstrated the highest response against fluorocarbon gas, CCl₂FCClF₂ (R-113) and CHClF₂ (R-22) among several kinds of metal oxide, such as SnO₂, ZnO, In₂O₃, Fe₂O₃, and WO₃ [91]. T. Nomura *et al.* [91] report the improvement of the sensitivity to fluorocarbon, surface-modification effects on fluorocarbon detection of a gas sensor based on metal oxides such as SnO₂, ZnO, In₂O₃, Fe₂O₃, and WO₃, have

been examined. It is reverent that SnO₂ is the most suitable material for fluorocarbon detection. Thirty-nine kinds of elements have been investigated as additives to SnO₂, which significantly affect its sensing characteristics. It is confirmed that sulfur is the most effective modifier to improve sensitivity.

CF₄ is one of the perfluorocarbon gases. There are some evidences to explain the interaction between SnO₂ and C-F bond. For these reasons, I chose a SnO₂ nanoparticle to fabricate the gas sensor for the direct CF₄ detection.

Gas sensors using zinc oxide (ZnO) nanomaterials have been studied in the number of works for detecting variety of gas species such as CH₄, CO, and H₂S. Again, according to T. Nomura *et al.* [91], a ZnO gas sensor was selected to observe the response of fluorocarbon gases in the same study. The result shows that SnO₂ shows the highest response as described above, and ZnO shows the second-high response, which lower than SnO₂. As a typical n-type semiconductor, ZnO exhibits unique characterizations required for an ideal gas sensor, such as a wideband gap of 3.37 eV, large exciton binding energy of 60 meV, high electromobility, photoelectric response, excellent chemical and thermal stability. Much more attention is particularly paid to the practical strategies that create room-temperature gas sensing of ZnO-based gas sensors, mainly including surface modification, additive doping, and light activation. Finally, some perspectives for future investigation on room-temperature gas-sensing materials are developed as well [92].



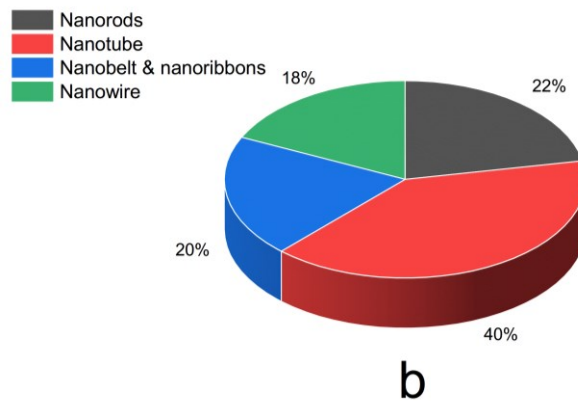


Figure 3.1. Nanomaterials (a) Relative comparison of various metal oxide as gas sensor [88] (b) Element forms of 1D metal oxide nanostructures [68]. Data from Review Recent Advances in Tin Oxide Nanomaterials as Electrochemical/Chemiresistive Sensors, Handbook of Gas Sensor Materials Properties, Advantages and Shortcomings for Applications. These graphs show the candidate metal oxides for gas sensors fabrication.

3.2.2 Working principle of semiconducting nanomaterial gas sensor

The working principle of the gas detection using metal oxide material is explained in the simple case for n-type semiconducting metal oxide [93]. Figure 3.2 shows the sensing mechanism of SnO₂ nanomaterial-based gas sensor in the atmosphere. In the figure, structure and band models before and after exposing carbon-monoxide (CO) are shown. Energy bands are presented; E_V , E_F , and E_C denote the valence band, Fermi level, and conduction band, respectively. When molecules interact with the surface of SnO₂, the band structure changes.

In the air, free electrons activated from the conduction band E_C of SnO₂ extract the oxygen molecules. They are then forming molecules (O_2^-) or atomics (O^-) on the SnO₂ surface. The reaction leads to band bending, upward band, and the depleted region of SnO₂ bulks. CO gas is exposed to SnO₂. CO gas molecules react with oxygen molecules or atomics on the SnO₂ surface to form CO₂ with leaving an extra electron. At the same time, band bending is reversed by releasing electrons to the bulk. The thickness of the depletion region decreases, which is a receptor function. The Schottky barrier between two grains is lowered, and it is easy for electrons to conduct in the sensing layers

through different grains, which is a transducer function. Therefore, the conductance among the grains is changed under the exposing gas condition [94-96].

Before CF_4 is exposed to a sensor, background gas is initialized until the sensor's conductance is attained as stable, approximately 1-2 h. Initialization time or warm-up time is an essential parameter, which determines the application potentiality of the sensors. The sensors are used in the conductance mode and at temperatures higher than room temperature. Thus, when it is heated from room temperature to working temperature, it requires some time to attain operating temperature and initial equilibrium conductance.

Then begin to expose CF_4 to the sensor. However, it was noted that, in the case of CF_4 detection, the SnO_2 , ZnO , and CNT gas sensors would be initialized to attain the baseline in SF_6 gas. It was not in the air because SF_6 is the major component when the sampling gas is taken from the GIS field for decomposition gas analysis. The reaction mechanism between the metal oxide and gas phases should be different from the reaction mechanism described above. Therefore, I would observe and verify the responses of metal oxide as well as the response characteristics of each sensor.

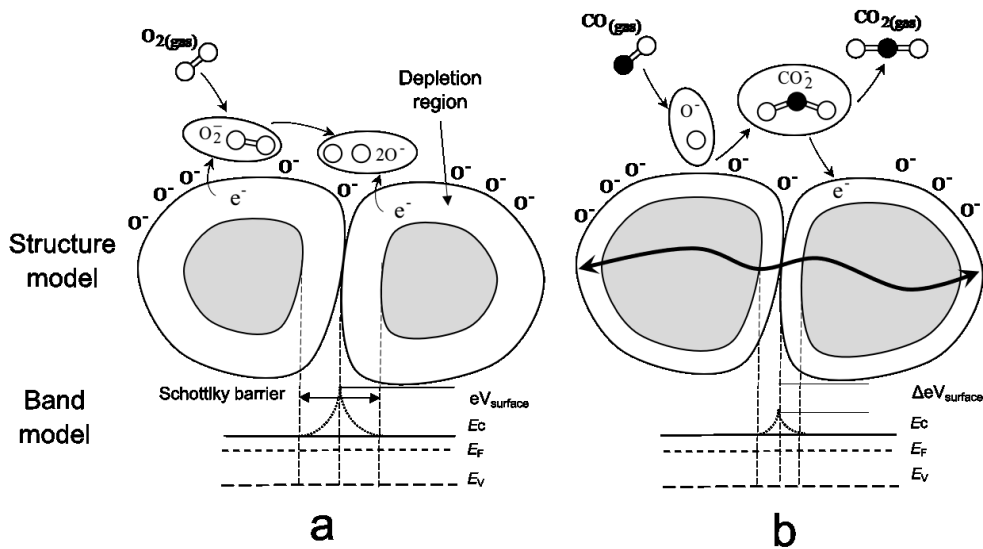


Figure 3.2. Structure and band models of sensing mechanism for n-type semiconducting metal oxide (a) before (b) after exposing CO [93].

3.2.3 Carbon nanotube (CNT)

In the recent year, carbon nanotube gas sensors have received considerable attention because of its excellent properties such as rapid response, high sensitivity, and lower operation temperature when compared with MOS [97-100]. Part of the reason for the explosion of interest from the gas sensor community in carbon nanomaterials is that while ranging from well-defined nanosized molecules to tubes with lengths of hundreds of microns, they do not exhibit the instabilities of other nanomaterials as a result of the very high activation barriers to their structural rearrangement. As a consequence, they are highly stable even in their unfunctionalized forms. Despite the wide range of carbon nanomaterials possible, they exhibit common reaction chemistry: that of organic chemistry [89].

3.3 Dielectrophoresis

Dielectrophoresis (DEP) is the electrical force acting on a dielectric particle suspended in a medium under the nonuniform electric field. This is based on the polarizations of the particle and the medium.

DEP force acting on the spherical particle of radius R suspended in a medium of absolute permittivity ε_1 is given by [101]

$$\mathbf{F}_{DEP} = 2\pi\varepsilon_1 R^3 \text{Re}[K(\omega)] \nabla |\mathbf{E}|^2 \quad (3.1)$$

Where $|\mathbf{E}|$ is the magnitude (rms) of the applied voltage and $\text{Re}[K(\omega)]$ is the real component of the Clausius-Mossotti factor given by

$$\mathbf{K}(\omega) = \frac{\varepsilon_2^* - \varepsilon_1^*}{\varepsilon_2^* + 2\varepsilon_1^*} \quad (3.2)$$

where ε_1^* and ε_2^* is the complex permittivity of the medium and particle, respectively.

The complex permittivity is defined as $\varepsilon^* = \varepsilon - j\left(\frac{\sigma}{\omega}\right)$, where ε is the permittivity, σ is the conductivity of dielectric, and ω is the angular frequency of the applied dielectric field.

The complex Clausius-Mossotti function is obtained by substituting into Equation (3.2):

$$\mathbf{K}(\omega) = \frac{\left(\varepsilon_2 - \frac{j\sigma_2}{\omega}\right) - \left(\varepsilon_1 - \frac{j\sigma_1}{\omega}\right)}{\left(\varepsilon_2 - \frac{j\sigma_2}{\omega}\right) + 2\left(\varepsilon_1 - \frac{j\sigma_1}{\omega}\right)} = \frac{\omega(\varepsilon_2 - \varepsilon_1) - j(\sigma_2 - \sigma_1)}{\omega(\varepsilon_2 - 2\varepsilon_1) - j(\sigma_2 - 2\sigma_1)}$$

Multiplying the numerator and denominator by the complex conjugate of the denominator

$$\mathbf{K}(\omega) = \frac{\omega^2(\varepsilon_2 - \varepsilon_1)(\varepsilon_2 + 2\varepsilon_1) + (\sigma_2 + 2\sigma_1)(\sigma_2 - \sigma_1)}{\omega^2(\varepsilon_2 + 2\varepsilon_1)^2 + 2(\sigma_2 + 2\sigma_1)^2} + j \frac{\omega(\varepsilon_2 - \varepsilon_1)(\sigma_2 - 2\sigma_1) - (\varepsilon_2 - 2\varepsilon_1)(\sigma_2 - \sigma_1)}{\omega^2(\varepsilon_2 + 2\varepsilon_1)^2 + 2(\sigma_2 + 2\sigma_1)^2}$$

On substituting into this expression, the characteristic relaxation (response) time τ given by

$$\tau = \frac{\varepsilon_2 + 2\varepsilon_1}{\sigma_2 + 2\sigma_1} \quad (3.3)$$

The real component is

$$\text{Re}[K(\omega)] = \left[\left(\frac{\omega^2 \tau^2}{1 + \omega^2 \tau^2} \right) \left(\frac{\varepsilon_2 - \varepsilon_1}{\varepsilon_2 + 2\varepsilon_1} \right) + \left(\frac{1}{1 + \omega^2 \tau^2} \right) \left(\frac{\sigma_2 - \sigma_1}{\sigma_2 + 2\sigma_1} \right) \right] \quad (3.4)$$

While the imaginary component simplifies to the form

$$\text{Im}[K(\omega)] = \left[\frac{3\omega(\varepsilon_2 \varepsilon_1 - \varepsilon_1 \sigma_2)}{\omega^2(\varepsilon_2 + 2\varepsilon_1)^2 + (\sigma_2 + 2\sigma_1)^2} \right] \quad (3.5)$$

For a nanotube or nanowire, which is another typical shape of nanomaterial and characterized by a cylindrical shape, DEP force is given by [102]

$$\mathbf{F}_{DEP} = \frac{\pi}{6} r^2 l \varepsilon_1 \text{Re}[\mathbf{K}_w(\omega)] \nabla |\mathbf{E}|^2 \quad (3.6)$$

$$\mathbf{K}_w(\omega) = \frac{\varepsilon_2^* - \varepsilon_1^*}{\varepsilon_1^*} \quad (3.7)$$

Where r is the radius, and l is the length of the cylinder.

The DEP force depends on the magnitude and sign of $\text{Re}[\mathbf{K}(\omega)]$. Nanomaterial trapped of DEP process is the positive dielectrophoresis which is defined by

$Re[\mathbf{K}(\omega)] > 0$. Particle are attached to electric field intensity maxima and repelled from minima. In the other hand, negative dielectrophoresis is defined by $Re[\mathbf{K}(\omega)] < 0$. Particle are attached to electric field intensity minima and repelled from maxima.

I simulated and plotted the Clausius-Mossotti by using MATLAB (ver. R2021a) for Equation (3.2) and (3.7). The particles and mediums calculated are assigned as

Case 1: $\varepsilon_2 > \varepsilon_1, \sigma_1 > \sigma_2$

$\varepsilon_1 = 2.5\varepsilon_0 \text{ F/m}$, $\varepsilon_2 = 10\varepsilon_0 \text{ F/m}$, $\sigma_1 = 4 \times 10^{-8} \text{ S/m}$, and $\sigma_2 = 4 \times 10^{-8} \text{ S/m}$

Case 2: $\varepsilon_1 > \varepsilon_2, \sigma_2 > \sigma_1$

$\varepsilon_1 = 10\varepsilon_0 \text{ F/m}$, $\varepsilon_2 = 1\varepsilon_0 \text{ F/m}$, $\sigma_1 = 10^{-8} \text{ S/m}$, and $\sigma_2 = 10^{-7} \text{ S/m}$

Both graphs show the sign of $Re[\mathbf{K}(\omega)]$ were changed with varied frequency leading to direction change of DEP as shown in Figure 3.3 and Figure 3.4. Therefore, in the practice of sensor fabrication by using DEP, I investigated and selected the appropriated frequency to make the positive-DEP as 100 kHz.

3.4 DEP trapping based fabrication of nanomaterial gas sensor

Figures 3.5a and b [101] illustrate the positive and negative dielectrophoretic effects for two distinct electrode geometries. In the concentric cylindrical geometry of Figure 3.5a, the observed force is parallel to the vector of the electric field, that is, $\mathbf{F}_{DEP} \parallel \mathbf{E}$. On the other hand, between the nonparallel electrode plates shown in Figure 3. 5b, the DEP force, and the electric field vector are orthogonal, $\mathbf{F}_{DEP} \perp \mathbf{E}$. In the general case, the force vector \mathbf{F}_{DEP} can have any orientation concerning the electric field vector \mathbf{E} .

As described above, if the dielectric properties of the particles are different from the suspension medium. The particles are accumulated and trapped on microelectrodes. They are leading to changes in the impedance between the electrode gaps.

We propose a dielectrophoretic integration method that extends the particle manipulation technology in the field to the nanoscale and presents a gas sensor. The advantages of DEP are as follows.

1. Low cost without the need for special equipment
2. Orientation of nanomaterials in the electric field direction
3. Integrate any nanomaterial on any metal electrode
4. Real-time monitoring of nanomaterial integration process with impedance

measurement

The biggest advantage of the DEP fabrication technique described is a quantification of the amount of trapped nanomaterials on a real-time basis by monitoring the electrical impedance of the sensor by using dielectrophoretic impedance measurement (DEPIM) [69]. DEPIM is helpful to precisely control and calibrates the response of the nanomaterial-based sensors.

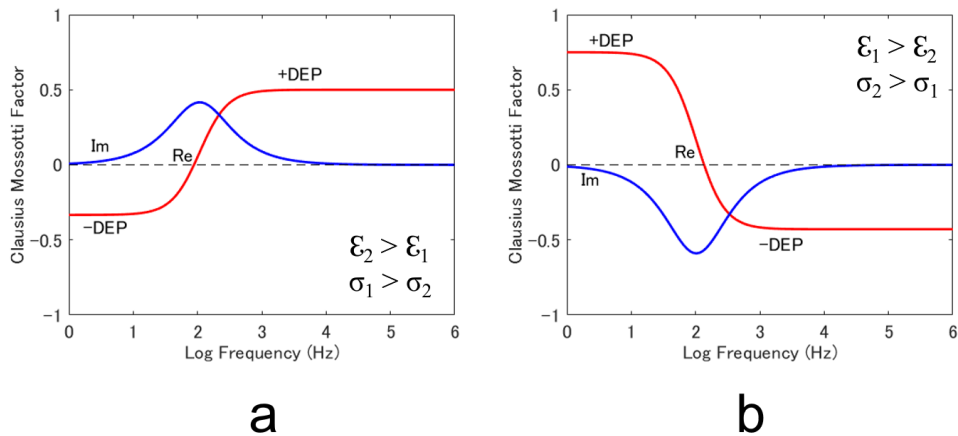


Figure 3.3. Clausius-Mossotti factor using Equation (3.2) (a) Case 1 (b) Case 2

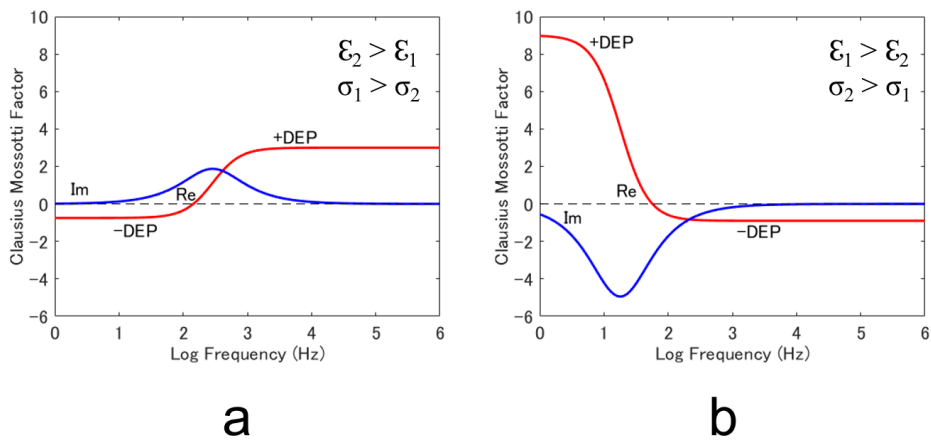


Figure 3.4. Clausius-Mossotti factor using Equation (3.7) (a) Case 1 (b) Case 2

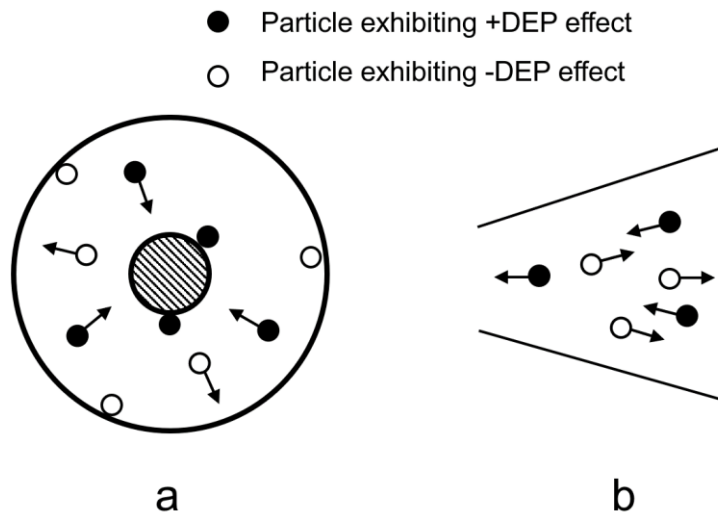


Figure 3.5. Positive and negative dielectrophoretic effect in different electrode structure [101]

(a) Electric field parallel to its gradient: $F_{DEP} \parallel E$

(b) Electric field vector perpendicular to its gradient: $F_{DEP} \perp E$

As previous works of our lab, they have already confirmed dielectrophoretic force as positive-DEP or negative-DEP of their applications by DEP [69-74]. Briefly, as mentioned earlier, Figure 3.6 illustrate the positive electrophoretic effect for my electrode geometry used for sensor fabrications. Figure 3.6a show particle behavior movement concept of particle under DEP process. The results of simulation by using COMSOL Multiphysics (ver. 5.5), by using particle tracing for fluid flow, creeping flow and electric current for physics interfaces, shows in Figure 3.6b-f, Figure 3.6b and 3.6c show the electric field region and velocity of medium flow. Figure 3.6d and 3.6e show particle behavior movement in case of without and with dielectrophoretic force. It was clearly understood that the trapping of particles on high filed region of electrode system.

The total force F_{total} acting on the particle mass m under DEP process

$$F_{total} = F_{DEP} + F_v + F_g + F_{flow} = m\mathbf{a} \quad (3.8)$$

Where F_v is the viscous force

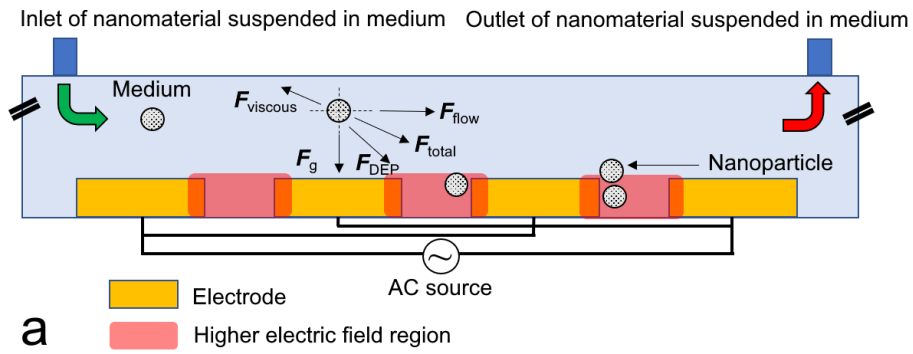
F_g is the gravitational force

F_{flow} is the force of medium flow

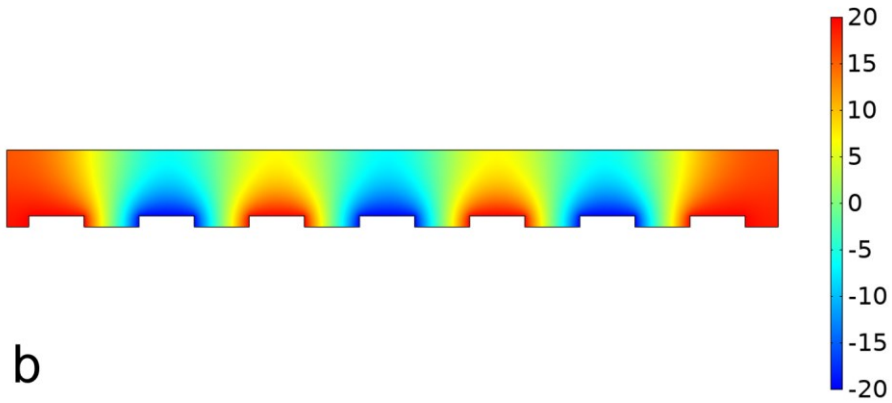
\mathbf{a} is acceleration

Properties of nanomaterial used as the gas sensor transducer are shown in Table 3.1. The SnO₂ nano-particles were suspended with the three different concentrations to investigate effects of the number of nanoparticles trapped on the microelectrode and the name list of sensors are shown in Table 3.2.

The Cr microelectrode used in the experiments was an interdigitated type. It had four electrodes fingers and three straight gaps. The electrode fingers had 12 mm in length and 50 μm in width. The gap between electrode fingers is 5 μm. The microelectrode was patterned on a glass substrate by using the photolithography technique. The microelectrode and the dimension of the electrode are shown in Figures 3.7a and 3.7b, respectively. Figure 3.7c shows the comparison size between the gas sensor and 100 YEN coin, which was the same size as each other.



freq(1)=1E5 Hz Surface: Electric potential (V)



freq(1)=1E5 Hz Surface: Electric field norm (V/m)



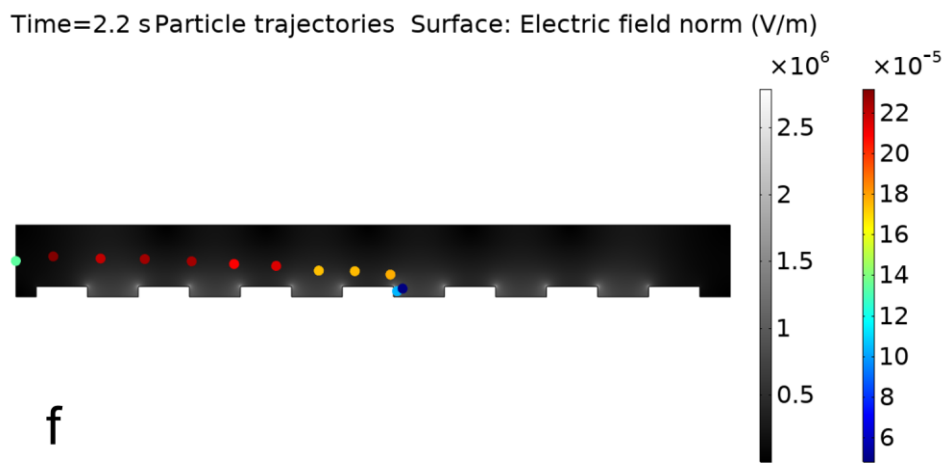
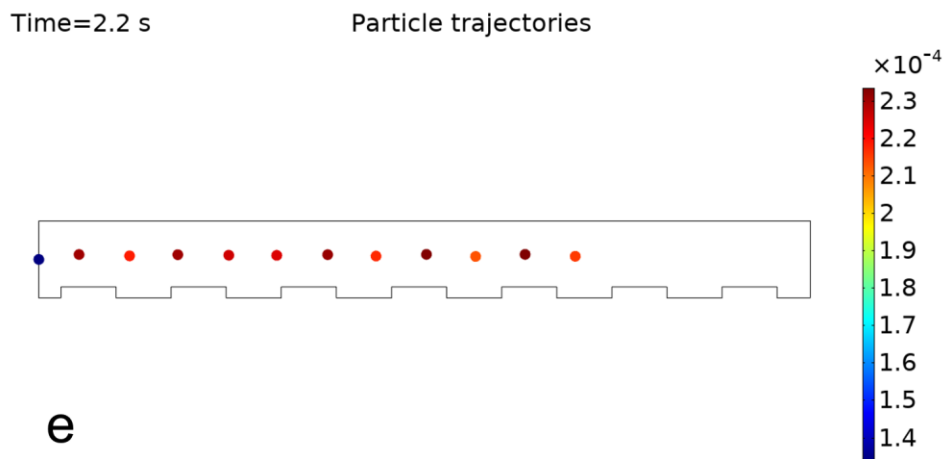
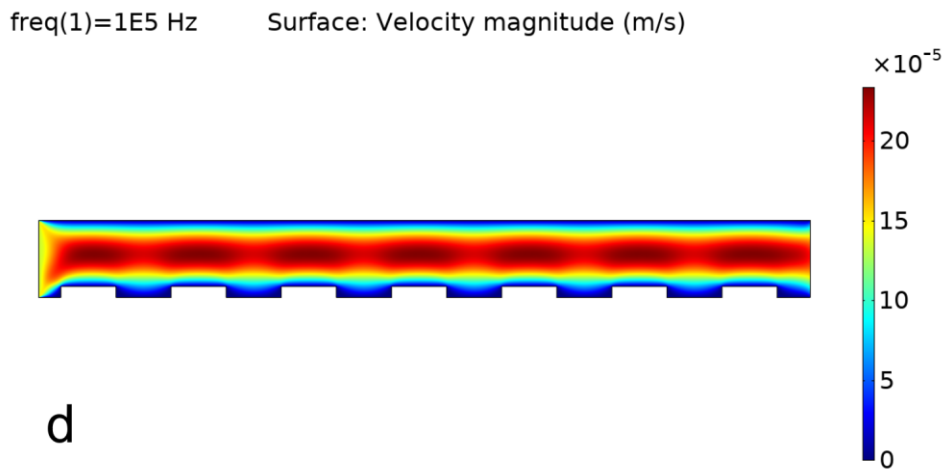


Figure 3.6. Positive electrophoretic effect (a) particle behavior movement concept (b) electric potential of electrode (c) electric field of electrode (d) medium flow (e) particle movement without +DEP (f) particle movement with +DEP

Table 3.1 Nanomaterials used as the gas sensor transducer.

Materials	Diameter	Length	Relative permittivity	Purchased from
SnO ₂ (particle)	15.9-136.7 nm	-	11.5	Kanto Chemical, Japan
ZnO (wire)	50 nm	300 nm	8.3	Sigma-Aldrich, Japan
SWCNT (tube)	1 nm	1 μm	2.5	Meijo Nano Carbon, Japan

Table 3.2 Name list and detail of fabricated sensors.

Sensor	Material	Medium (relative permittivity, conductivity)	Concentration
A-1s	SnO ₂	Ethanol (25.2, 0.219 μS/cm)	1 mg/ml
A-2s	SnO ₂	Ethanol (25.2, 0.219 μS/cm)	5 mg/ml
A-3s	SnO ₂	Ethanol (25.2, 0.219 μS/cm)	20 mg/ml
B-1s	ZnO	Ethanol (25.2, 0.219 μS/cm)	50 μg/ml
C-1s	CNT	Water (79.9, 5.5 μS/m)	0.1 mg/ml

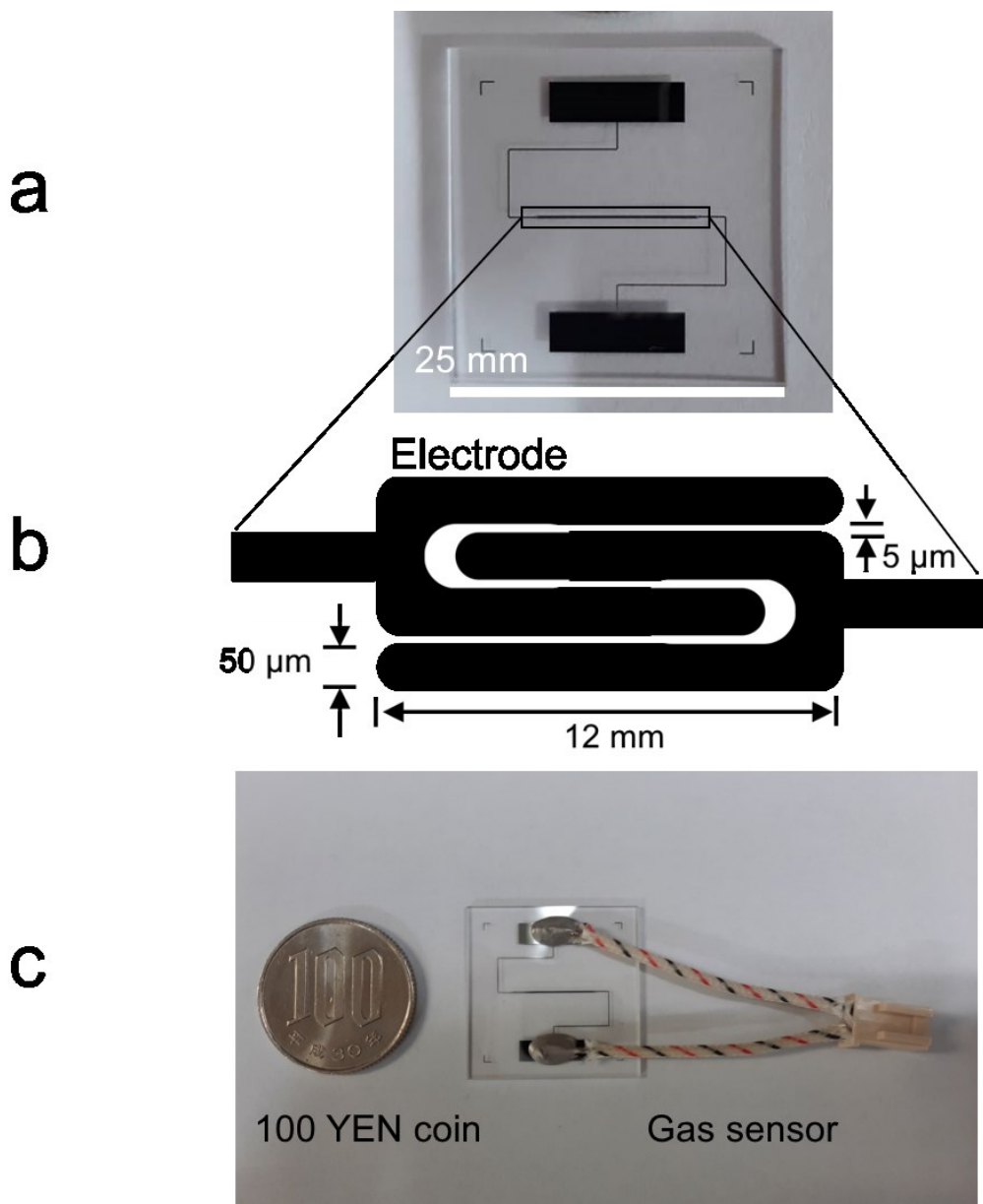


Figure 3.7. The structure detail of gas sensor (a) microelectrode (b) schematic of electrode finger (c) size comparison between gas sensor and 100 YEN coin

A schematic diagram of the DEP-based fabrication setup of nanomaterial-based gas sensors and the equivalent circuit is shown in Figure 3.8.

Figure 3.8a shows the experimental setup of the DEP process. The microelectrodes were covered by a silicone rubber spacer, which has the inlet and outlet for nanoparticle suspension injection from a peristaltic pump (SMP-21AS, AS ONE) at a flow rate of 0.8 ml/min. The microelectrodes were connected to the integrated circuit of

a function generator and lock-in amplifier.

Figure 3.9b shows the equivalent circuit of the DEP process. Microelectrodes were applied at $20\text{ V}_{\text{peak-peak}}$, 100 kHz by a function generator (WF 1945 1CH, NF Electronic Instrument). The conductance between the electrodes was simultaneously measured by a lock-in amplifier controlled (5560, NF Electronic Instrument) by PC via the user interface application.

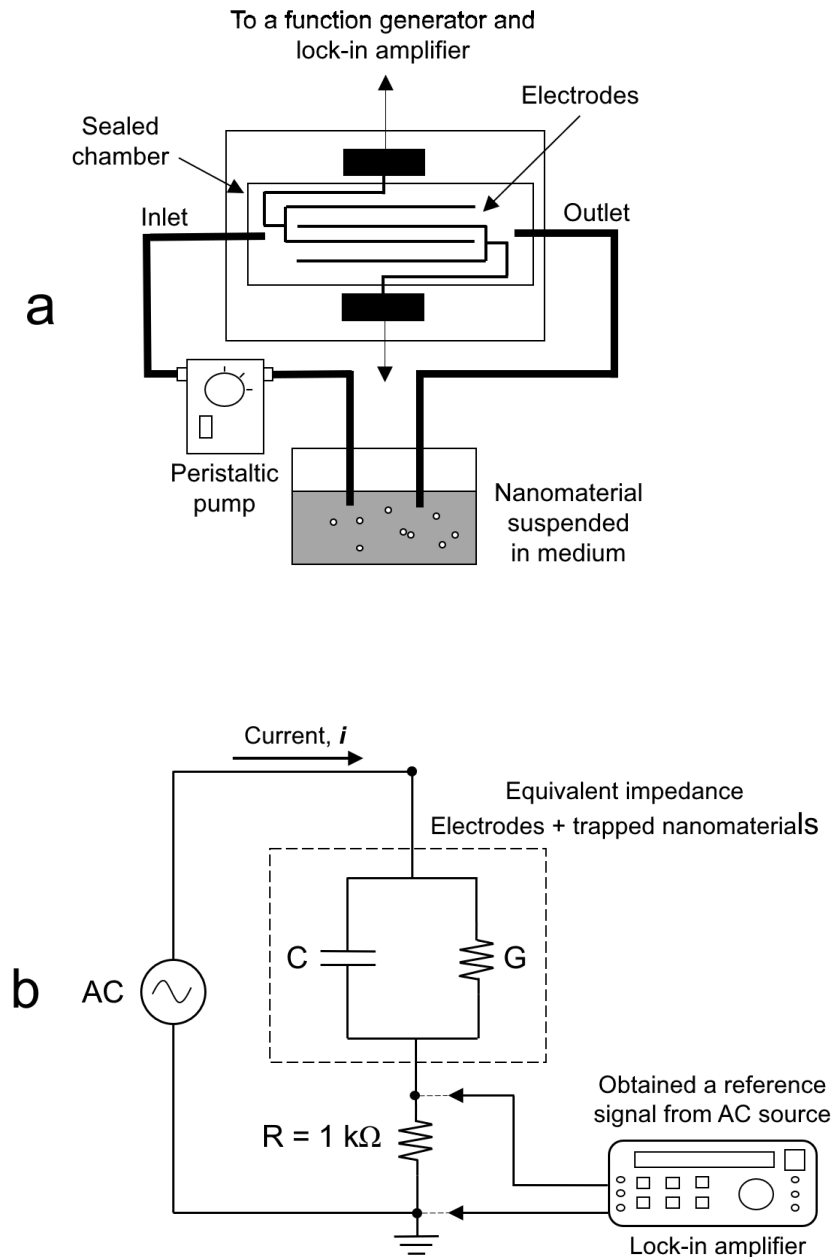


Figure 3.8. Dielectrophoresis process (a) schematic diagram (b) DEPIM equivalent circuit

Figure 3.9 shows the conductance change during DEP-trapping of the SnO₂ nanoparticles. The number of SnO₂ nanoparticles trapped on the microelectrodes varied with DEP time, (a) 15, (b) 30, (c) 45, and (d) 60 min. At 60 min-DEP time, it was clearly understood that the conductance between electrodes was increased and following the explanation in [69-70]. They explain using a simple equivalent circuit model of a particle trapped, which is the model as the parallel sum of the individual particle. The DEP fabrication and impedance monitoring could control the initial conductance of the sensor and the resultant sensor response. The DEP fabrication method enables the control the number of nanoparticles trapped on the microelectrode by the impedance measurement. At this stage, we desired to select the 60 min-DEP time for sensor fabrication. Because their conductance seemed to be stable. However, this time, I did not observe the effect of DEP trapping-time against CF₄.

In my idea, I think a thin layer (short time of DEP trapping) might be fast sensing than multilayer (long time of DEP trapping) because, for multilayer, it seems that equivalent circuit will be series and parallel connection of particle. The sensing layer should be the outer layer only. But that time, I could not do that because some conditions limited it. However, in stable conductance (60 min), I think it gives me the advantage of comparing all sensors in the condition of maximum conductance from the DEP process.

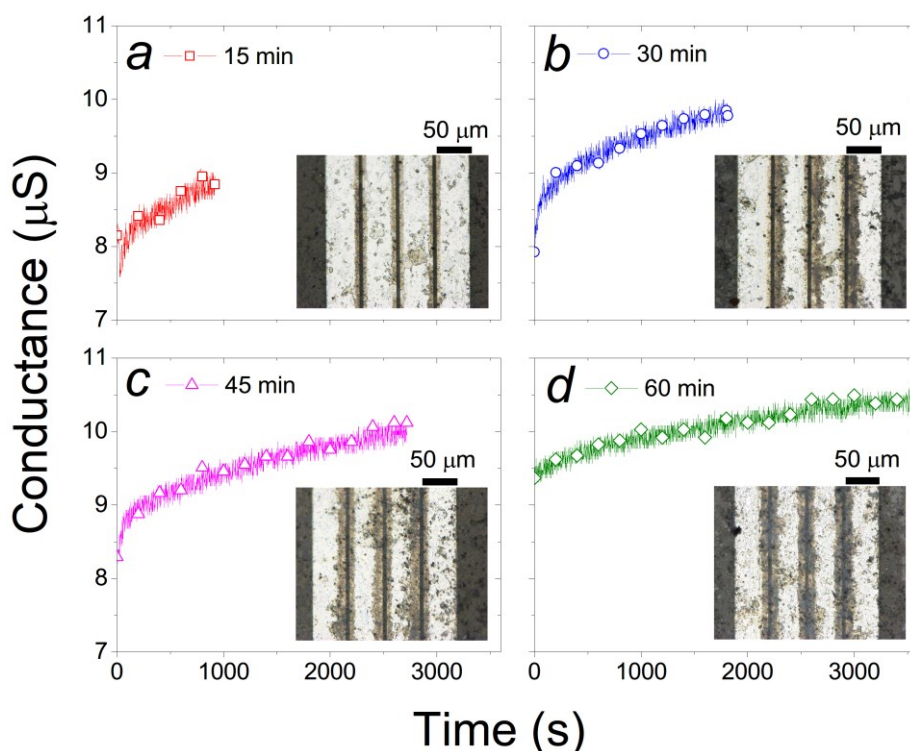


Figure 3.9. The conductance changes and the number of SnO_2 nanoparticles trapped on the microelectrodes varied with DEP time:(a) 15 min (b) 30 min (c) 45 min (d) 60 min. Inset photos are images of the microelectrode after DEP trapping.

Figure 3.10 shows the conductance of sensors fabricated by 60 min-DEP. After the DEP process was stopped, the liquid on the microelectrode was gently evaporated at room temperature (RT), keeping them in the chamber which is controlled humidity. The conductance_{dry} of the fabricated sensors were measured after ethanol evaporation (24 h after DEP process). The conductance of the dried sensor was lower than that of wetted sensor with ethanol. In my opinion, getting these results due to the conductivity of ethanol is greater than the conductivity of air. I was considering the conductance between SnO_2 particles when suspended in ethanol and air, where the conductivity of particles is constant. Suppose assuming that SnO_2 and media are connected in series. The conductivity of the sensor suspended in ethanol would be greater than in air.

The conductance of sensors before and after dry was shown in Figure 3.11. The scanning electron microscope (SEM) was used for observation of nanomaterial trapped on the microelectrode as shown in Figure 3.12.

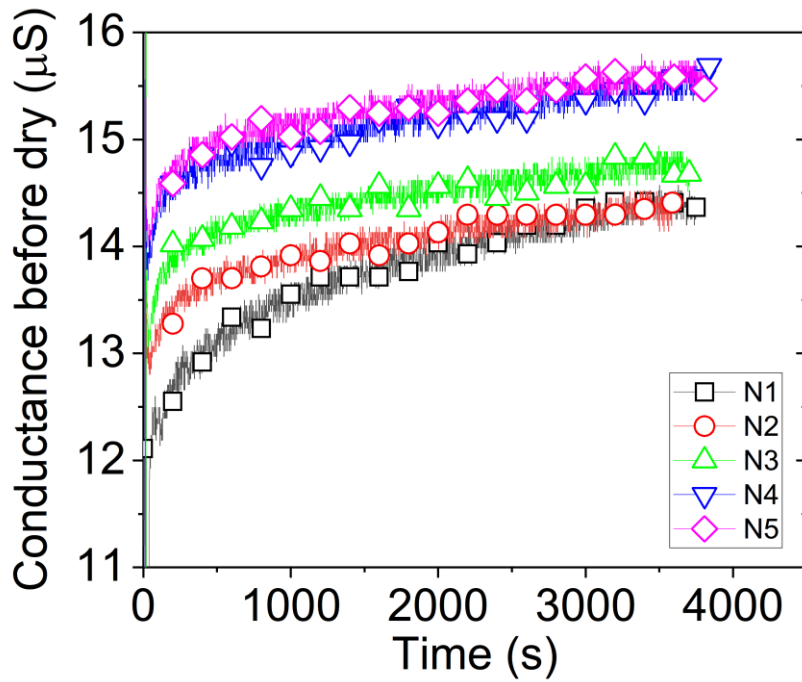


Figure 3.10. Temporal change of the microelectrode conductance during DEP process. N1–N5 indicates SnO₂ sensors fabricated independently.

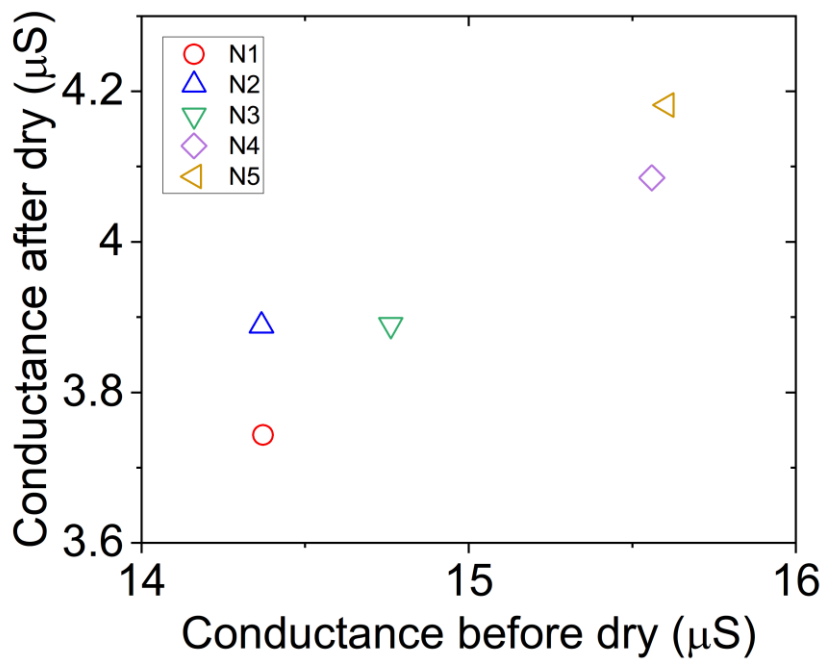


Figure 3.11. Relationship between the conductance measured before and after ethanol evaporation. N1–N5 indicates SnO₂ sensors fabricated independently.

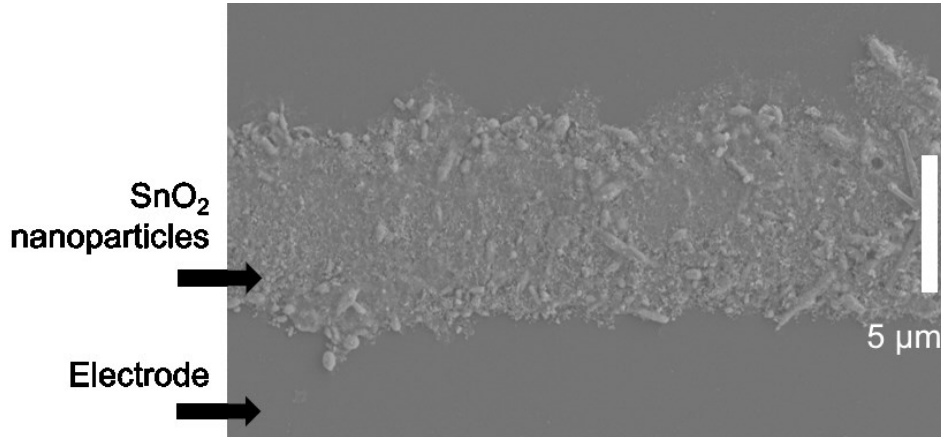


Figure 3.12. SEM image of SnO₂ nanoparticles trapped between the microelectrodes.

3.6 Experimental apparatus for gas sensor performance

Figure 3.13 shows the schematic diagram of the experimental setup for the investigation of the sensing response of the nanomaterial-based gas sensors. The sensor was placed in a chamber made of stainless steel (Volume: 1400 cm³), and the working temperature was controlled by a ceramic heater (Adjusting range: 20 – 300 °C). AC voltage, 1 V_{peak-peak} energized the sensor, and 100 kHz of frequency (WF 1945A 1CH, NF Electronic Instrument), and the sensor conductance was measured by a lock-in amplifier (7280 DSP, PerkinElmer/EG&G) controlled by PC via user interface application (LabVIEW, 2019, SP1). The gas flow rate was controlled by a mass flow control unit (STEC, MU-3406, Horiba, Kyoto, Japan). CF₄ gas was diluted by SF₆ gas to 1% (10000 ppm) concentration.

The sensor was exposed to SF₆ gas in the initialization stage until a steady baseline was attained (approximately 2 hr.). After that testing stage, the exposing gas sequences were included the initialize gas (SF₆) for time 300 s, exposing the target gas for time 600 s and backed to initialize gas for time 600 s. The sensing response was shown as the normalized values of conductance of the sensor. The given equation calculates the normalized response of the sensor

$$\frac{\Delta G}{G_0} = \frac{G_a - G_0}{G_0} \quad (3.9)$$

where G_0 is the conductance in initialize gas and G_a is the conductance in the presence of the target gas. Response time is expressed in term of time (t_R) needed for 90% of full response. Figure 3.14 shows the apparatuses of direct CF_4 detection system. Figure 3.15 shows the user interface application screen on PC for monitoring the sensor response by LabVIEW (2019, SP1) and the gas exposure sequence used in this study is showed in Figure 3.16.

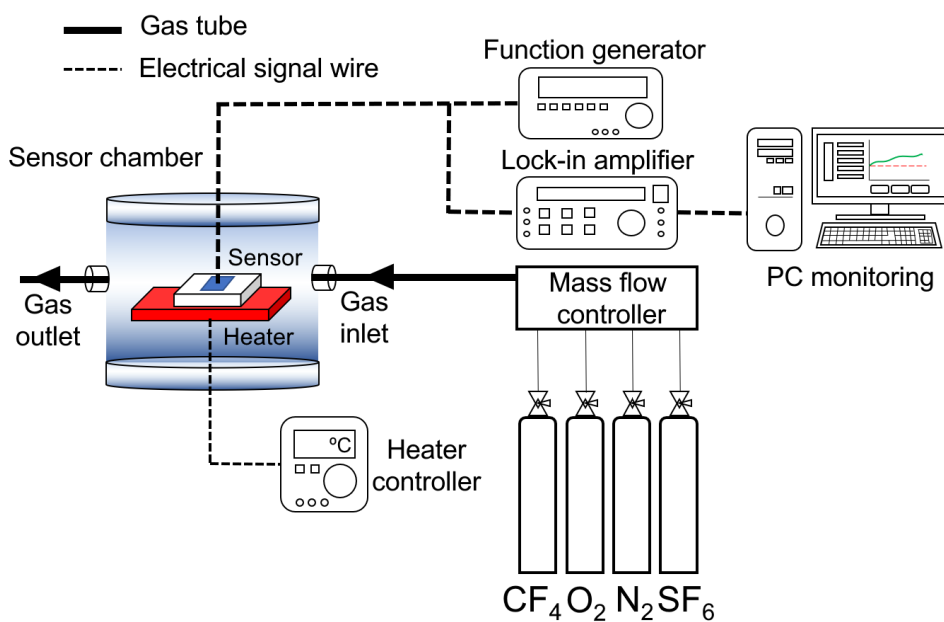


Figure 3.13. Experimental setup of direct CF_4 detection.

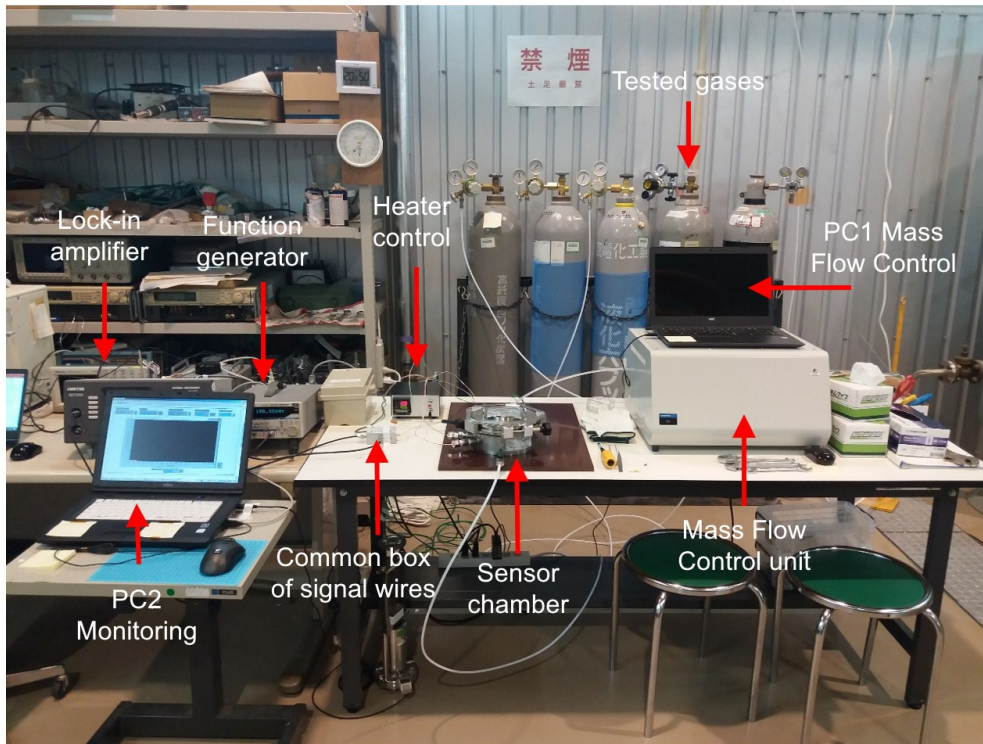


Figure 3.14. Apparatuses of direct CF₄ detection

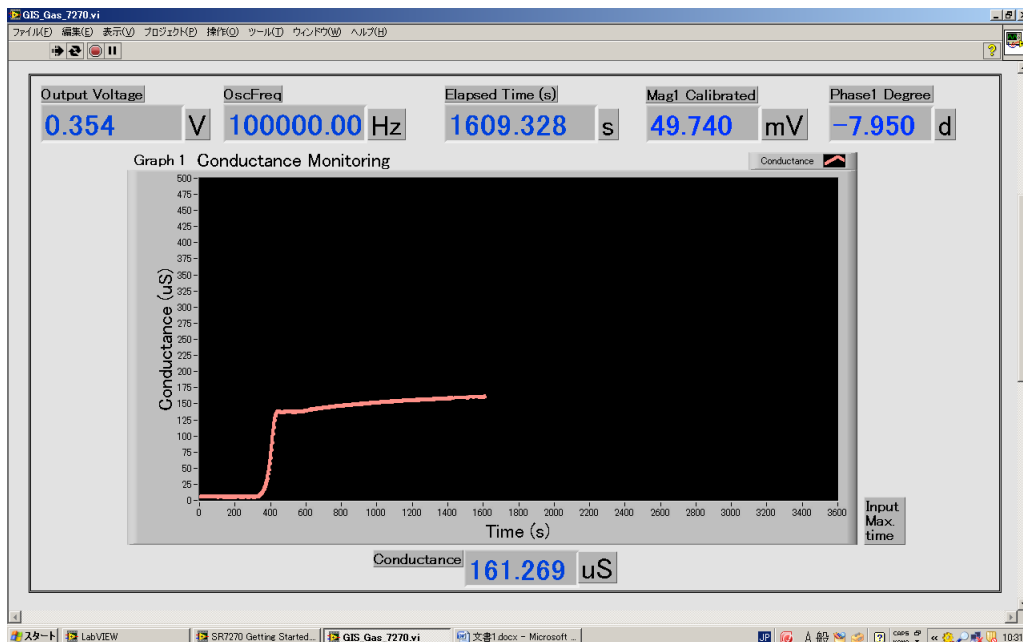


Figure 3.15. User interface application screen on PC for monitoring sensor response

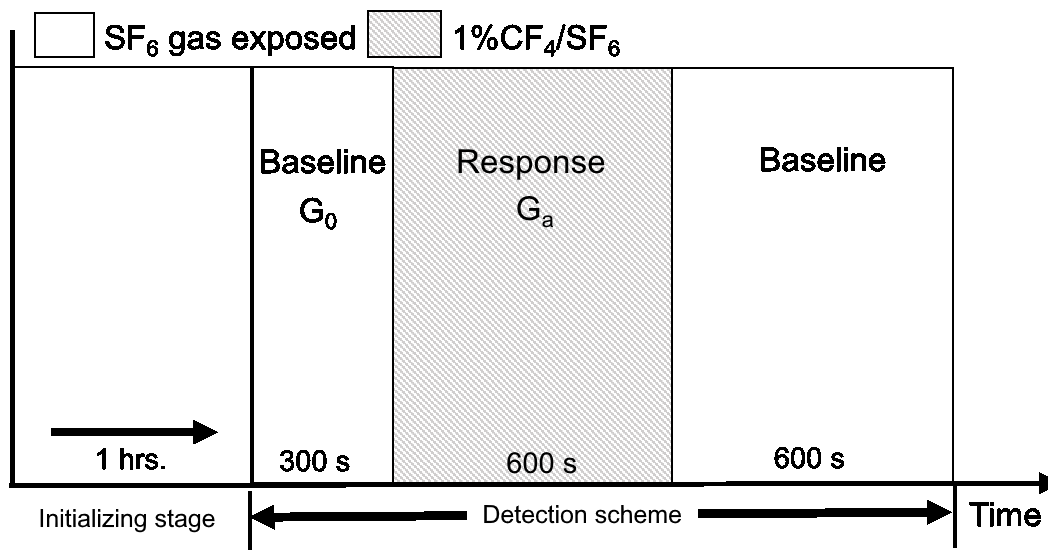


Figure 3.16. Tested gas sequences

3.7 Effect of transducer material and operating temperature

Figure 3.17 shows CF_4 response in comparison of three gas sensors, which were made of different nanomaterials (see Table 3.2). The highest response was obtained with the A-2s sensor, which was made of SnO_2 nanoparticles, 5 mg/ml. The B-1s sensor (ZnO nanowire) response was about 30% of A-2s, while the C-1s sensor (CNT) showed little response.

Operating temperature dependency of these sensors are shown in Figure 3.18. The temperature dependency of A-2s and B-1s demonstrated a similarity. Their responses were the highest at RT and decreased with the temperature below $200^\circ C$. Above $200^\circ C$, the response increased with the operating temperature. C-1s sensor response became the highest at $200^\circ C$.

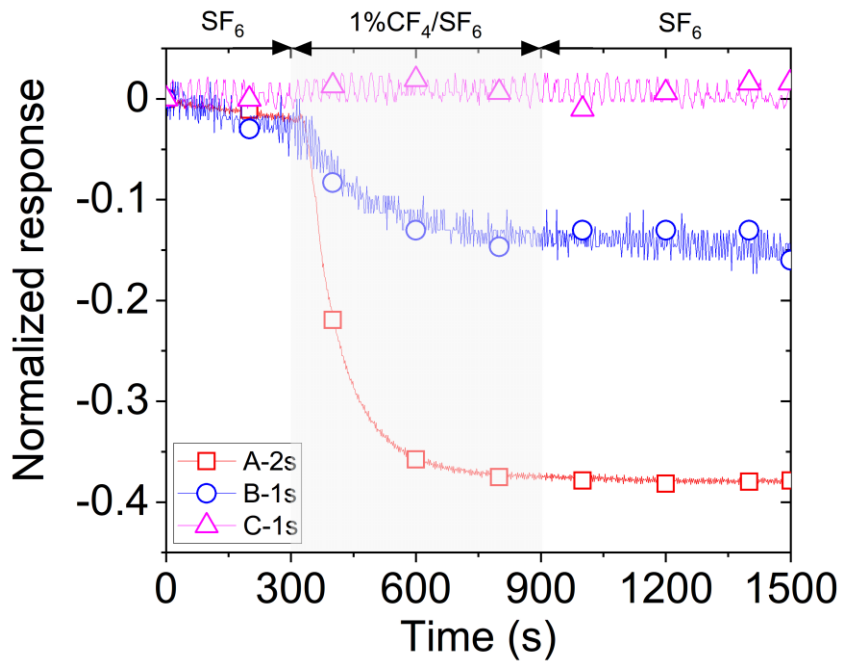


Figure 3.17. Response of sensors against CF₄ at room temperature of A-2s, B-1s, and C-1s [90].

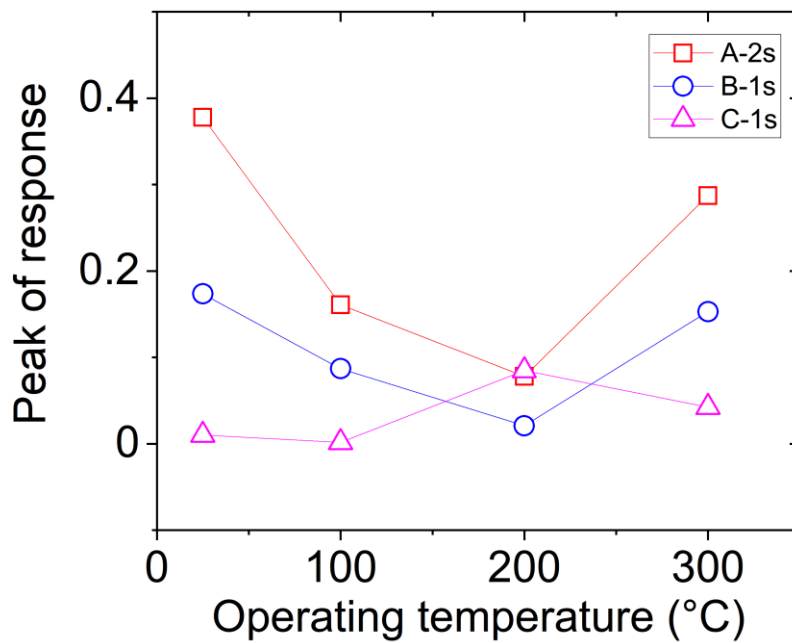


Figure 3.18. Response of sensors against CF₄ at various temperatures of A-2s, B-1s, and C-1s [90].

Figure 3.19 shows temporal variation of A-2s sensor response to CF₄ gas. As shown in Figure 3.18, the peak value of the sensor response became the highest at RT. On the other hand, the sensor response time tended to become faster at elevated temperature. Table 3.3 compares response times (t_R) and peak values (p_v) at RT and 300°C. Figure 3.19 also demonstrates that the sensor conductance showed a peak value at elevated temperatures, while monotonously increased with time at room temperature. This result implied CF₄ sensing mechanism of SnO₂ nanoparticle-based sensor depended on the temperature. Basic working principle for gas detection using metal oxide material is explained above. The sensing mechanism is discussed in section 3.10.

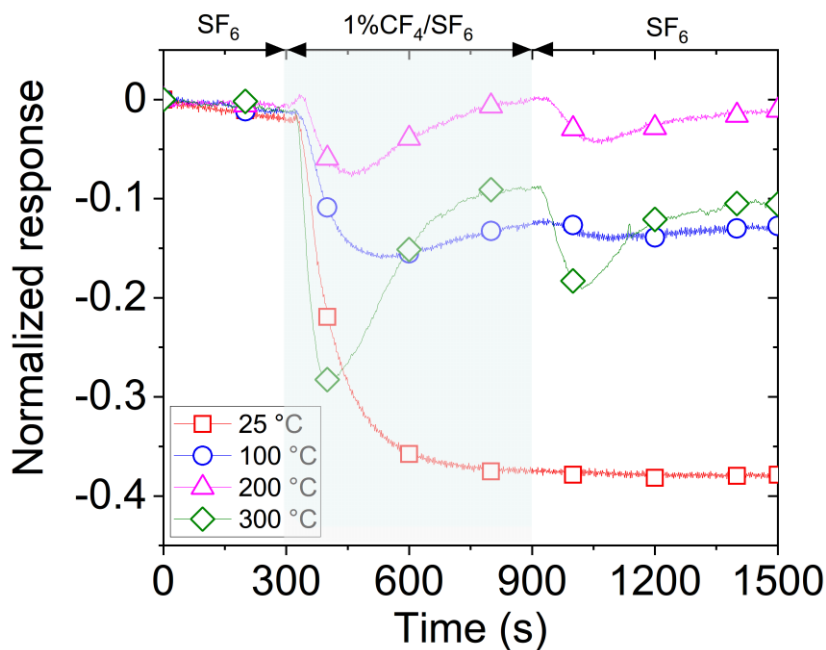


Figure 3.19. Effect of the temperature on temporal variation of the A-2s sensor response [90].

Table 3.3. Effect of the temperature on the response times t_R and peak values p_v of the A-2s sensor response.

Temperature	t_R (s)	p_v
RT	230	0.37
300 °C	74	0.28

3.8 Effect of nanoparticle suspension concentration

In the DEP fabrication process, the amount of nanomaterial (transducer) trapped on the microelectrode can be controlled by the concentration of nanomaterial suspension. I investigated how the SnO₂ nanoparticle amount influences the sensor response. The results are shown in Figure 3.20. It was found that the sensor response depended on the SnO₂ nanoparticles concentration. The highest response occurred at 5 mg/ml concentration. It was probably due to enhanced agglomeration of nanoparticles which reduced effective gas adsorption sites on their surface.

3.9 Reproducibility of SnO₂ gas sensor

As shown in Figure 3.18, it was noticed that the SnO₂ gas sensor showed the highest response at RT. In the case of RT without any temperate control, it cannot be controlled the exact temperature, approximately 15 – 25 °C. Therefore, determination of the working temperature-controlled will be demonstrated higher stability of sensor response. In this section, I selected 150 °C to working temperature and tested reproducibility and repeatability performance.

Figure 3.21 shows the responses of independently developed nine sensors (P1-P9). Those sensors were operated at 150°C. The normalized responses were in a range between 0.1-0.22. Average and standard deviation of the values are 0.16 and 0.03, respectively (coefficient of variance is 18.8%). Figure 3.22 shows repeatedly response of the three sensors (P10-P12). Comparison of first-time and second-time response, the results show that the response of second time was 25% of first-time response. These results suggested that the CF₄ could poison the SnO₂ nanoparticles.

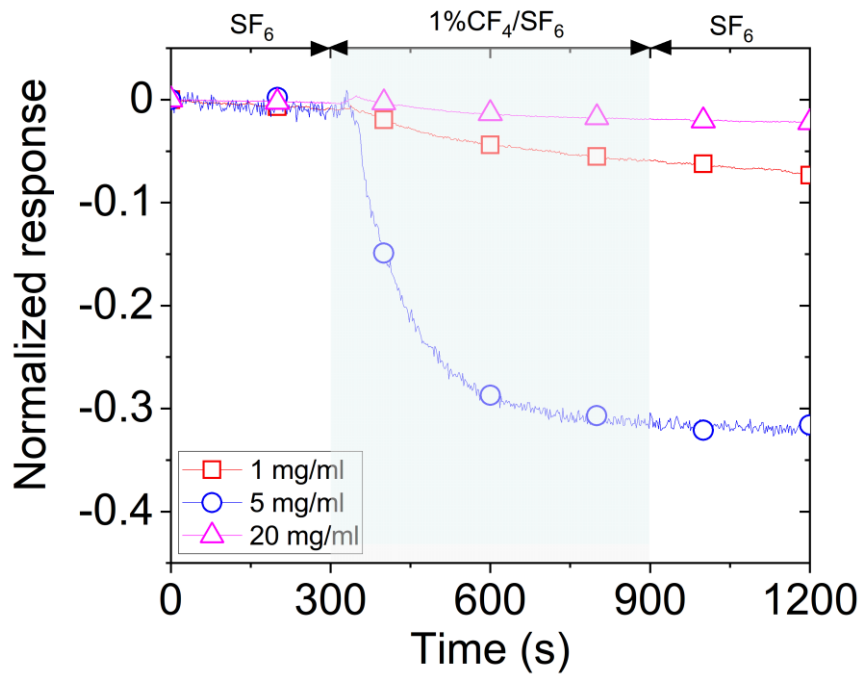


Figure 3.20. Effect of SnO₂ nanoparticle suspension concentration on the CF₄ gas response [90].

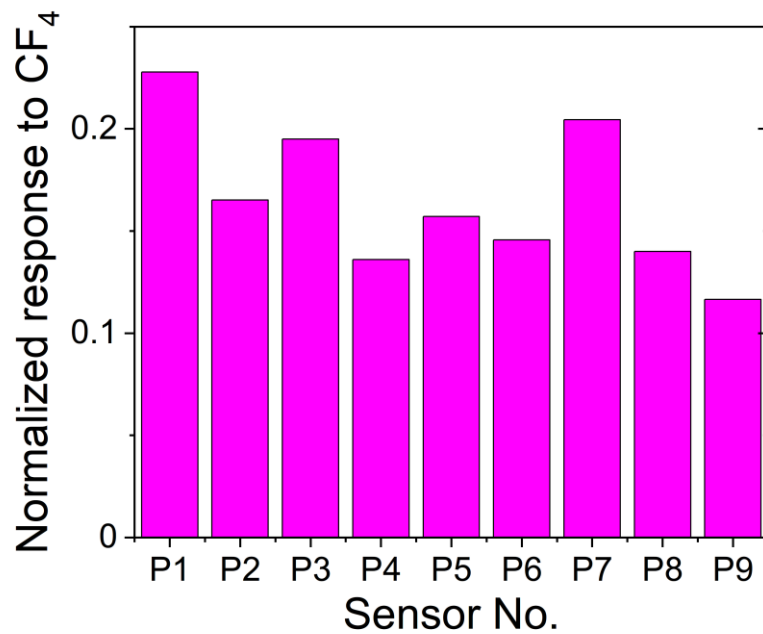


Figure 3.21. CF₄ responses of the nine sensors

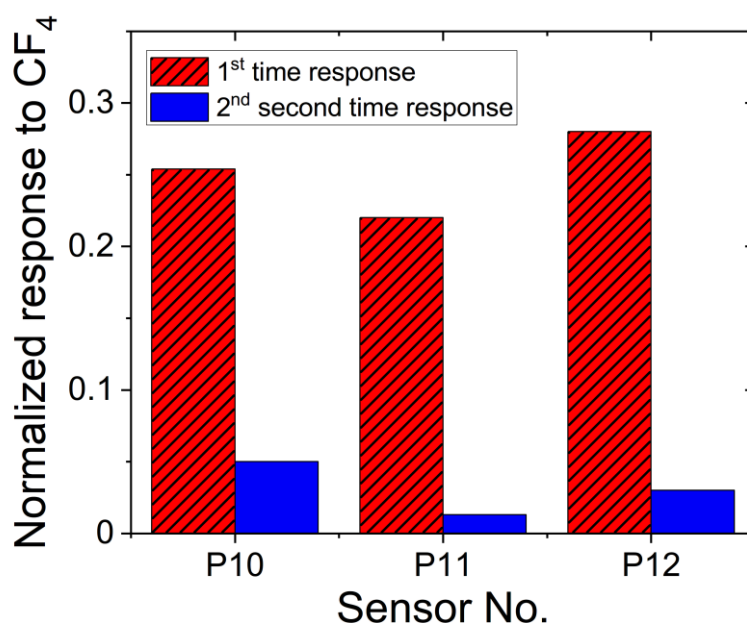


Figure 3.22. 1st and 2nd responses of the sensors

The reproducibility investigation shows there was individual difference in the DEP-fabricated SnO₂ gas sensor. To calibrate the individual differences between the sensors, we tried to utilize NO₂ as the calibrator. It is well-known that NO₂ is a gas which can be detected by semiconductor gas sensors repeatedly. Figure 3.23 shows the sensor responses (P4-P9) against NO₂ before and after testing against CF₄. It was found that the NO₂ responses of all sensors after testing against CF₄ were decreased from before testing against CF₄. In this time, it was not clear why the ability of the sensor was decreased but it provided some evidences to suggest that there was the reaction between CF₄ and SnO₂ sensor.

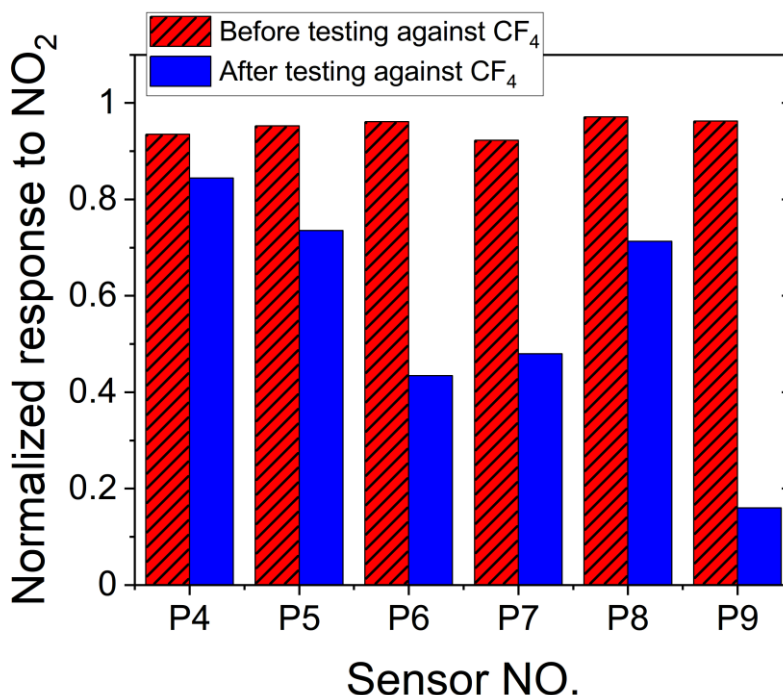


Figure 3.23. NO₂ response of the sensors before and after experience the exposed by CF₄

3.10 Discussion

Although, the chemical sensing mechanism and reaction pathway between nanomaterial-based gas sensors and CF₄ were still unclear, and there is a lack of research on this reaction. The SnO₂ gas sensor could detect CF₄, but the detection lower limit was approximately 10,000 ppm, which was not sufficient for the GIS diagnosis. This low sensitivity might be due to weak CF₄ adsorption energy on the SnO₂ surface [103]. For one example of SnO₂ response studies, Zhang and Meng [104] reported the detection of 500-ppm CF₄ using a gas sensor based on single-walled CNT modified with a hydroxyl group (SWCNT-OH). The result shows that 0.8% of response sensitivity and 7 min of response time. Their gas sensor had cross sensitivities to other decomposition gases, such as SO₂, SOF₂, and SO₂F₂. However, its capability was not enough to detect the level of CF₄. We would like to conclude that the direct CF₄ detection may be difficult.

In GIS, the sample gas consists of not only CF₄ but also many gas species such as SO₂, HF, and SO₂F₂. Thus, the cross-sensitivity performance of gas sensors should consider and discuss carefully.

As mention above, I have another choice that might improve the sensitivity of the sensors. I would set the further work to study a combination of nanomaterials for gas

sensors fabricated by DEP. They were supposed to improve the sensitivity to the target gas, whether it be CF_4 , CO , or CO_2 . These topics would be discussed and demonstrated some experimental results in Chapter 5.

3.11 Summary

Three kinds of semiconducting nanomaterials, carbon nanotube, SnO_2 nanoparticle, ZnO nanowires, were integrated on a microelectrode by dielectrophoresis fabricate a gas sensor. It was found that the SnO_2 gas sensor showed the highest response to CF_4 gas at 10000 ppm concentration in SF_6 . The conductance of the SnO_2 sensor gradually decreased with elapsed time after exposure to the CF_4 gas, depending on the operating temperature. SnO_2 gas sensors fabricated by DEP could detect CF_4 , but there was a limitation. Because CF_4 may poison the SnO_2 , the sensor could be used once. Although the reproducibility was not high, the calibration of the sensor using NO_2 would overcome it. In the future, the study of the mechanism of the reaction between CF_4 and SnO_2 would be made clear to improve the performance of the sensor.

The novelty of this technique is using the nanomaterial-based gas sensor to detect CF_4 under the limitation of 10000 ppm- CF_4 concentration. The strong point demonstrated in terms of an inexpensive sensor fabricated by the dielectrophoresis method.

Aiming to an application for GIS diagnosis, nanomaterial-based gas sensors fabricated by DEP were applied. They show their response against CF_4 , but the responses seemed to be low when compared in the real-world of residual CF_4 in GIS. However, this method is one of the CF_4 diagnosis methods, and it is the starting stage. Improvement and new concept would be needed in the future.

Chapter 4

Indirect CF₄ detection by using nonthermal plasma application

4.1 Introduction

The proposed indirect CF₄ detection method is conceptually illustrated in Figure 2.6. The GIS sample gas is mixed with O₂. Then the gas is processed by DBD to convert CF₄ into CO and CO₂. If the conversion is perfect, the sum of CO and CO₂ corresponds to the amount of CF₄. The generated CO and CO₂ are detected by conventional gas sensors, which are available in the market. Because there are many requirements to detect the gases, we can find cheap but sensitive gas sensors from the market. In GIS, CF₄ is major decomposition gas containing carbon atom [45]. Even if CO and CO₂ have already existed in the sample gas, the proposed method should work by evaluating the increment of these gas concentrations after DBD treatment. This implies that CO and CO₂ detection in plasma-treated sample gas can be regarded as an alert for possible accumulation of residual CF₄ in the GIS. This chapter demonstrated the CF₄ conversion technique and the possibility for GIS diagnostic application [105].

Although, each species of decomposition gas generations rates depends on the types of discharge [46, 47, 106-107]. Therefore, in practical application, I would explain the pre-condition before taking the gas sample for indirect CF₄ detection:

1. After fault occurs, decomposition gases are generated in the case of involving the polymeric insulators.
2. CO₂ and CO, which are our target gases, are also generated.
3. In the case of an absorbent installed, decomposition gases removal takes 1-10 h [108, 109] or several days [45], except CF₄. After this period, it assumes that there is the only CF₄ exists in the gas compartment.
4. Without an absorbent, CF₄, CO, and CO₂ exist in the gas sample. For indirect detection, measurement of CO and CO₂ before and after DBD treatment is required to subtract generated gases. In this case, one or more extra steps are applied to estimate CO and CO₂ before DBD treatment. Moreover, under DBD application, CO could be oxidized into CO₂, while CO₂ may be converted into CO. Analysis of generation of CO and CO₂ might be complicated than in the case with an absorbent installed.

To date, chemical analysis of SF₆ decomposition gases generally was carried out by lab instruments, such as gas chromatography and FT-IR. As described earlier, the purpose of this study is to achieve indirect CF₄ detection by DBD-induced conversion into CO and CO₂. The converted gases can be detected using commercially available gas sensors. The commercially available gas sensors (below 50,000 yen) are cheap rather than expensive lab instruments (approximately 1.5 million yen). In the first stage of this study, it was investigated that DBD-induced CF₄ conversion process. It was confirmed by FT-IR-based gas analysis. Next, a commercial CO gas sensor was compared with FT-IR. Finally, discussion of this method in practical application are presented.

A DBD plasma was employed for CF₄ conversion because it has been widely used in various plasma processing applications owing to its simplicity and excellent performance [110]. Because DBD can be generated at atmospheric pressure, it can be operated at a lower cost than other plasma generation systems [80]. Figure 4.1 [111] shows the nonthermal plasma operation using a flow reactor or a closed reactor. In this case, the reaction mixture is far from the thermal equilibrium. The chemical conversions are initiated by the high temperature ($T_e \geq 104$ °K) of free electrons at relatively low gas temperature ($T_g \leq 103$ °K) (plasma electrical conversion). The processes take place under highly nonequilibrium conditions of all plasma species. Hot electrons, energetic ions, cold, excited species, free atoms, and radicals are produced in the so-called active zone (phase) of the different kinds of nonthermal (electrical) gas discharges. In the passive zone (phase), the electrons cool down fast. The unstable plasma components change to stable reaction products by volume and wall reactions.

In the case of a flow reactor, the target gas is introduced into a discharge channel continuously. In this case, the time for the DBD treatment depends on the flow rate. In the other case, in a closed reactor, no flow occurs when the DBD occurs. The closed reactor is filled with the target gas. Then, the reactor is closed. After the DBD treatment, the gas is recovered for analysis. In this case, DBD treatment is controlled by the switching of the power source. We would know the actual volume of sampling gas estimated by the same volume as gas treatment chamber volume. In a practical application, the volume of the sampled gas from GIS is limited. Controlling the DBD treatment time of the closed reactor is easier than that of the flow reactor. Therefore, it is suggested that the closed reactor should be more suitable for our concept.

DBDs are normally operated in one of the parallel-plate or cylindrical configurations illustrated in Figure 4.2 [112]. The parallel-plate design is used to surface treat fast-moving webs and films, and the annular volume of the cylindrical structure is used to treat airflows for ozone production. At least one electrode of these geometries is covered with an insulating dielectric barrier to prevent actual currents from flowing from the discharge volume to the electrodes and power supply. I selected the design of a parallel plate with a single dielectric layer (Figure 4.2b) because it is the most simple and easiest to construct, and no special apparatus needs to support the electrode configuration. The time scale of the relevant process of the filamentary barrier discharge is shown in Figure 4.3 [113]. The time constants of the relevant processes in barrier discharge cover many orders of magnitude. The development of micro discharge channels, which is characterized by the production of high-energy plasma electrons, takes place in the ns range. Otherwise, the phase of plasma chemical reactions by atoms, radicals, excited species, and short waved radiation typically starts within the ms scale. Their production is controlled by the plasma parameters of the micro discharges, namely by the reduced local electric field strength and electron density. Therefore, the knowledge of these parameters is of essential importance for the desired control of the final plasma process.

Our laboratory has demonstrated three kinds of plasma source configuration in previous research, as shown in Figure 4.4.

Phansiri *et al.* [114] reported using a needle to plane electrode configuration for CF₄ conversion into CO₂ detection by the SnO₂ gas sensor. The discharge gap between them was set at 5 mm, and the applied voltage was 12 kV_{rms}, 60 Hz as shown in Figure 4.4a.

Phansiri *et al.* [115] demonstrated the parallel plates electrode configuration for CF₄ conversion into CO and CO₂ detection by a gas analyzer. The discharge gap between the upper electrode and dielectric layer was set at 5 mm, and the applied voltage was 20 kV_{rms}, 60 Hz as shown in Figure 4.4b.

Miwa *et al.* [116] using the cylindrical electrode configurations for CF₄ decomposition shown in Figure 4.4c. The discharge gap between a high-volt electrode and dielectric layer was set at 5 mm, and the applied voltage was 22 kV_{rms}, 60 Hz.

During discharge occurred, all of the filament discharge photos were taken by digital camera with shutter speed 1/20 sec and ISO-400.

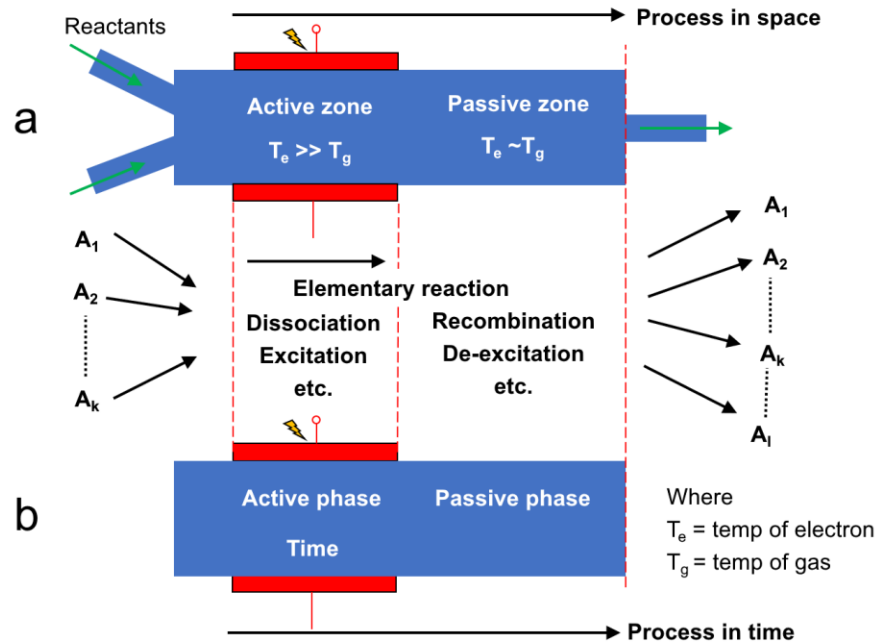


Figure 4.1. Operation scheme of a nonthermal plasma by (a) flow reactor and (b) closed reactor [111]. Active and passive zone, and dissociation and recombination zone between flow reactor and closed reactor.

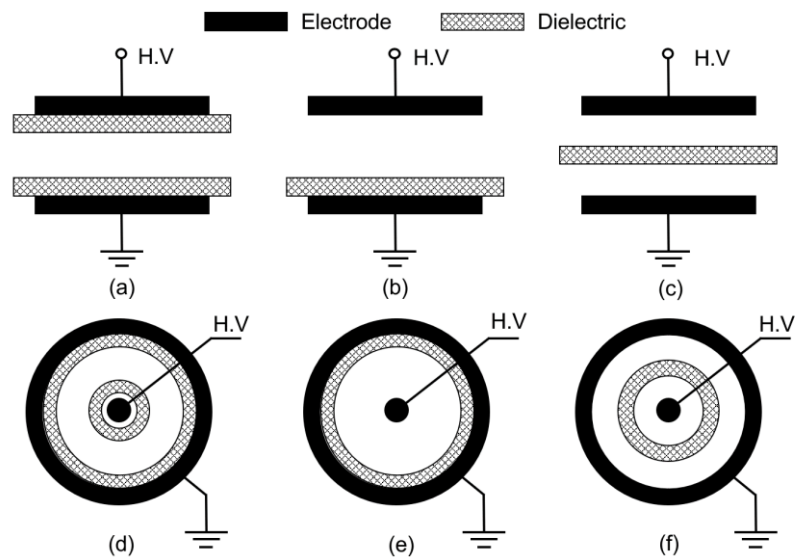


Figure 4.2. Schematic diagrams of (a)–(c) parallel-plate, and (d)–(f) cylindrical electrodes for DBD generation [112]. Electrode configurations commonly used in DBD application.

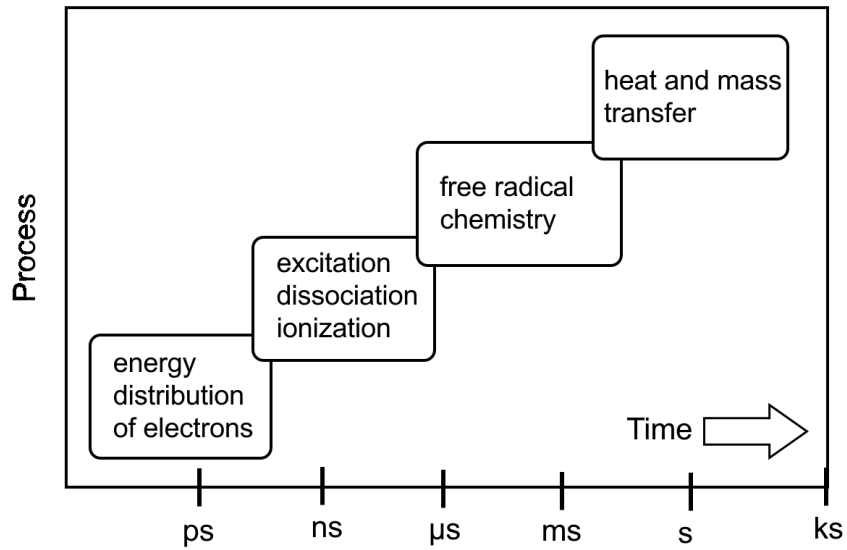


Figure 4.3. Time scale of the relevant process of the filamentary barrier discharge [113]. Show the time scale of dissociation and recombination.

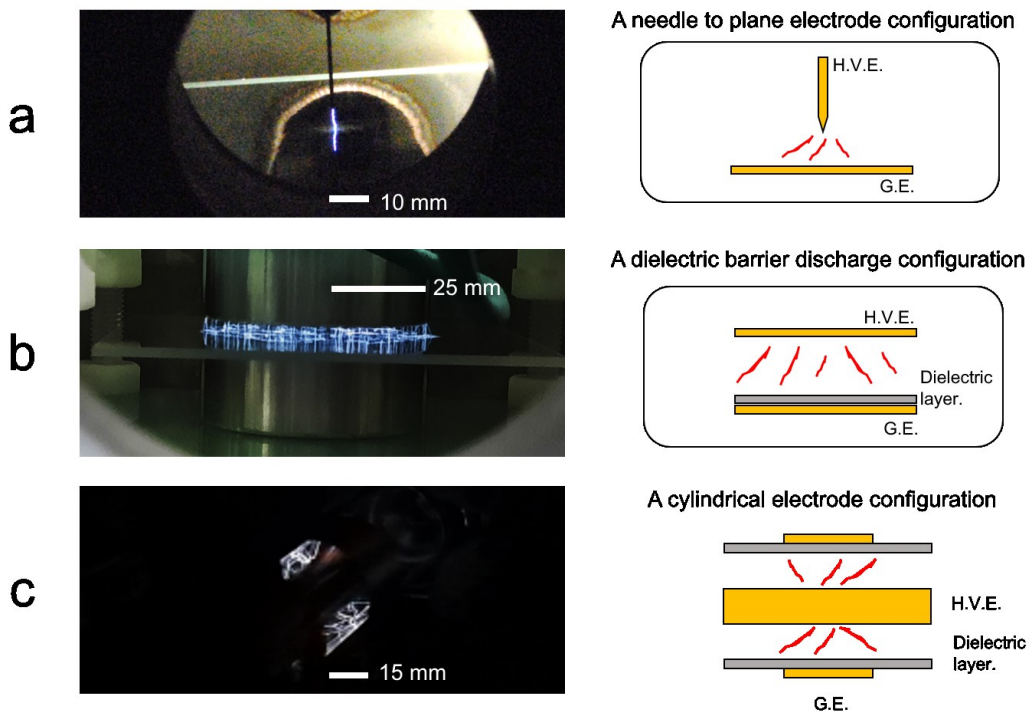


Figure 4.4. Plasma source configuration used in our laboratory (a) needle to plane (b) parallel-plate, and (c) cylindrical electrode configuration [114-116]. Suehiro and Nakano Laboratory demonstrated the application of three kinds of electrode configuration.

4.2 Experiments

4.2.1 DBD reactor and gas treatment chamber

Figure 4.5 shows a schematic diagram of the DBD reactor. Parallel aluminum round plate electrodes (radius: 25 mm; thickness: 20 mm) were placed in a stainless-steel gas treatment chamber (inner volume: 9,700 cm³). The distance between the electrodes was adjusted to 5 mm. A quartz dielectric plate (Heralux, Shin-Etsu Quartz Products Co., Ltd., Japan) (dielectric constant: 3.7; thickness: 2 mm) was placed on the surface of the ground electrode. The distance and volume between the upper electrode and the dielectric plate were 3 mm and 5.9 cm³, respectively. A high voltage transformer (60 Hz, maximum output 50 kV_{rms}, 5 kVA) was used as a high-voltage source. The applied voltage, V_s , and charging voltage, V_Q , across a series capacitor (0.04 μF) were measured using a digital phosphor oscilloscope (MDO3012, Tektronix, Beaverton, OR, USA) via high-voltage probes. The discharge current, i_D , was measured using a Rogowski coil (110, Pearson, CA, USA). The DBD power in the reactor was calculated using the V - Q Lissajous figure technique [113, 117]. Figures 4.6a and 4.6b show the electric field distribution and potential field distribution simulated using COMSOL Multiphysics (ver. 5.4), electrostatic physics mode, for DBD electrode configuration, the high electric field region is occurred in 3 mm-gap.

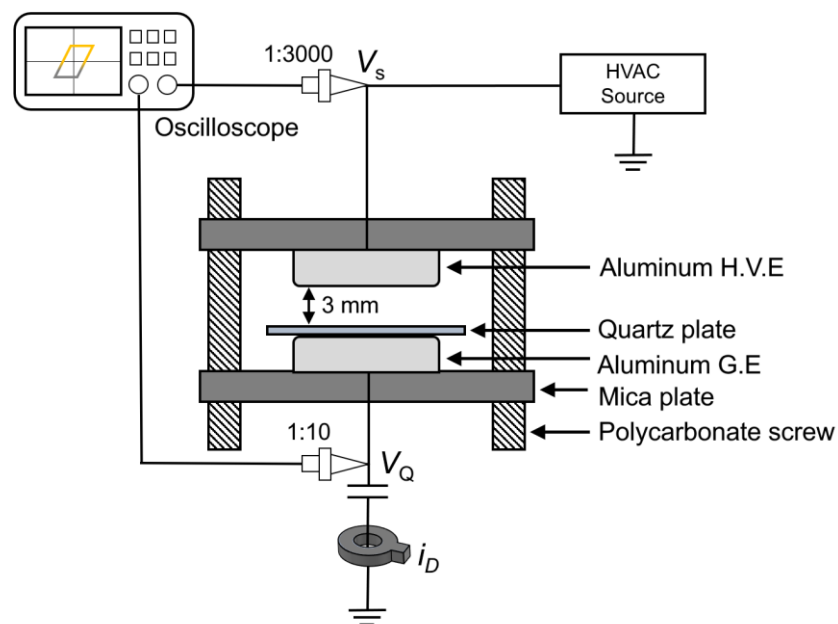


Figure 4.5. Schematic of DBD reactor and electrode configuration [105].

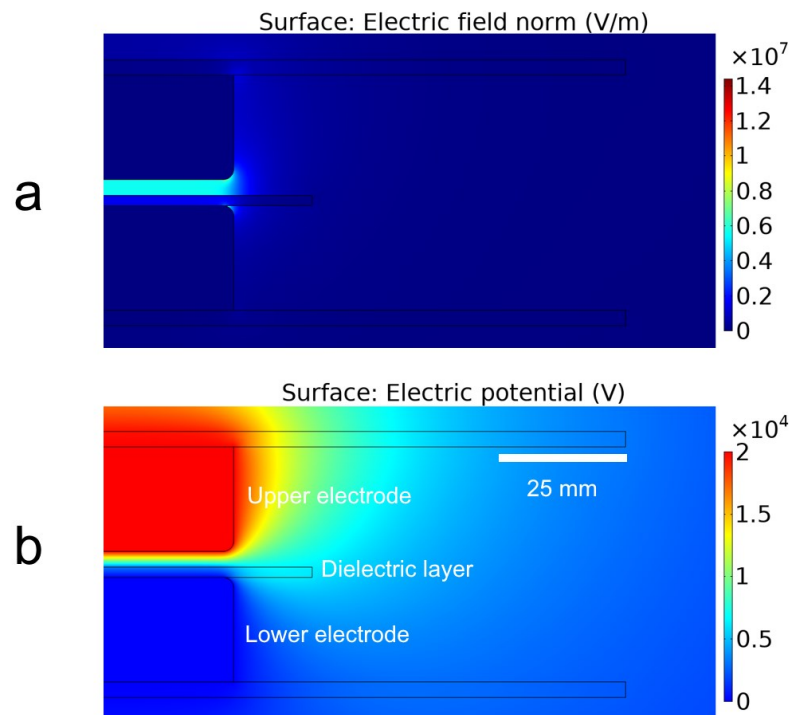


Figure 4.6. Electrode configuration simulation (a) Electric field distribution, and (b) Electric potential. The high electric field region is occurred in 3 mm-gap.

4.2.2 Test gas

CF_4 concentration was varied between 0 and 20,000 ppm (0, 10, 100, 300, 500, 1,000, 2,000, 4,000, 10,000, and 20,000 ppm). As previously mentioned, the target CF_4 concentration for GIS diagnosis is approximately 30 ppm (see Chapter 2).

The DBD-induced CF_4 conversion into CO and CO_2 may be performed with or without artificial O_2 gas addition to the GIS sample gas. Without additional O_2 , CO and CO_2 might be generated by the reaction between CF_4 and O_2 , or H_2O , which could exist in the GIS as a small amount of contamination. However, this cannot control the amount of O_2 involved in the reaction as desired. Accordingly, we decided to artificially add 1% or 10% concentration O_2 as an additive. The conversion ratio into CO and CO_2 is also expected to improve with higher concentrations of O_2 additive.

4.2.3 Analysis of generated CO and CO₂

The DBD-treated gas was analyzed by FT-IR (IRSpirit-T, Shimadzu, Kyoto, Japan) and an electrochemical CO gas sensor. For FT-IR analysis, the infrared spectra of tested gases were measured in the range of 400–4,000 cm⁻¹. Several peaks from SF₆, CF₄, CO, CO₂, and others were detected. Some of the peaks were overlapped [118]. Based on the FT-IR spectra, the calibration curves were obtained for quantifying each gas concentration. Details of how the calibration curves were generated can be found in the gas analysis preparation section. Briefly, in CO₂, FT-IR spectra of serial dilutions of CO₂ in SF₆ were subtracted from those of pure SF₆.

The electrochemical CO sensor (model TGS5042) and its evaluation module (model EM5042A) were purchased from Figaro Engineering (Osaka, Japan). This sensor can detect CO in the range of 0–10,000 ppm. The TGS5042 is a battery operable electrochemical sensor, the electrolyte of TGS5042 is a low concentration of mixed/prepared alkaline electrolyte consisting of KOH, KHCO₃, and K₂CO₃ [119, 120].

The sensor was placed in the sensor chamber, to which the DBD-treated test gas was introduced for CO detection. According to the CO sensor datasheet, the sensor shows cross-sensitivity to other gases. Among the gas, an effect of SO₂ was concerned, which is generated by discharge plasma to a mixture of SF₆ and O₂ [110, 114]. Before performing the test gas sensing, the sensor response was calibrated for CO detection in SF₆ with SO₂. Details of the CO sensor calibration can be found in the gas analysis preparation section.

4.2.4 Experimental procedure

Figure 4.7 shows a schematic diagram of the experimental setup. The flow rate of gases (SF₆, CF₄, and O₂) was controlled with a mass flow control (MFC) unit (STEC, MU-3406, Horiba, Kyoto, Japan). The purity of SF₆ gas used in the experiments was 99.99%. First, the mixture of CF₄/O₂/SF₆ gas was introduced into the DBD treatment chamber closed for the DBD treatment. After the DBD treatment, the processed gas was introduced into the sensor chamber, where the electrochemical CO sensor was placed. Also, the gas was introduced to the FT-IR cell. The gas flow for the analysis was controlled by a pump, 7L/min (DAP-6D, ULVAC, Methuen, MA, USA) placed downstream of the DBD chamber. All experiments were carried out at RT (approximately 20°C). Detail of the experimental procedure is as follows:

(1) The aluminum electrodes and quartz were cleaned using purified water. Then, after 24 h to allow the water to evaporate, the reactor was set in the gas treatment chamber.

(2) After setting up the apparatus, the DBD chamber was evacuated to less than 10 Pa. This pressure was maintained for at least 2 h to remove impurities and residual gases in the chamber.

(3) The gas mixture, with varied CF₄ concentration diluted in SF₆ with O₂ additive, was introduced into the gas treatment chamber at a pressure of 0.1 MPa.

(4) The test gas was exposed to DBD at an applied voltage of 22 kV_{rms} for 30 min. In the meantime, the *V-Q* Lissajous figure was obtained to quantify the average DBD power. After the DBD process was completed, the DBD-treated gas was introduced into the sensor chamber and FT-IR cell for gas analysis.

(5) After each experiment, the gas treatment chamber was evacuated for 2 h to remove residual gases at the pressure of less than 10 Pa as in step (2), then filled with N₂ at atmospheric pressure until the following experiment.

4.3 Gas analysis preparation

4.3.1 Determination of CO₂ concentration

Figure 4.8 shows the IR absorption bands of 100% SF₆, 100% CF₄, and 500-ppm CO₂ in N₂. It should be noted that the main CO₂ absorption band is located in the spectral range of 2280–2385 cm⁻¹, which is overlapped with that of SF₆. Therefore, the spectra curve subtraction technique was employed as follows [121- 123]. The concentration of DBD-generated CO₂ was calculated by subtracting the integral value of the absorbance in the range of 2280–2385 cm⁻¹ of 100% SF₆ from the measured integral value of the absorbance in 2280–2385 cm⁻¹ of CO₂. The integral value of the absorbance of CO₂ (A_{CO_2}), can be estimated by the following equation:

$$A_{CO_2} = A_{SF_6+CO_2} - A_{SF_6} \quad (4.1)$$

where $A_{SF_6+CO_2}$ represents the integral value of the measured absorbance, which is obtained from the DBD-treated CF₄/O₂/SF₆ gas mixture. A_{SF_6} is the integrated value of the absorbance in the range of 2280–2385 cm⁻¹ of 100% SF₆. Figure 4.9 shows the relationship of the absorbance spectra. The CF₄ absorption is negligibly small when the mixed ratio was less than 1%. O₂ has no overlapped absorption band in this wavenumber

range [124]. A_{SF_6} , which represents the SF_6 concentration after DBD application, can be obtained by integrating the IR absorption curve for DBD-treated O_2/SF_6 gas mixture without CO_2 generation (Figure 4.9, middle curve). The IR absorption curve obtained by subtracting these two curves (Figure 4.9, top curve), which represents that of CO_2 generated by DBD-induced CF_4 conversion, is integrated to obtain A_{CO_2} . Other gases, such as CO , SO_2 , H_2O , had no effect for analysis significantly.

This procedure enables the quantification of CO_2 concentration generated by DBD treatment of $CF_4/O_2/SF_6/$ gas mixture. The validation of the procedure was confirmed by using SF_6 gas mixed with known concentrations of CO_2 . The calibration curve is depicted in Figure 4.10, showing that A_{CO_2} linearly increases with CO_2 concentration in the concentration range between 0 to 700 ppm. A_{CO_2} is almost identical to the integral value of the absorbance of CO_2 in N_2 . This implies the subtraction method determines the concentration of CO_2 in SF_6 correctly.

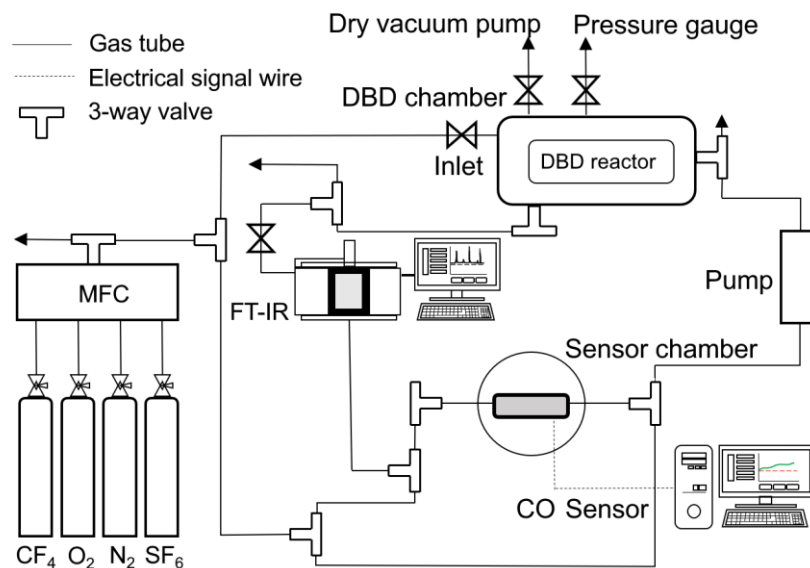


Figure 4.7. Schematic diagram of the experimental setup [105].

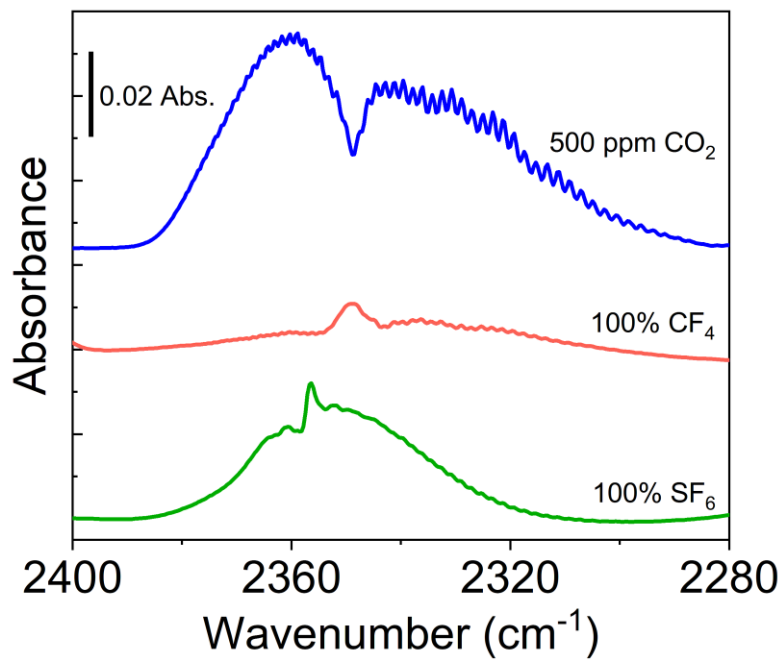


Figure 4.8. IR absorption bands of CF₄, SF₆, and CO₂.

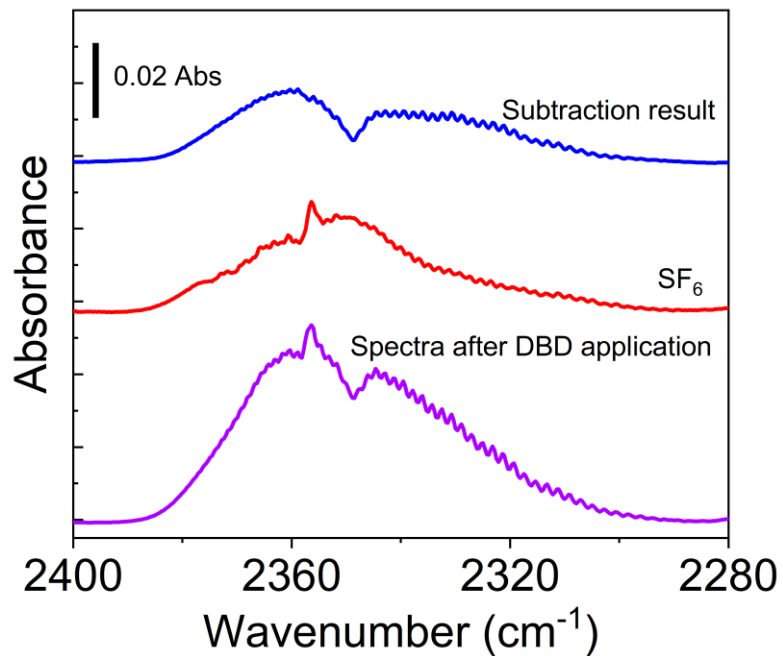


Figure 4.9. Typical IR absorption bands of DBD-treated CF₄/O₂/SF₆ gas mixture (bottom), pure SF₆ (middle), and the subtraction (top).

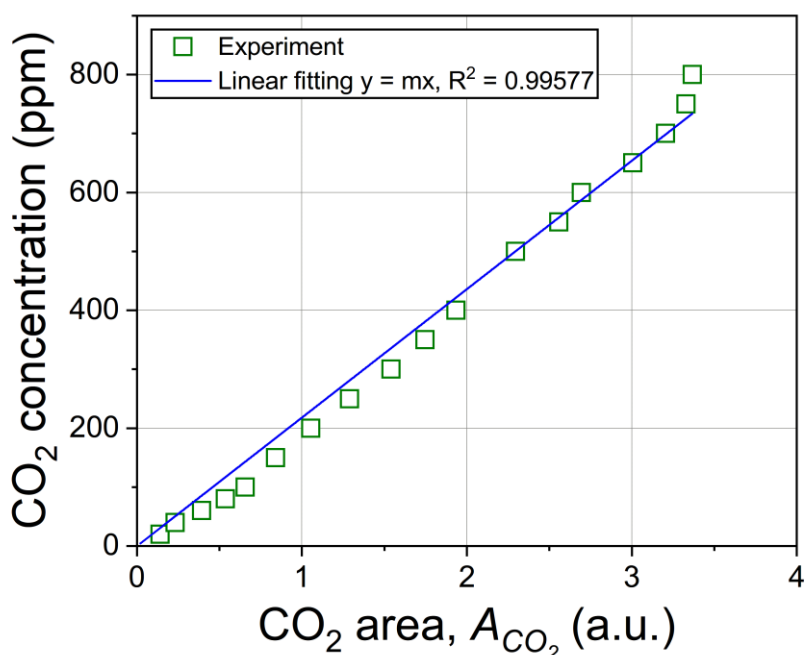


Figure 4.10. Relationship between the A_{CO_2} and CO₂ concentration mixed in SF₆. the IR absorbance area of CO₂.

4.3.2 Determination of CO concentration

Figure 4.11 shows the IR absorption bands of a gas mixture of 500-ppm CO and 1,000-ppm CF₄ diluted with SF₆ (upper curve). The main CO absorption band is located in the spectral range of 2050–2225 cm⁻¹, which is partially overlapped with the absorption bands of CF₄ and SF₆ in the range of 2150–2250 cm⁻¹ (lower curve). CO concentration can be quantified by integrating the absorption curve in the range of 2048–2125 cm⁻¹, where CF₄ and SF₆ absorptions are not overlapped. The validation of the procedure was confirmed by using SF₆ gas mixed with known concentrations of CO. The calibration curve is depicted in Figure. 4.12, showing that the CO absorption area linearly increases with CO concentration in the range between 0 and 800 ppm. This enables quantification of CO concentration generated by DBD treatment of the CF₄/O₂/SF₆ gas mixture. Other gases, such as CO, SO₂, H₂O, had no effect for analysis significantly.

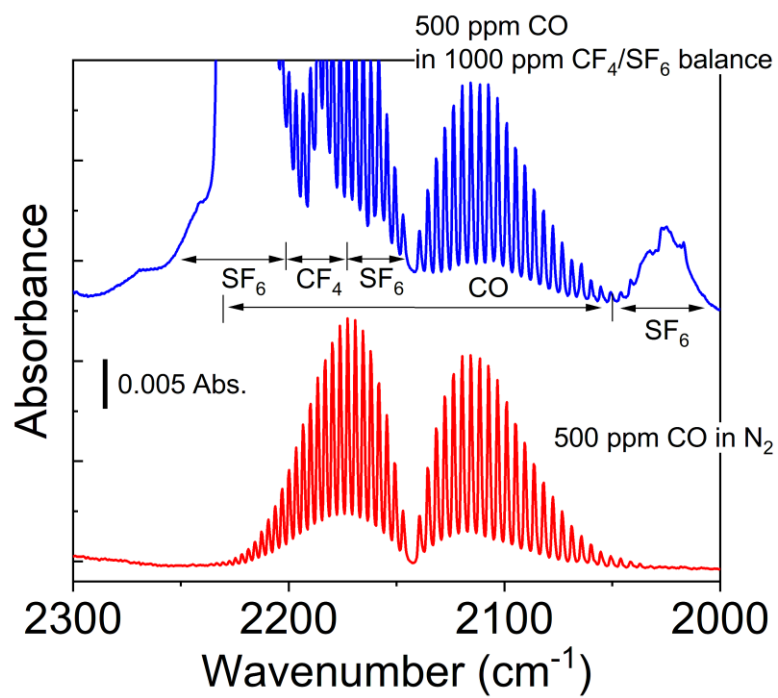


Figure 4.11. IR absorption bands of CO, CF₄, and SF₆ [105].

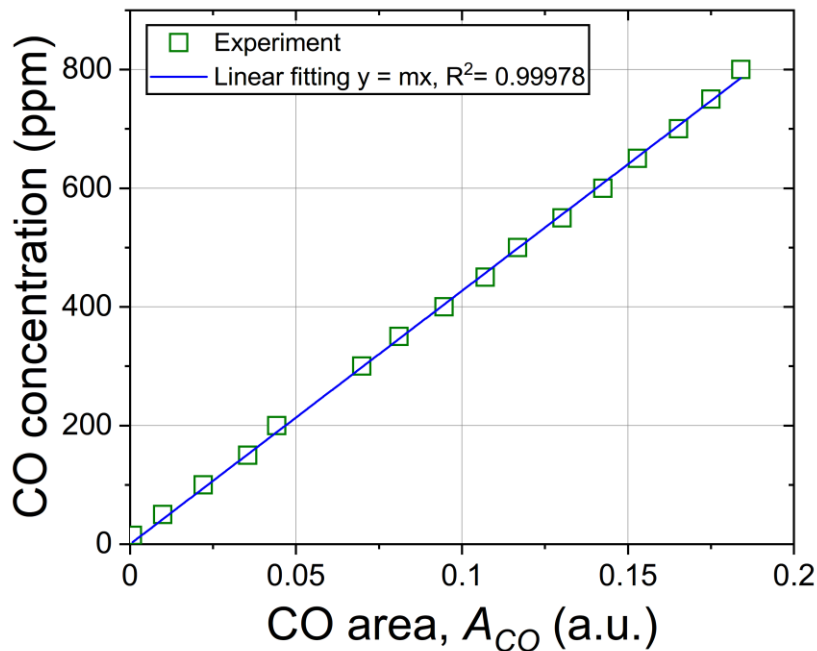


Figure 4.12. Relationship between the A_{CO} and CO concentration mixed in SF₆. of 2048–2125 cm⁻¹ [105].

4.3.3 CO sensor performance under SF₆ background gas and SO₂ influence

Figure 4.13 shows the photo of the CO sensor and its evaluation module used in this study. The evaluation module converts sensor output current to voltage output and it is designed the electrical noise reduction for stable operation. The cost of the sensor and the module are 9900 yen and 32000 yen, respectively. Figure 4.14a shows the schematic diagrams of the CO sensor system. The CO sensor was installed in the sensor chamber, 160 cm³ in the volume. Figure 4.14b shows the steps how to obtain the CO concentrations. When CO sensor response to CO gas generated after DBD treatment. Evaluation module, drive-by 5 VDC source (PA36-1.2B, TEXIO), sends the voltage signals to the data logger. Then data logger (LR8431, HIOKI) sends signals to the PC via a USB port interface. They are monitoring the real-time response by Logger Utility software on PC and storing data in Excel files. Finally, calculate the CO response in ppm using the master calibration curve obtained from the experiment.

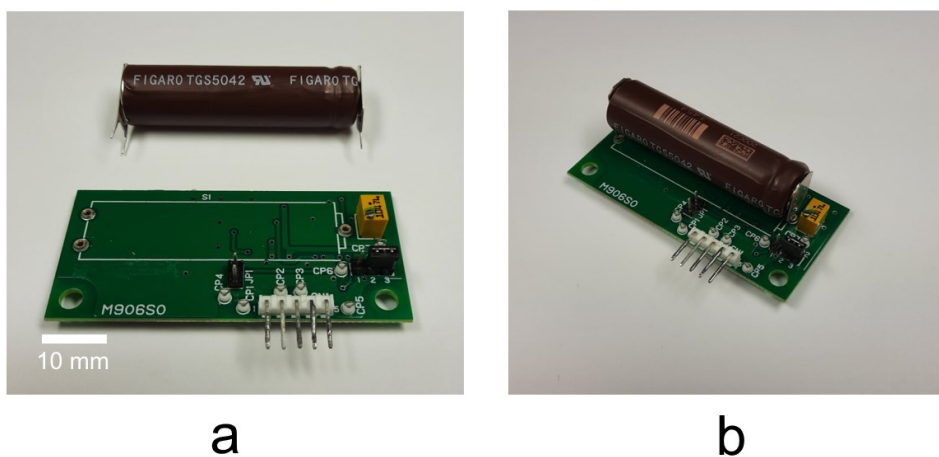
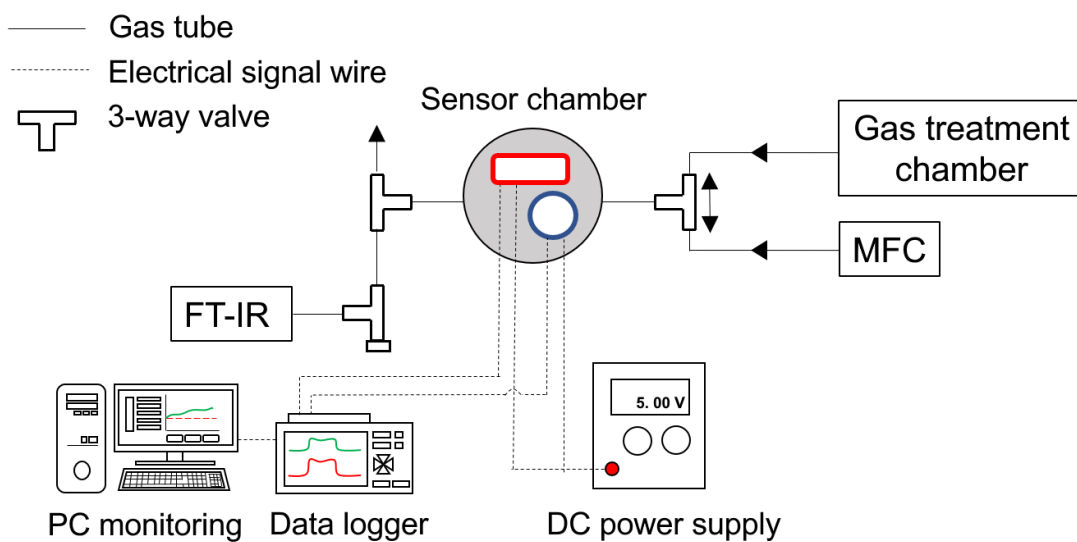
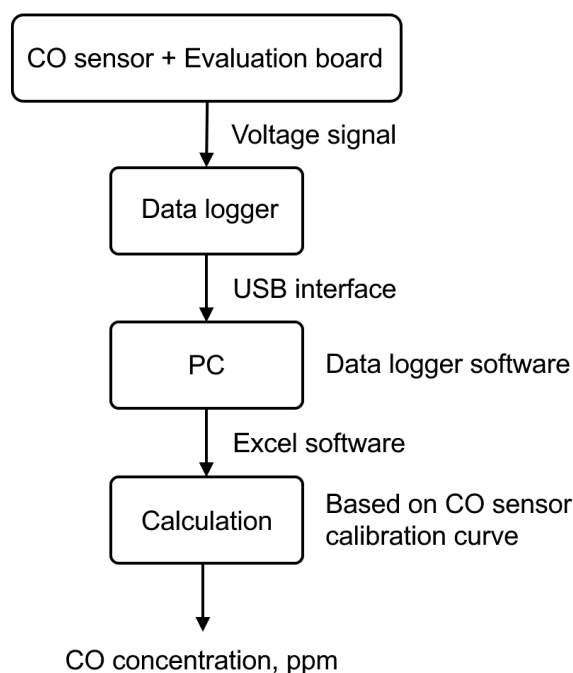


Figure 4.13. The electrochemical CO sensor (a) model TGS5042 and its evaluation module model EM5042A, and (b) their assembly.



a



b

Figure 4.14. CO sensor (a) CO sensor system (b) calculation steps

Figure 4.15 shows the calibration curves of the CO gas sensor obtained under different background gas conditions. According to the datasheet supplied by the sensor manufacturer, the electrochemical gas sensor exhibits a cross-sensitivity to SO_2 , which is generated by the DBD treatment of $\text{CF}_4/\text{O}_2/\text{SF}_6/$ gas mixture. 100-ppm SO_2 gas was detected by a gas detection tube (5DH, Gastec, Warminster, PA, USA) along with the CO_2 and CO generation shown in Figures 4.23 and 4.24, respectively. I examined the CO gas sensor for known concentrations of CO mixed with 100-ppm SO_2 under the background gases, SF_6 or N_2 . When N_2 was used as the background gas, the CO sensor reading corresponded to the actual CO concentration adjusted by MFC. If 100-ppm SO_2 was mixed with the background N_2 , the CO sensor reading was slightly higher than the actual CO concentration. However, it is worth noting that the CO sensor reading was lower than the actual CO concentration with SF_6 as the background gas. It might be possible that SF_6 with a strong electron affinity could act as a scavenger of electrons [45]. SF_6 may cause decreasing the electron flowing the circuit, especially for the surface of the sensor. The calibration curve obtained with 100-ppm SO_2 with SF_6 background was

used to get the data shown in the results section.

Figure 4.16 shows an example of the temporal response of the CO sensor. After a steady baseline was attained by the gas before DBD application, the DBD-exposed gas was introduced. Sequences were included the tested gas for time t_1 , exposing the decomposition gas for time t_2 , and backed to tested gas again for time t_3 . The sensing response was shown as ppm response against CO generated.

4.3.4 DBD plasma characterization

Figure 4.17 shows photographs of DBD plasma generated in the DBD reactor filled with pure SF₆. The number of discharge filaments and the emission light increased with the applied voltages.

Figure 4.18 shows the voltage waveforms to the reactor and the discharge current when the microdischarges occurred with 25 kV_{rms}. The current pulses of the microdischarge are observed only in the pulse rising phase [110].

Power consumed by DBD is calculated by drawing Lissajous Figure [110, 117]. I studied DBD power because I need to know the power consumption of DBD reactor when compared to another type of reactor, such as a cylindrical reactor and another reason is I need to confirm the result of DBD power when the background gases were changed. Figure 4.19a shows a comparison of the V - Q Lissajous diagram at the applied voltages of 21 and 25 kV_{rms}. Figure 4.19b shows the charge-voltage slope m_1 and m_2 on the obtained Lissajous Figure [117]. This illustrates the two duty cycles when discharge off and discharge occurring. The slope m_1 of the Lissajous Figure represents the capacitance of the barrier discharge arrangement, $C_{BD} = m_1$, when the discharge off. The slope m_2 represents the capacitance of the dielectric barrier, $C_d = m_2$, when discharge occurs. With these values, the capacitance of the discharge gap, C_g , can be calculated using

$$C_{BD} = \frac{C_g C_d}{C_g + C_d}. \quad (4.2)$$

The electrical power dissipated in the DBD plasma was calculated using the Lissajous Figure method and summarized in Figure 4.20. The plasma power increased almost linearly with applied voltage and was not significantly influenced by the gas mixture components.

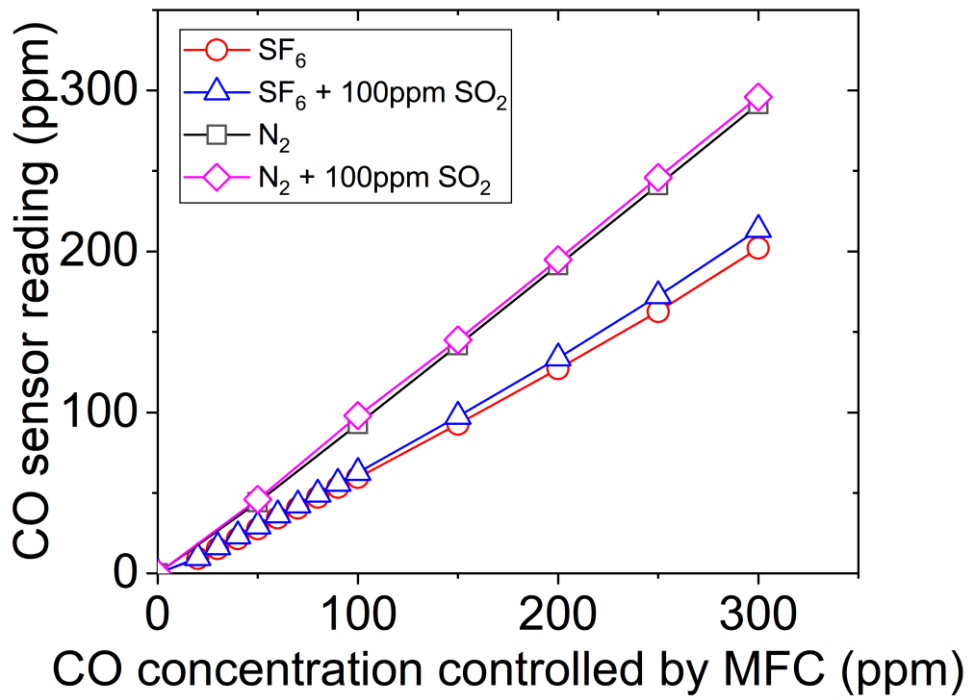


Figure 4.15. Calibration curves of the CO gas sensor under different background gas conditions. Legends indicate the background gases.

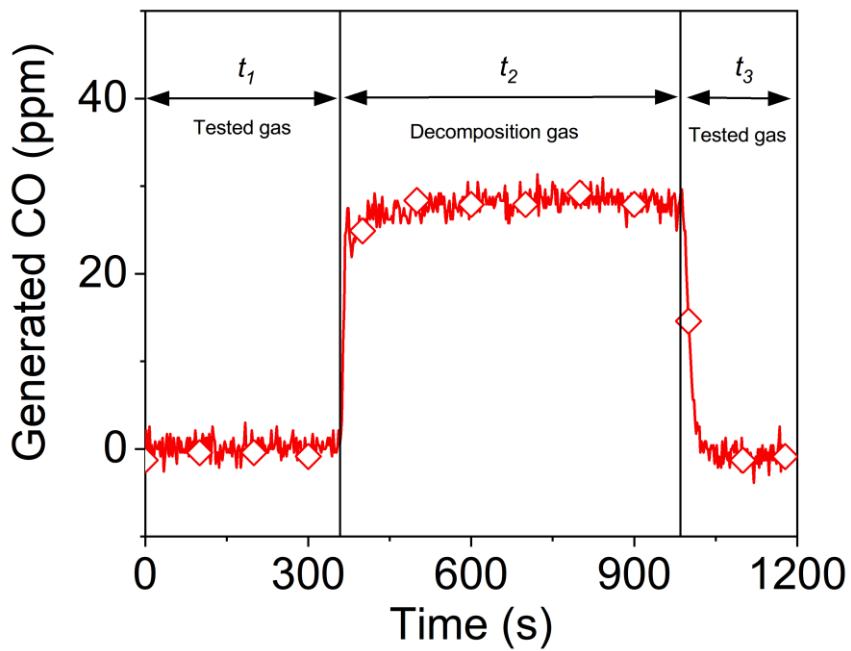


Figure 4.16. Typical response of CO sensor against CO in decomposition gas.

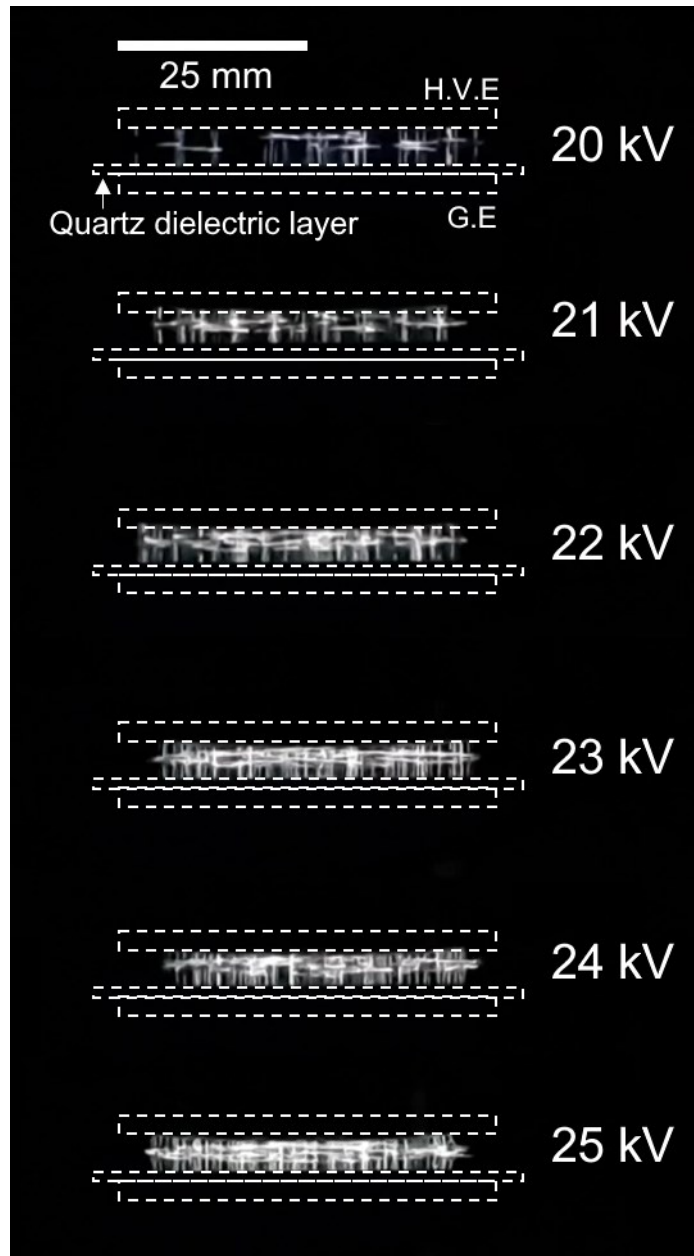


Figure 4.17. Typical DBD generated by the DBD reactor with various applied voltages (30 frames per second). Discharge filament with increasing applied voltage from 20 to 25 kV_{rms}. All photos were taken by digital camera with shutter speed 1/20 sec and ISO-400.

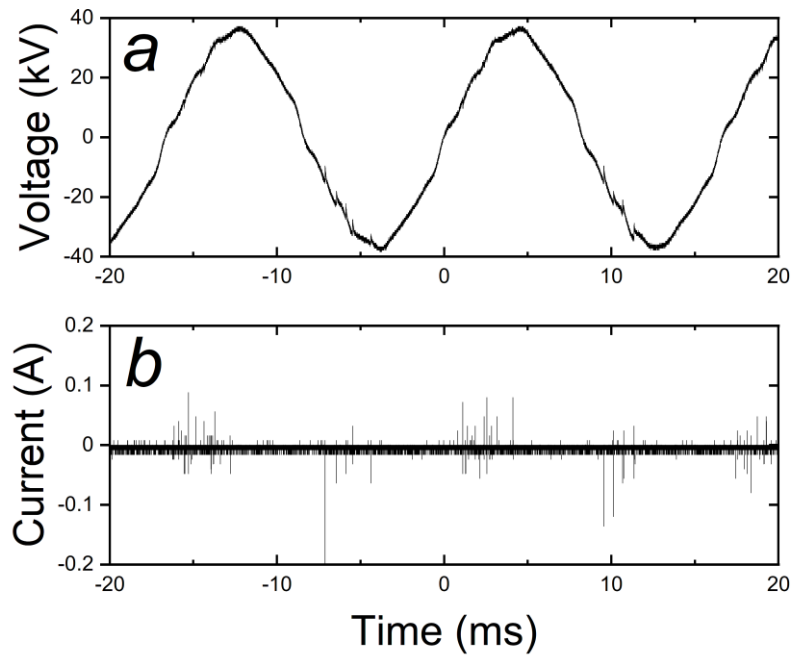


Figure 4.18. Typical waveform under DBD. (a) Applied voltage, and (b) current.

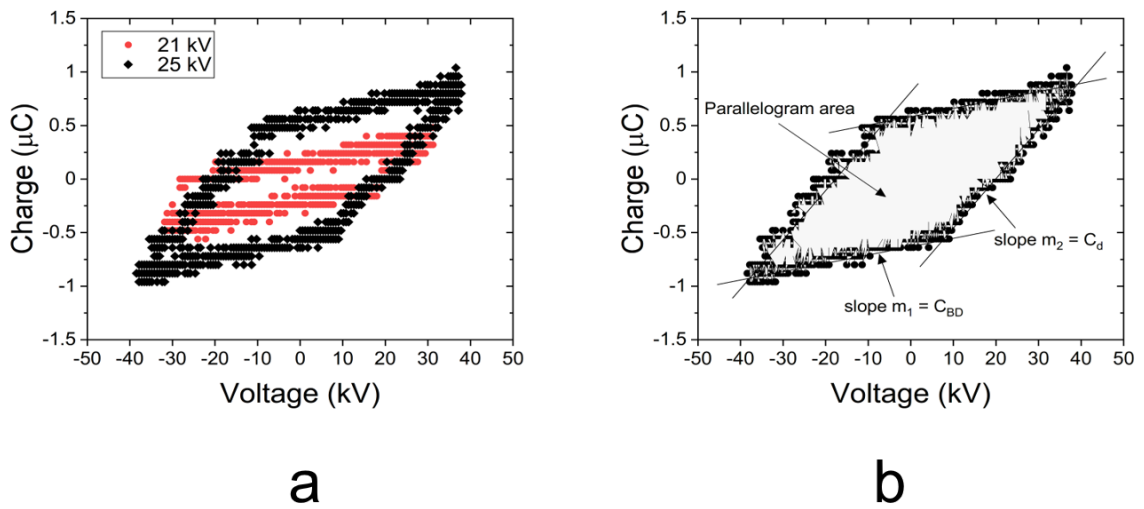


Figure 4.19. Typical V - Q Lissajous of DBD. (a) Comparison typical V - Q Lissajous of DBD between 21 and 25 kV applied voltage and (b) V - Q Lissajous with capacitance slope at 25 kV_{rms}.

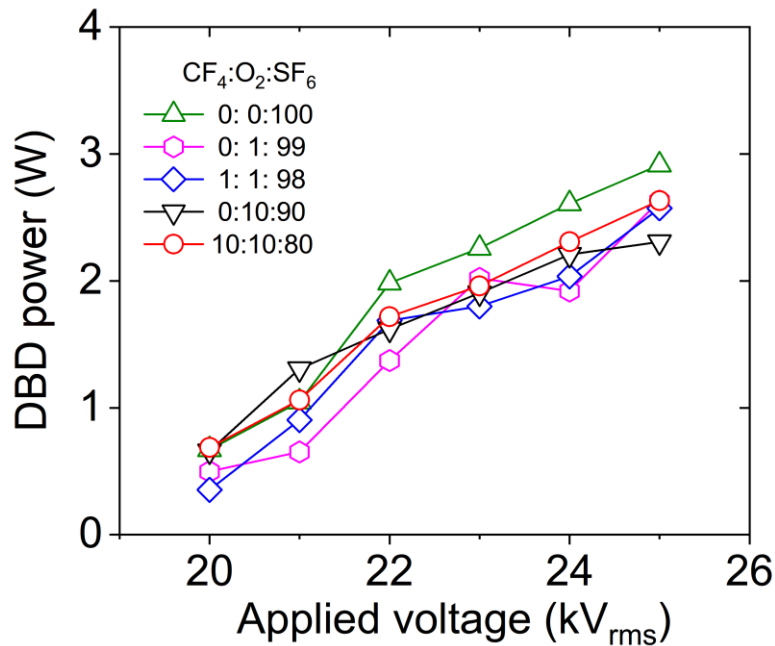


Figure 4.20. Plot of DBD plasma power as a function of the applied voltage with various gas contents. Legends indicate the ratio of the gas mixture.

4.4 Results

4.4.1 DBD plasma characteristics

Typical images of the microdischarges of DBD in the $\text{CF}_4/\text{O}_2/\text{SF}_6$ gas mixture are shown in Figure 4.21 (shutter speed of camera 1/20 sec). There were many bright microdischarge filaments generated between the electrodes. Detailed DBD characteristics can be found in the Appendix. The discharge power characteristics (averaged over 30 min) are plotted in Figure 4.22. It was found that the power was almost independent of O_2 and CF_4 concentrations and was in the range of 1.5–2.0 W.

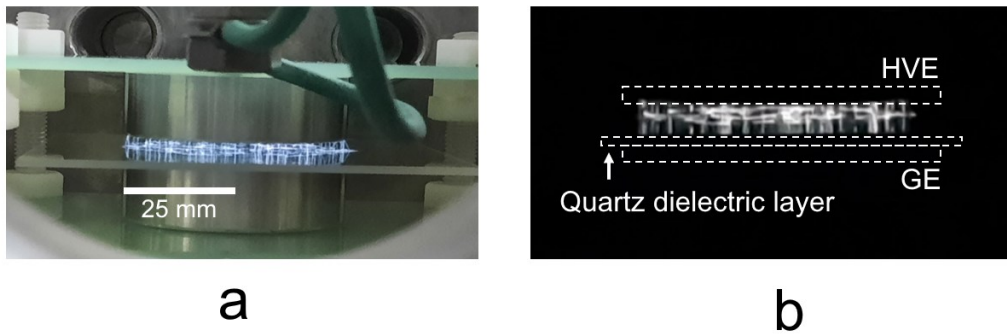


Figure 4.21. Typical images of micro discharge filament between electrodes. (a) The backlight on, and (b) the backlight off. At 22 kV_{rms} applied voltage. All photos were taken by digital camera with shutter speed 1/20 sec and ISO-400.

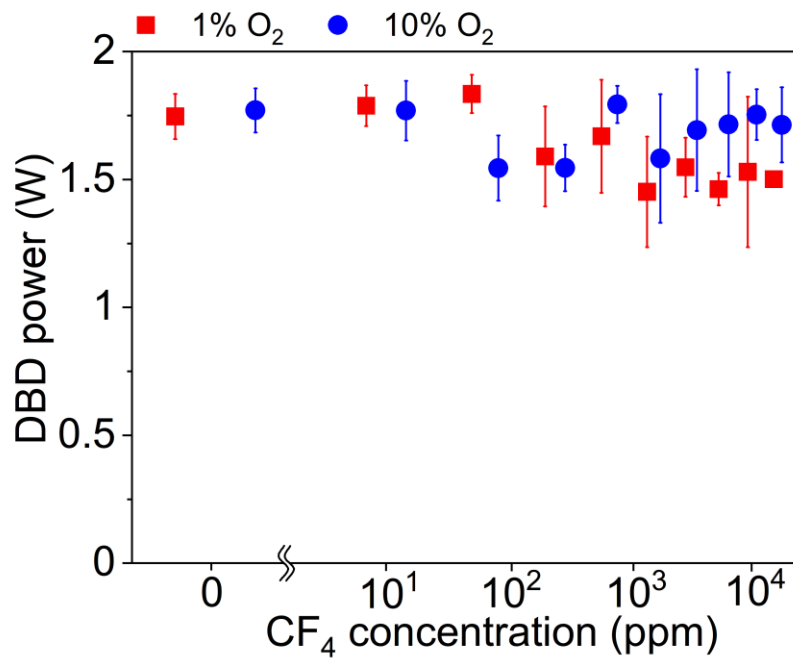


Figure 4.22. 30-min-averaged DBD power for various CF₄ concentrations and O₂ content at 22 kV_{rms} [105].

4.4.2 Generation of CO₂ and CO by DBD

The FT-IR analysis results of CO₂ and CO gas generated by DBD treatment of CF₄/O₂/SF₆ gas mixture with various CF₄ concentrations are shown in Figures 4.23 and 4.24, respectively. The conversion rate was defined as (CO₂ or CO concentration after DBD) / (adjusted CF₄ concentration).

In 1% O₂ addition, CO₂ generation was detected only for CF₄ concentrations higher than 100 ppm. The CO₂ concentration gradually increased with the CF₄ concentration, then decreased after peaking at a CF₄ concentration of 1,000 ppm, as shown in Figure 4.23a. The maximum conversion rate was 1.4%, which occurred at the CF₄ concentration of 1,000 ppm. When the O₂ addition increased from 1% to 10%, the CF₄ to CO₂ conversion rate was enhanced for the tested entire CF₄ concentration range, as shown in Figure 4.23b. The peak values of CO₂ concentration and CO₂ conversion rate were increased two- and seven-fold, respectively. As depicted in Figure 4.24, the CF₄ concentration dependence on the CO concentration was almost similar to the CO₂ concentration. However, it should be noted that the CF₄ to CO conversion rate was not enhanced when the O₂ addition increased from 1% to 10%. This finding is discussed in the next section.

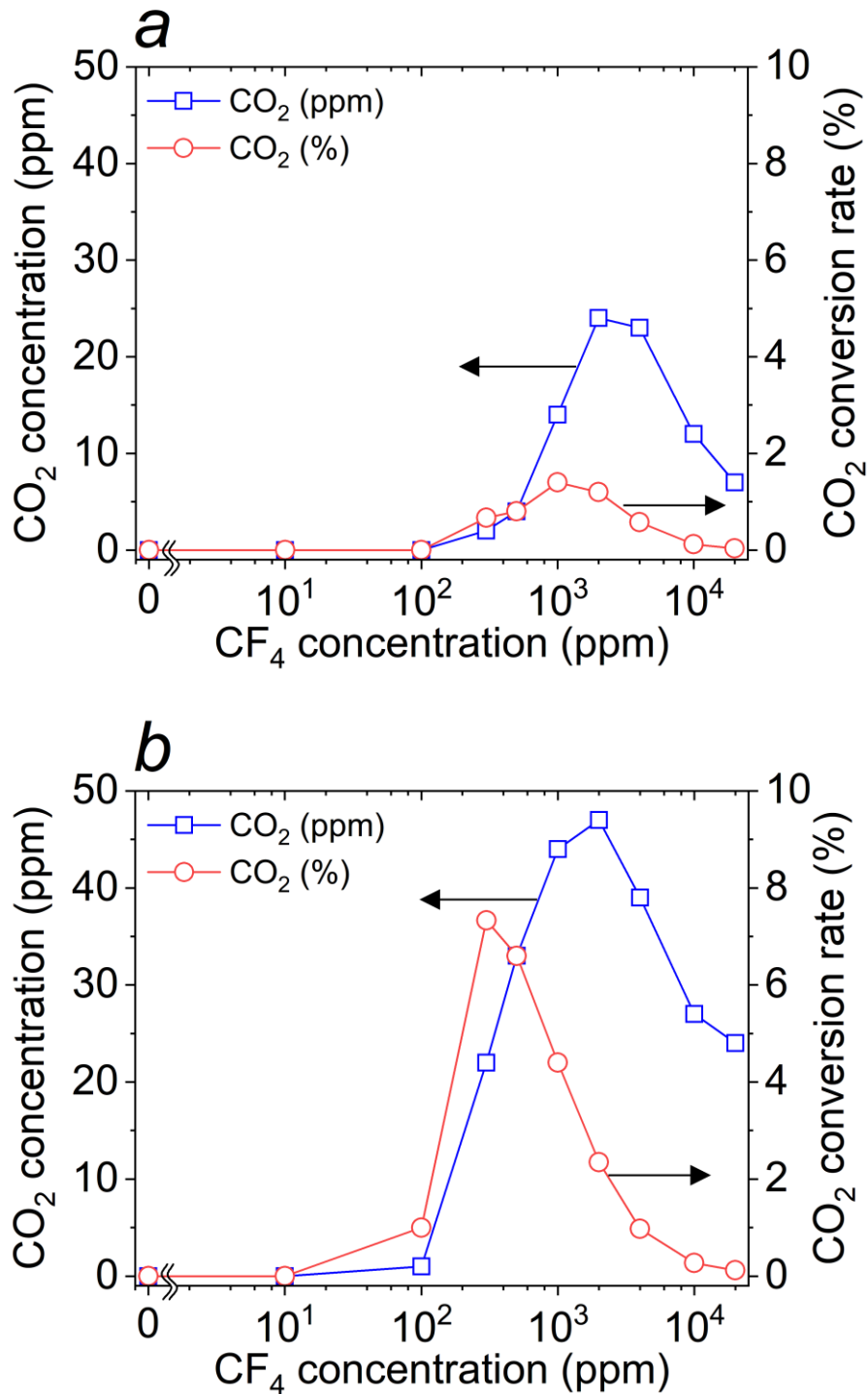


Figure 4.23. CO_2 concentration and CF_4 conversion rate into CO_2 : (a) 1% and (b) 10% O_2 content addition. The applied voltage was $22 \text{ kV}_{\text{rms}}$, and the treatment time was 30 min [105].

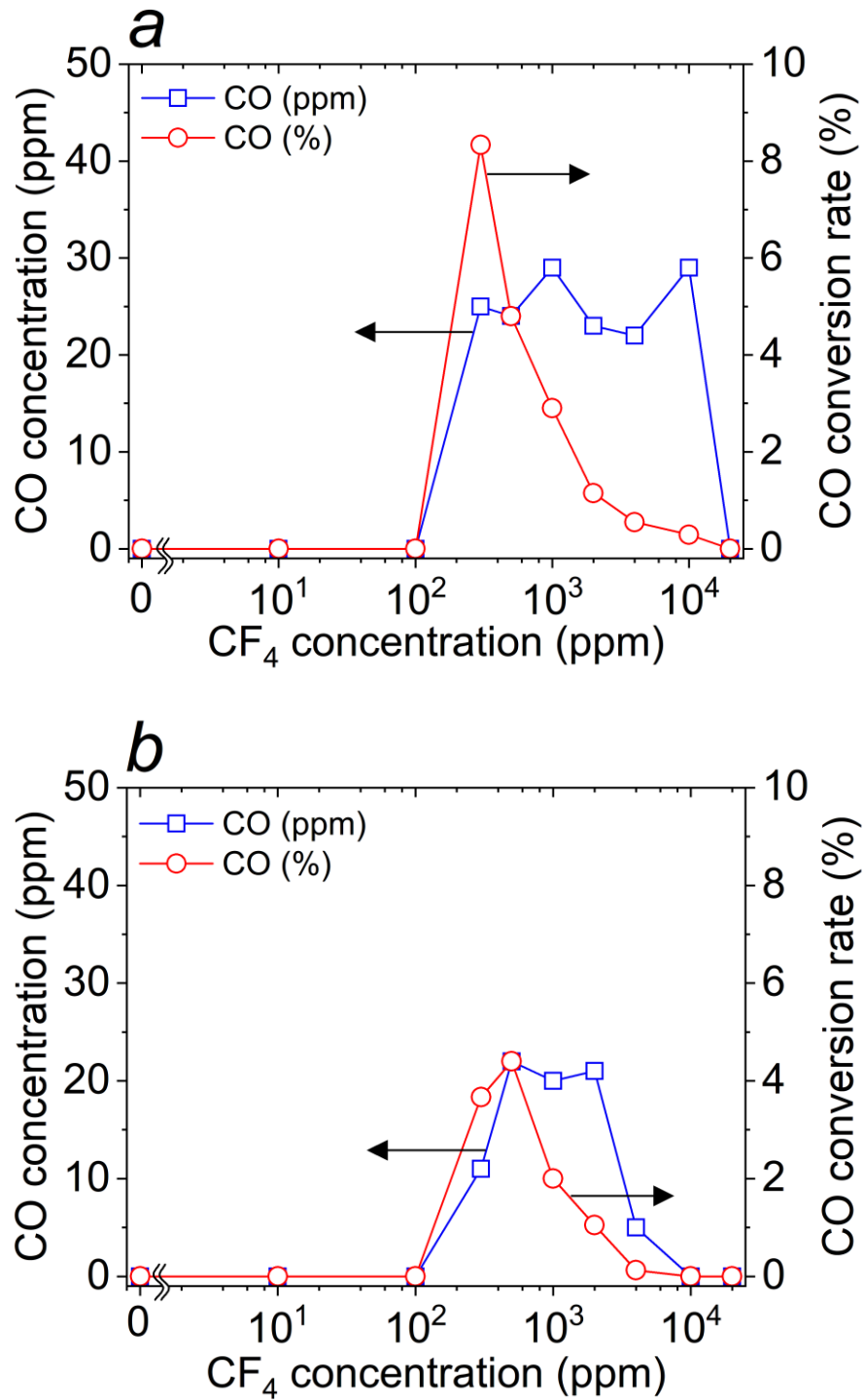


Figure 4.24. CO concentration and CF_4 conversion rate into CO: (a) 1% and (b) 10% O_2 content addition. The applied voltage was $22 \text{ kV}_{\text{rms}}$, and the treatment time was 30 min [105].

4.4.3 Electrochemical CO sensor performance

The FT-IR results shown in Figures 4.23 and 4.24 suggest that the possibility of indirect CF₄ detection using the proposed DBD-induced conversion to CO or CO₂. The CF₄ detection limit is approximately 100 ppm, which is very close to the target concentration of 30 ppm for GIS diagnosis. These results encouraged me to attempt CO detection using a commercially available CO gas sensor.

I selected CO as the target gas to be detected with a gas sensor, not CO₂. There are commercially available sensitive CO gas sensors that detect 10-ppm, whereas such a CO₂ gas sensor is not. We can find cheap but sensitive CO sensors. CO₂ and CO gas sensor are available in the market shown in Figure 4.25 and 4.26 [125], respectively. Moreover, Table 4.1 shows the recent CO sensors which are available in the market (The year 2021). The cost shows around 100-200 USD/Pc.

As mentioned before, DBD treatment of CF₄/O₂/SF₆ gas mixture produces SO₂, to which electrochemical CO gas sensors are known to have a cross-sensitivity. Therefore, the CO sensor was calibrated in advance with SO₂ as a coexisting decomposition gas. Figure 4.27 compares the CO gas concentrations obtained by FT-IR and the CO gas sensor with 10% O₂ addition. The CO gas concentrations obtained by the two different methods are in good agreement for the tested entire CF₄ concentration range. However, upon closer examination, it is revealed that the CO gas sensor tends to show higher CO concentrations than FT-IR analysis in some cases. This may be attributed to unknown decomposition gases other than SO₂, to which the CO gas sensor might show cross-sensitivity.

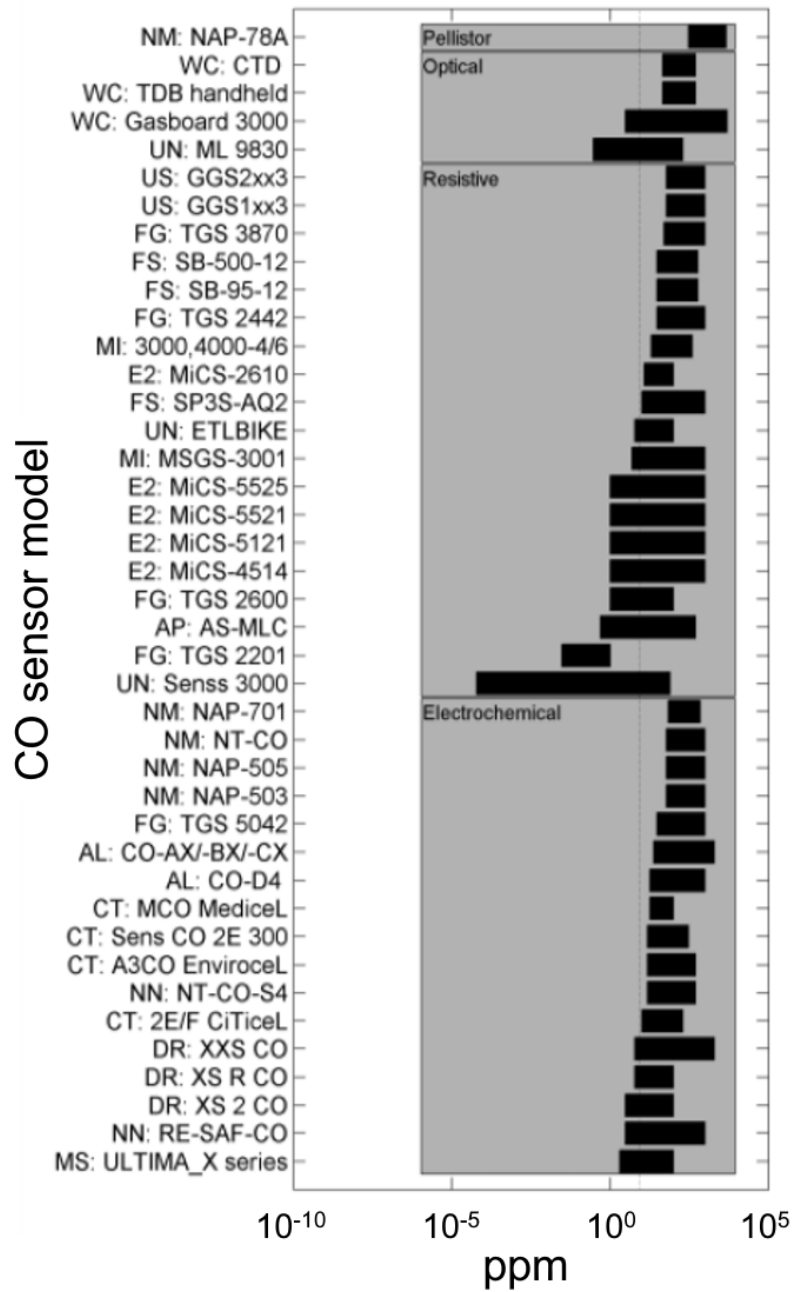


Figure 4.25. CO gas sensors in the market [125]

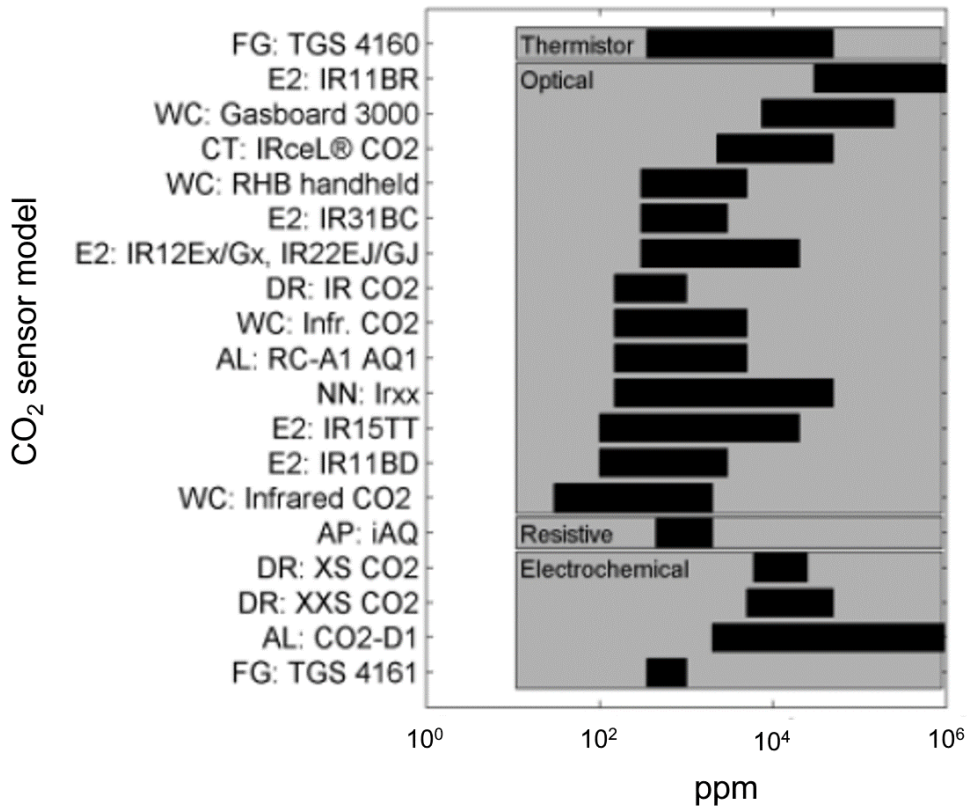


Figure 4.26. CO₂ gas sensors in the market [125]

Table 4.1. CO sensor, detection range, and cost

Manufacturer	Sensor model	Detection range (ppm)	Technology	Cost (USD)	Website
Figaro	TGS5042-A00	0 - 10,000	Electrochemical	90	https://www.figaro.co.jp/
Figaro	FECS40-1000	0 - 1,000	Electrochemical	122	https://www.figaro.co.jp/
Alphasense	CO-AF	0 - 5000	Electrochemical	199	https://www.alphasense.com/
Microsens	MGSM	5 - 1000	Resistive	Price quotes	http://microsens.ch/products/
Unitec	SENS-IT	0.1 - 80	Electrochemical	Price quotes	http://www.unitec-srl.com/
Nervitech	NT-CO-SLI1000	0 - 1000	Electrochemical	Price quotes	https://www.nervitech.com/

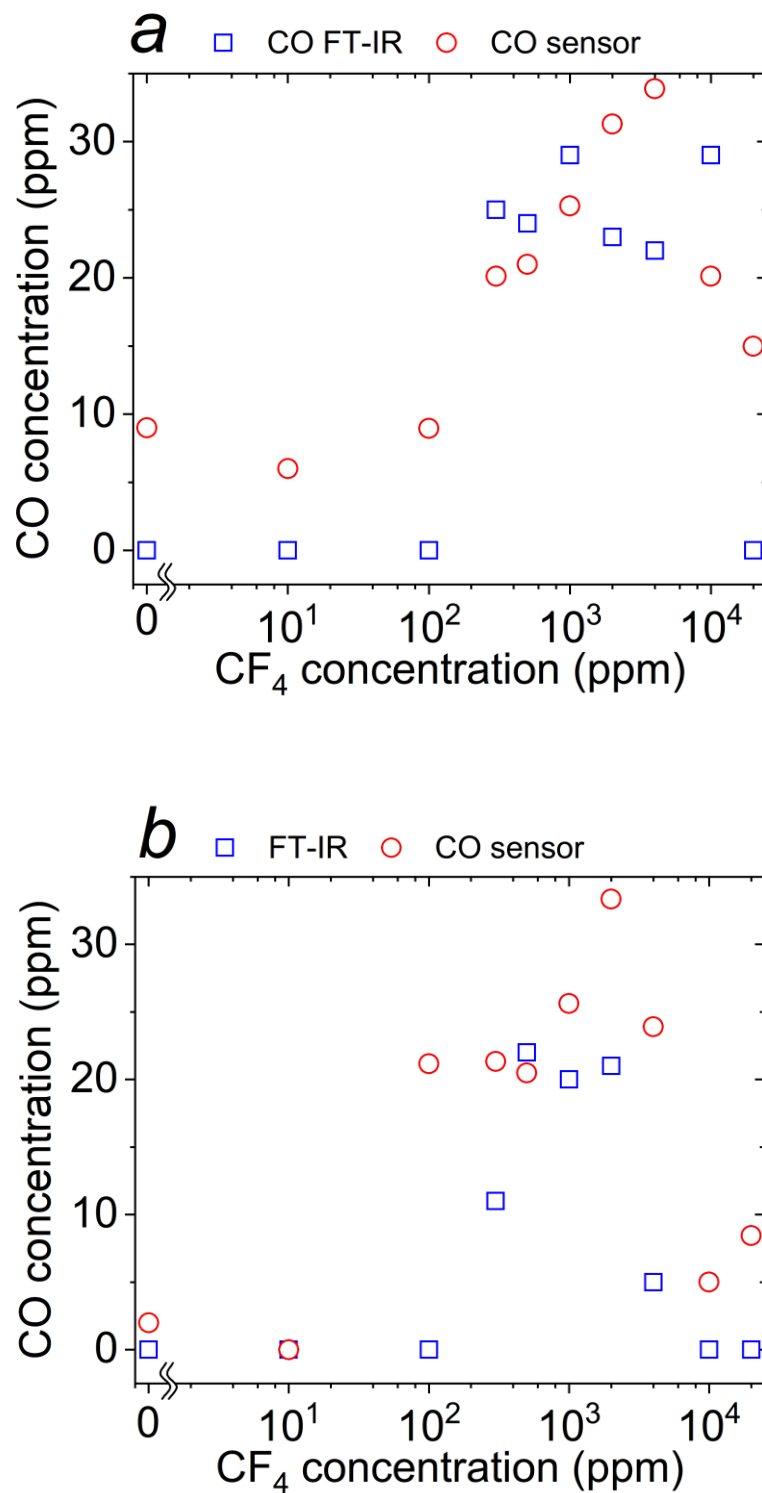


Figure 4.27. Comparison of CO concentrations obtained by FT-IR and the CO gas sensor: (a) 1% and (b) 10% O₂ content addition. The applied voltage was 22 kV_{rms}, and the treatment time was 30 min [105].

4.5 Discussion

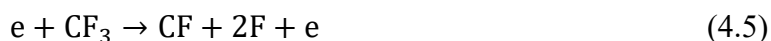
4.5.1 CF₄ to CO and CO₂ conversion rates

As shown in Figures 4.23 and 4.24, the CF₄ to CO and CO₂ conversion rates were less than 10% and depended on CF₄ concentration. To realize secure detection of 30-ppm CF₄, which is the target concentration for GIS diagnosis, a higher conversion rate should be achieved, especially for CF₄ concentrations below 100 ppm. The low conversion rates might be attributed to the relatively small volume of the DBD reactor (approximately 6 cm³) compared to that of the DBD chamber (9,700 cm³) in which it was installed. Because the test gas in the DBD chamber was not circulated using a pump, only a limited portion of the gas was exposed to the DBD plasma. Additionally, this study required a large chamber because the DBD-treated gas was analyzed in series by FT-IR (gas cell volume: 235 cm³) and by the gas sensor installed in a 160 cm³ volume chamber. As demonstrated in Figure 4.25, CF₄ converted to CO gas could be detected by the CO gas sensor, which means that the sample gas volume could be reduced as small as the DBD reactor volume. Higher conversion rates might also be achieved under elevated temperatures [126] or by introducing catalytic reaction steps [127].

4.5.2 CF₄ conversion selectivity

In this study, FT-IR analysis revealed that CO and CO₂ were simultaneously generated via DBD treatment of the CF₄/O₂/SF₆ gas mixture. As illustrated in Figure 4.23 and 4.24, their concentrations were almost identical under the same CF₄ concentration. It might be possible that other gases derived from CF₄, such as COF₂, were also generated and might have contributed to the CO gas sensor response to some extent. Considering that commercial CO gas sensors have higher sensitivity than CO₂ gas sensors, it is preferable that CF₄ is selectively converted to CO rather than CO₂. To date, plasma-induced CF₄ decomposition under the existence of O₂ has been classified into the following two steps [126, 127]. In the first step, a plasma-produced high-energy electron collides with CF₄ molecules to produce CF_x radicals (x = 1, 2, 3), as shown below





In the second step, CF_x radicals react with an O atom, which is also produced from O_2 molecules by the electron impact, to produce CO, CO_2 , and COF_2 . For example,



CO can also be produced from COF_2 and CO_2 by the electron impact as



As shown in Figures 4.23 and 4.24, CO_2 concentration increased with O_2 addition, whereas CO concentration did not. This might imply that electron impact energy was not high enough to convert CO from COF_2 and CO_2 via reactions (4.10) and (4.11). For the DBD reactor employed in this study, a higher electric field is obtained by increasing the voltage applied to the electrode, which is mainly limited by the electrical breakdown of the electrode gap. At the same time, a higher electric field strength could also improve the overall CF_4 decomposition efficiency, as predicted by equations (4.3)–(4.6).

4.5.3 Effect of decomposition gases on the damage of the sensor

At this stage, the most important thing I had to concern about was the generation of corrosive gases such as HF and SO_2 . Especially, HF is a highly acidic chemical that can easily react with the CO sensor's metal pins. It was concerned that the sensor response property might be damaged by the decomposition gas. To confirm this, I tested the CO sensor to expose the decomposition gas many times (for trial and error experiment as

more than ten times, corresponds to 10 hours of the exposure). Then, it was confirmed that after the sensor responded to CO/decomposition gas mixture, then reset the sensor by N₂ exposing. The results showed that the CO sensor could be recovered to initial response. Moreover, the recovery time to the blank value of the sensor response was not affected by repeated use. Therefore, I concluded that this sensor used here works stably under the practical application.

4.5.4 Prospects for on-site GIS diagnosis application

The main purpose of this study was to demonstrate the new technique for GIS diagnosis based on a chemical gas analysis. Using the plasma reactor, the target gas, CF₄ in SF₆ with O₂ additive, was converted into CO and CO₂, which could be securely detected by a commercially available electrochemical gas sensor. Compared to other gas analysis apparatus, such as FT-IR or gas chromatography, the chemical gas sensor is inexpensive, manageable, field-portable, and suitable for on-site GIS diagnosis. However, for DBD generation, the present study employed a high-voltage AC source, which is expensive and not portable due to its large size and heavyweight. To overcome this limitation, a combination of a small-sized high-voltage source and a plasma reactor could be used, which is already being widely employed for portable air cleaners or ozonizers [128].

The portable air cleaner or ozonizers is interesting for our concept because they are small size, portable device and low cost of HV power source. Typically, the reactor of ozonizers designed to surface discharge electrode with high power frequency (approximately 5 kVrms, 15 kHz) for air decomposition. In the gas sample that contained SF₆, which is the main content, the voltage should be greater than this for CF₄ decomposition. However, a further step of our concept is to try this equipment to observe the possibility of conversion, discharge power, and contamination of its design.

To study the selectivity improvement of CO₂ and CO under plasma application at the low level of CF₄, lower than 100 ppm, would investigate in future work. At this point, as we have known that PFCs are not easily be decomposed because of their stable C-F and tetrahedral structure. Many factors should be investigated, such as an applied voltage, decomposition time, frequency, O₂ content addition, or plasma catalytic. Especially, the thermal plasma application, arc plasma, or plasma torches should be considered the important factor to improve the CF₄ conversion efficiency.

4.6 Summary

A novel scheme for detecting residual carbon tetrafluoride (CF₄) gas in gas-insulated switchgear (GIS) is presented. CF₄ is one of the decomposition gases that occurred after partial discharge or breakdown in GIS, which accumulates in long-span usage because it is hard to be removed by absorbent in GIS. Therefore, the CF₄ can act as the failure indicator in the GIS. The purpose of this study is to investigate the possibility of a new concept; the indirect detection of CF₄ by converting CF₄ in SF₆ background gas with additional O₂ into easily detectable CO₂ and CO, under dielectric barrier discharge (DBD) application. The maximum selectivities of CO₂ and CO measured by Fourier transform infrared (FT-IR) were 7.33% (10% O₂ addition) and 8.33% (1% O₂ addition), respectively. Moreover, the performance of the commercial CO sensor was tested in the experimental environment, and it had a similar trend as FT-IR. The presented scheme can apply in the practical application for GIS diagnosis.

Chapter 5

Gas sensor fabricated by two-step dielectrophoretic assembly

5.1 Introduction

As described in Chapter 3, further works investigated nanomaterial combination for the CF₄ gas sensor fabricated by DEP. In this chapter, I reported some parts of my research studies related to nanomaterial combination. Nowadays, the challenges in hybrid material-based gas sensing is the key attention [129]. I selected this technique applied to fabricate NO₂ gas sensors by two-step dielectrophoretic assembly. It appeared the sensitivity enhanced when the mixture ratio and materials of the combination were suitable [130]. Combination technique might be the essential key to develop CF₄ detection in future work.

A literature review, D. Wang *et.al* [131] report the first-principles calculations to investigate the sensing properties for the systematically study of the adsorption behavior of SF₆ decomposition products (H₂S, SO₂, SO₂F₂, and SOF₂) on germanium phosphide (GeP) monolayer by using first-principles calculations. The results show that SO₂ molecules are physically adsorbed on GeP monolayer with the largest adsorption energy and the greatest charge transfer compared to other molecules. It can be seen from this study that the hybrid material can be used to improve the selectivity and sensitivity.

5.2 Nitrogen Oxide (NO₂)

Nitrogen dioxide (NO₂), which is widely generated in industry and transportation, is one of the major gas species of air pollution. The average NO₂ concentration in the atmosphere is ~30 ppb [132]. For NO₂ detection, spectrophotometry and chemiluminescence are the established gas detection methods [129]. However, these methods require expensive and large equipment, and the optical system is sensitive to vibrations. Therefore, small, cheap, and robust NO₂ gas sensors are necessary for environmental monitoring.

The semiconducting gas sensor has widely been investigated for environmental monitoring [129]. Because only a small amount of semiconducting nanoparticles is used as the transducer, the cost of the gas sensor can be reduced. Among the semiconducting

nanoparticles, semiconducting carbon nanotubes (CNTs) have shown good potential for gas detection at room temperature [133–137]. When CNTs bridge the electrodes, the micro electrode used in this work is the same structure in Chapter 3, the individual CNTs act as a conductive channel, and they are well modulated by adsorbed gas species, such as NO₂ [138, 139]. In addition, nanoparticle decoration of CNTs enhances the sensitivity of gas detection [140-150]. In particular, tin dioxide (SnO₂) particle decoration of CNTs has been shown to enable an enhancement of the gas sensitivity at room temperature [139] because of the formation of pn hetero-junctions at the CNT/SnO₂ interfaces [139].

Various methods have been reported to form CNT channels for CNT-based gas sensors, such as dispersed CNT network formation [151–153], single CNT bridging, [154, 155] and DEP assembly [156–158]. Among them, the DEP assembly is a powerful method to produce aligned CNT channels. When small dielectric materials are located in a high non-uniform electric field, the polarization of the particles occurs, and the polarized particle can be moved by the DEP force. CNTs are effectively polarized owing to their high aspect ratio. Our group has reported the DEP assembly of CNTs and other nanoparticles [157, 159–161]. To fabricate SnO₂-decorated CNT (CNT/SnO₂) gas sensors, it is necessary to attach SnO₂ nanoparticles onto the CNT surfaces. SnO₂ nanoparticles should be assembled by the DEP method when a high electric field is formed on the CNT surface. In this chapter, I fabricated CNT/SnO₂ gas sensors by a two-step DEP assembly method, and investigated the NO₂ gas detection properties.

5.3 Experiment

To fabricate the CNT/SnO₂ gas sensor devices, CNTs and SnO₂ particles were assembled by a two-step DEP assembly, as shown in Figure 5.1a. First, CNTs were assembled by DEP between the electrodes. Second, SnO₂ nanoparticles were decorated also by the DEP, where the CNTs acted as electrodes generating the high electric field around them. SnO₂ nanoparticles were effectively attached to the CNT surface, and formed pn hetero-junctions at the CNT/SnO₂ interfaces. To validate the two-step DEP assembly method, the second DEP assembly was simulated using COMSOL Multiphysics (ver. 5.4). To study particle movement, I selected the particle tracing for fluid flow for physics interfaces and configured the electrode which applied electric field.

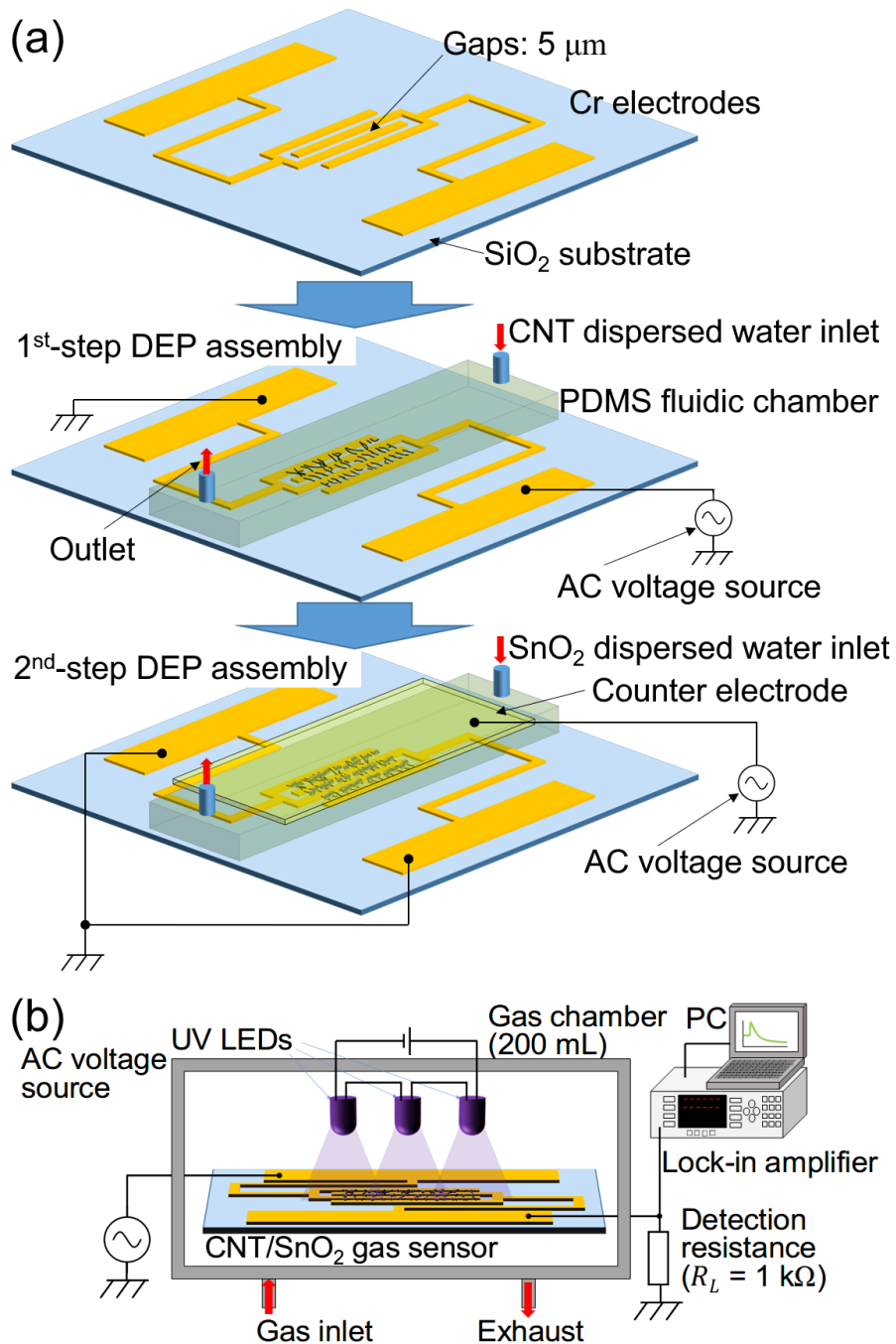


Figure 5.1. (a) Schematic of the two-step DEP assembly method. CNTs and SnO_2 nanoparticles were assembled during the first or second DEP assembly, respectively. In the second DEP assembly, CNTs acted as the grounded electrodes. SnO_2 nanoparticles were attracted by CNTs by the DEP force. (b) Schematic of the NO_2 gas detection system [130].

I fabricated the devices with the two-step DEP assembly. The chromium interdigitated microelectrodes were fabricated on a glass substrate. The gap between fingers, the finger width, and the total finger length were adjusted to 5 μm , 50 μm , and 36 mm, respectively. The semiconducting CNT-dispersed solution (99.9% in purity) was purchased from NanoIntegris Co., Ltd., QC, Canada. The average diameter and length of the CNTs were 1.4 nm and 1 μm , respectively. The CNTs were assembled in the first step of the DEP assembly. The microfluidic channel, as described in Chapter 3, formed by polydimethylsiloxane (PDMS) was placed on the substrate, and CNT-dispersed water with a concentration of 100 ng/ml was circulated for 5, 10, and 15 min with flow rate of 0.8 ml/min. Simultaneously, an AC voltage of 20 V_{pp} at 100 kHz was applied to the electrodes. The CNT assembly was confirmed by dielectrophoretic impedance measurement (DEPIM) [28]. The conductance increased as CNTs assembled between the microelectrodes. Next, the top counter electrode was placed on the CNT channel. The microelectrodes on the substrate were connected to the ground, where the assembled CNTs had the same potential, and an AC voltage of 20 V_{pp} at 100 kHz was applied between the ground including CNTs and the top counter electrode. SnO_2 -dispersed water with a concentration of 1 mg/ml was circulated for 5 min, 15 min, and 60 min with flow rate of 0.8 ml/min. SnO_2 nanoparticles were purchased from Kanto Chemical Co., Ltd., and the diameter was distributed in the range of 14–120 nm. The solution was replaced with deionized water, and an AC voltage was applied. After replacing the counter electrode with the PDMS microfluidic channel, the sample was annealed at 150 $^\circ\text{C}$ for 2 h in air to evaporate the surface solution. The formed device was observed by SEM.

A schematic of the gas sensing system is shown in Figure 5.1b. The CNT/ SnO_2 sensor was placed in a stainless-steel chamber, volume 160 cm^3 , and the atmosphere was replaced by nitrogen gas with a continuous flow followed by surface initialization by UV irradiation for typically 2 h. UV light-emitting diodes (365 nm, 9.2 mW/cm^2 , NS365L-ERLM, Nitride Semiconductors Co., Ltd., Tokushima, Japan) were used as the UV light source. After the UV light was turned off, 1 ppm of NO_2 diluted by N_2 gas was introduced to the gas chamber with the flow rate of 350 sccm. The impedance of the sensor was measured by a lock-in amplifier. Here, the impedance of the CNT/ SnO_2 gas sensors was calculated from the impedance of the external detection resistance. The resistance R of the sensor corresponded to that of the RC parallel equivalent circuit of the sensor. It was calculated that the normalized response as the resistance change as $\Delta R/R_0 = (R - R_0)/R_0$,

where R and R_0 were the resistances during NO_2 exposure and just after initialization, respectively.

5.4 Result and discussion

To validate the two-step DEP assembly method, I simulated the second DEP assembly step using COMSOL Multiphysics (ver. 5.4), as the first DEP assembly has already been established [157]. For the second-step DEP assembly, the CNTs were already assembled between the microelectrodes, and they acted as electrodes. The regions near the CNTs had a high electric field by applying an AC voltage of $0.1 V_{\text{rms}}$ between the interdigitated electrodes and the counter electrode, which were located $5 \mu\text{m}$ from each other. Because the counter electrode was located $\sim 900 \mu\text{m}$ from the microelectrodes in the real system, the value of the AC voltage in the simulation was determined as a proportionate voltage for a distance of $5 \mu\text{m}$. CNTs were bridged between the microelectrodes, which corresponded to the situation where CNTs were assembled between the microelectrodes with the $5\text{-}\mu\text{m}$ gap by the DEP assembly method.

The simulation result of an electric field is shown in Figure 5.2a. A high electric field was formed around the CNTs. The particle behavior was simulated, as shown in Figure 5.2b. Here, the particle was SnO_2 , where the relative dielectric constant of SnO_2 and the solution, the conductivity of SnO_2 and the solution, and the SnO_2 particle size were set to 11.527 and 80, 1 S/m and 1×10^{-4} S/m, and 100 nm, respectively. Electric property of SnO_2 nanoparticle was from Ref. The applied frequency was 100 kHz. The SnO_2 nanoparticles were attracted to the CNTs by the positive DEP force. Thus, the SnO_2 particles were decorated on the CNTs by a two-step DEP method.

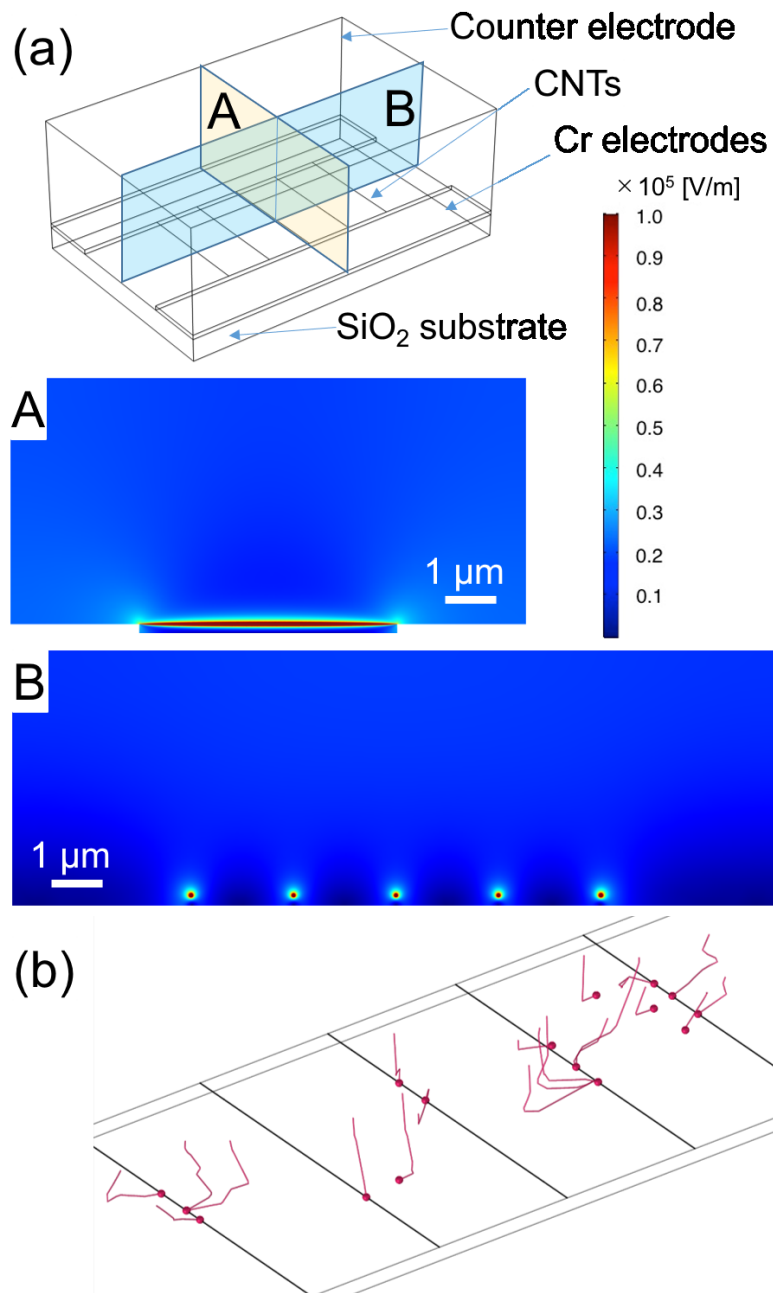


Figure 5.2. (a) Electric field simulation results for the second-step DEP assembly. Five CNTs are bridged over the 5- μm electrode gap and electrically connected to microelectrodes. Thus, CNTs act as thin electrodes. High electric field is formed around the CNTs. (b) Simulation result of SnO₂ particle movement by a DEP force induced by the high electric field around CNTs. Red lines indicate trajectories of the particle. It was calculated that the particle movements for 0.8ms [130].

To confirm the device fabrication, SEM images of the channel were obtained, as shown in Figure 5.3. The image after the first step of the DEP method was Figure 5.3a. CNTs bridged between the electrodes. CNTs formed bundles between the microelectrodes, and some intervals existed between the bundles. Figures 5.3b–5.3e show the SEM images after the two-step DEP assembly with assembly times of CNTs and SnO₂ of (b) 15 min and 5 min, (c) 15 min and 15 min, (d) 15 min and 60 min, and (e) 5 min and 60 min. The number of apparent SnO₂ nanoparticles increased as the ratio of the SnO₂/CNT assembly time increased. For a low SnO₂/CNT assembly time ratio, SnO₂ nanoparticles were sparsely deposited on the CNT sidewalls [Figures 5.3b–5.3d]. For a high SnO₂/CNT assembly time ratio, SnO₂ nanoparticles assembled and formed large clusters on the CNTs [Figure. 5.3e].

Additionally, to confirm that the SnO₂ nanoparticles were attracted by the electric field formed by CNTs, SnO₂ nanoparticles were assembled by the DEP with the counter electrode without CNTs, as shown in Figure. 5.3f SnO₂ nanoparticles were not assembled between the microelectrode gaps and assembled mainly at the outer edges of them. Because the potential of the microelectrodes was the same, the electric field between the microelectrodes was low. Then, SnO₂ nanoparticles were not assembled between the microelectrodes. When the CNTs were assembled between the microelectrodes in advance, the CNTs effectively formed a high electric field and attracted the SnO₂ nanoparticles.

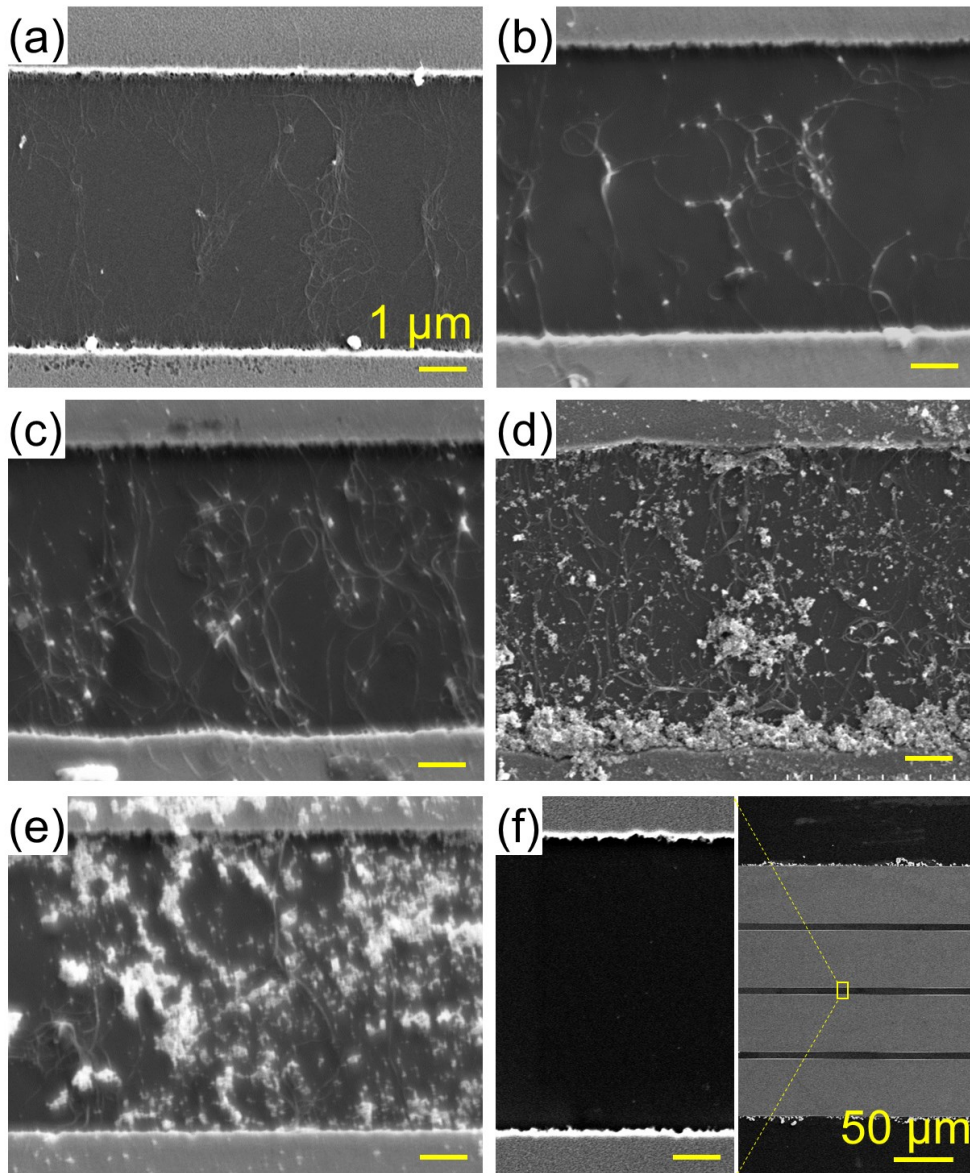


Figure 5.3. SEM images of Cr electrode gaps (a) after the first step DEP assembly, (b)–(e) after the second-step DEP assembly, and (f) after the second-step DEP without the first CNT assembly. The CNT/SnO₂ DEP assembly times are (b) 15 min/5 min, (c) 15 min/15 min, (d) 15 min/60 min, and (e) 5 min/60 min, respectively. The scale bars in (a)–(e) and the left figure in (f) corresponds to 1 μm [130].

The gas responses of the CNT/SnO₂ gas sensors are shown in Figure. 5.4a. NO₂ with a concentration of 1 ppm diluted by N₂ was introduced from 60 s and reached the chamber around 70 s. The resistance quickly increased for ~30 s and then gradually decreased in all samples. For comparison, sensors using the CNT only and the SnO₂ only were fabricated Their 1-ppm NO₂ responses are shown in Figure. 5.4b.

The normalized resistance decreased for the CNT channel gas sensor, and increased for the SnO₂ channel gas sensor upon NO₂ exposure. Because CNT and SnO₂ are ordinary p-type and n-type semiconductors, these sensor responses in resistance decreased and increased, respectively. The response of the SnO₂ gas sensor quickly saturated to be positive, while that of the CNT gas sensor slowly decreased.

The normalized resistance varied for the CNT and SnO₂ DEP assembly conditions. To investigate the relationship between the DEP assembly condition and the sensor response, the highest normalized resistances were plotted as the function of the ratio of the SnO₂/CNT DEP assembly time, as shown in Figure. 5.4c. As the assembly time ratio increased, the normalized response increased, and became the highest at the ratio of 4, which corresponded to DEP assembly times of 15 min and 60 min for CNT and SnO₂, respectively. For a higher ratio, the normalized response was reduced.

For further investigation, the NO₂ concentration dependence of the sensor was measured for the CNT/SnO₂ gas sensor with the highest response, as shown in Figure. 5.4d. For the normalized response with 100 ppb of NO₂, the resistance gradually increased compared with that with 1 ppm and reached a response of ~10. After reaching the maximum resistance, it decreased slowly. Note that the time when the resistance began to increase was long for low concentration NO₂ exposure, which stemmed from the mass-flow control system rather than the sensor properties. For 50 ppb of NO₂, the resistance increased even slower. The response of the sensor was confirmed for less than 50 ppb. Although a slight increase in resistance was observed for 10 ppb, this may be the long-term shift of the sensor resistance. The maximum response did not linearly depend on the NO₂ concentration.

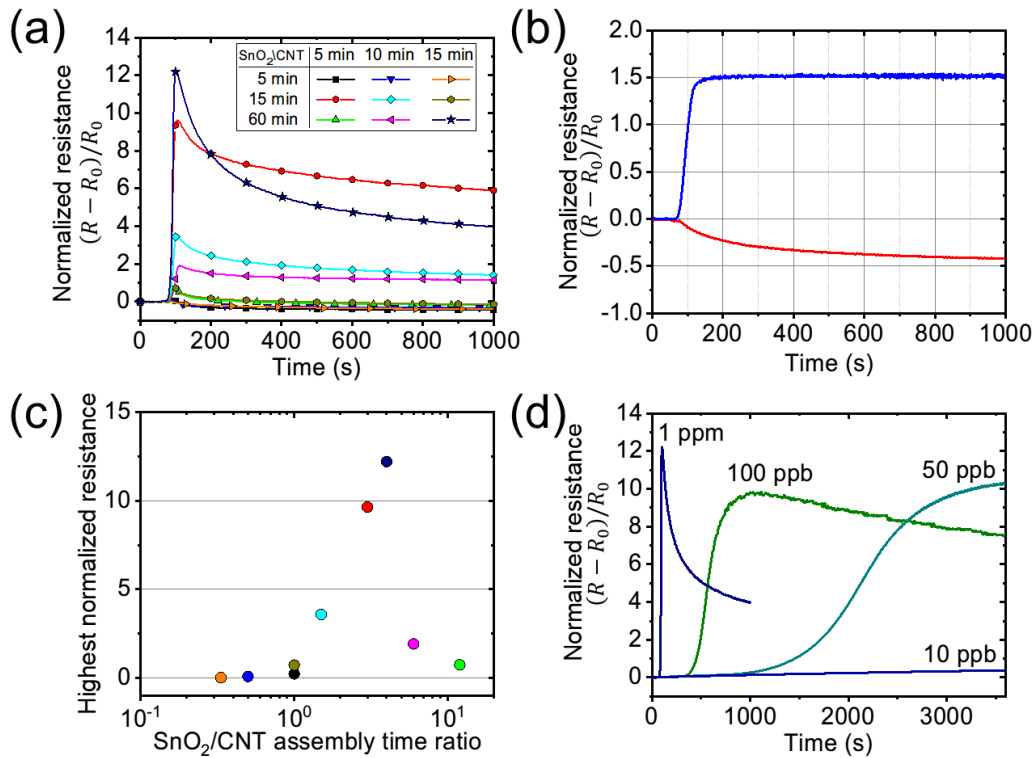


Figure 5.4. Normalized resistance characteristics of (a) CNT/SnO₂ gas sensors and (b) CNT (red line) and SnO₂ (blue line) gas sensors, for 1 ppm of NO₂. (c) Highest normalized resistance as a function of the SnO₂/CNT assembly time ratio. The color of the plots corresponds to that of the characteristics curves in (a). {add error bars} (d) Normalized resistance characteristics of CNT/SnO₂ gas sensors with the highest response (CNT: 15 min/SnO₂: 60 min) for low NO₂ concentration [130].

To understand the response of the CNT/SnO₂ gas sensor, I proposed an equivalent circuit and a response mechanism of the CNT/SnO₂ gas sensors. The large response was derived from the resistance change of the CNT/SnO₂ pn hetero-junctions, though CNTs without SnO₂ decoration may exist in the sensor channel. The resistances of the sensors with the CNT only (after the first step of the DEP assembly for 15 min) and with the CNT/SnO₂ (after the second step of the DEP assembly for 60 min) without UV initialization were ~4 kΩ and 50 kΩ in air, respectively. This indicated that the resistance of the CNTs increased by decorating with SnO₂ nanoparticles. If CNT and SnO₂ were connected in parallel, the resistance should decrease. Therefore, the equivalent circuit of this sensor is that shown in Figure 5.5a, where the resistances of the CNTs R_{CNT} and

CNT/SnO₂ pn hetero-junction $R_{p/n}$ were connected in series.

When the gas sensor was initialized by UV irradiation in N₂ atmosphere, the number of CNTs was depleted and exhibited a high resistance at the CNT/SnO₂ pn hetero-junctions, as shown in Figure 5b. When NO₂ molecules approached the channel, the SnO₂ nanoparticles quickly responded to NO₂ gas adsorption, and an electron in SnO₂ was transferred to molecular NO₂ [163]. The depletion region expanded and the resistance of the CNT/SnO₂ pn heterojunction regions $R_{p/n}$ increased, as shown in Figure 5.5c. The NO₂ gas response rate of SnO₂ nanoparticles was faster than that of CNTs from the response shown in Figure 5.4b. After the NO₂ response of SnO₂ nanoparticles became saturated, the response of the CNT surfaces to NO₂ gas molecules became apparent. An electron in the CNTs was also transferred to NO₂ gas molecules and the hole carrier induced by surface negative adsorbates. The depletion region shrunk by the additional carriers in the CNTs, and the resistance of the CNT/SnO₂ pn hetero-junction regions $R_{p/n}$ gradually decreased, as shown in Figure 5.5d. Here, the resistance of the CNTs R_{CNT} also decreased by the increase in carrier density in the CNTs. For low concentration NO₂ gas exposure, the gas adsorption rate should decrease, and the response rate should decrease. The resistance increase, and the following decrease for an NO₂ gas response to 100 ppb was slower those that to 1 ppm. Because NO₂ gas molecules adsorbed to both SnO₂ nanoparticles and CNTs, the shape of the response remained for a low concentration. Although only a resistance increase was observed for 50 ppb of NO₂, the resistance should decrease for further NO₂ exposure.

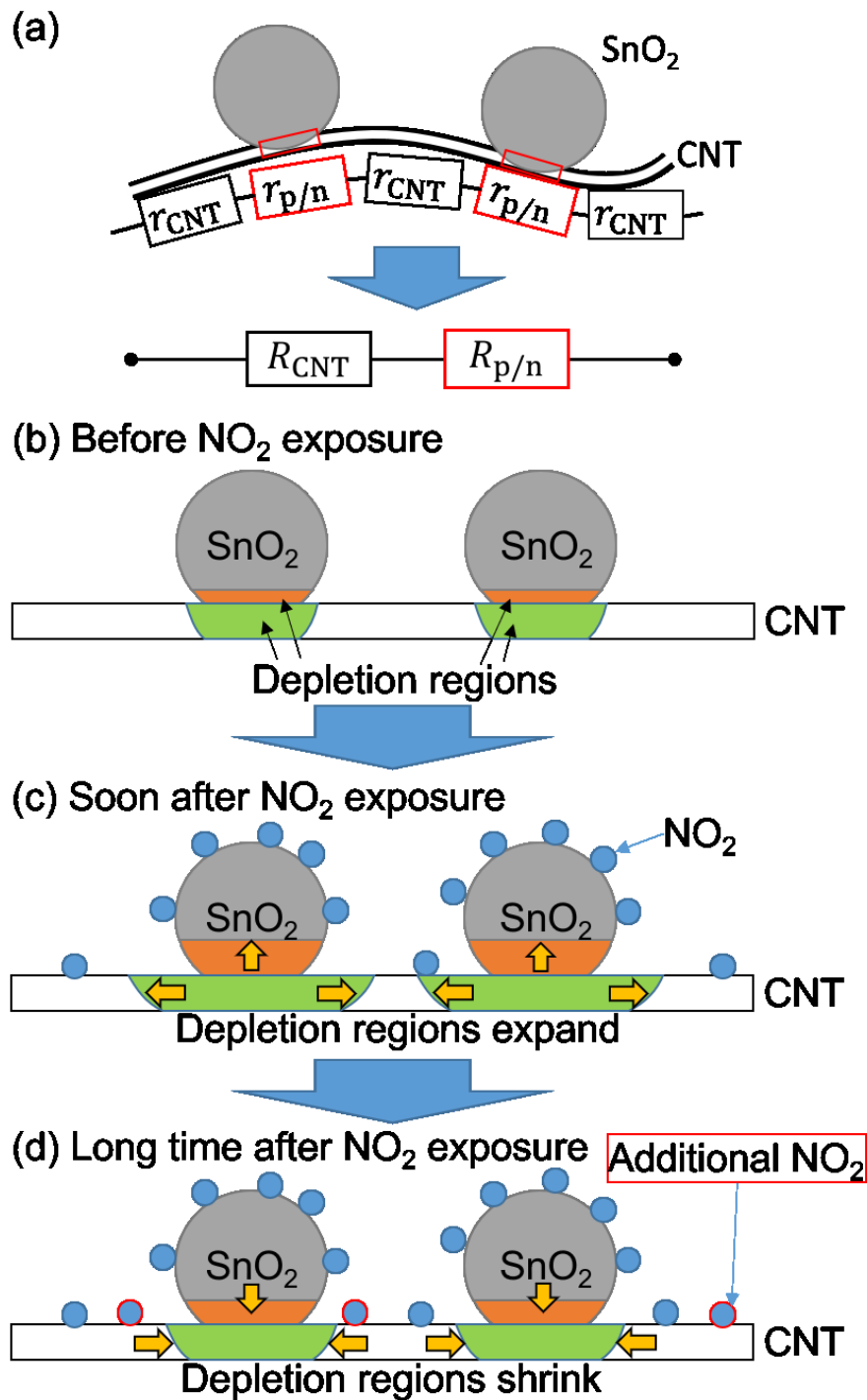


Figure 5.5 (a) Equivalent circuit of the CNT/ SnO_2 gas sensor. (b)–(d) Schematic of the CNT and decorated SnO_2 nanoparticles (b) before NO_2 exposure, (c) soon after NO_2 exposure, and (d) long time after NO_2 exposure [130].

Note that I considered that the charge transfer between SnO₂ and NO₂ was dominant, while some reports have shown oxygen vacancies at the SnO₂ surface trap NO₂ gas molecules to result in a gas response [163–170]. This is because the CNT/SnO₂ gas sensor is operated at room temperature, so the oxygen vacancies are not active as reaction sites. Ruhland *et al.* [163] reported that a high temperature is necessary for the reaction to occur. Additionally, I confirmed that the resistance after initialization was almost the same for repeated use. If oxygen vacancies at the SnO₂ surface trap NO₂ gas molecules, the number of oxygen vacancies decreases and the resistance of the SnO₂ film should change by repeated use.

According to this model, when the SnO₂ amount is small, the first response should be low. Conversely, as the ratio of the SnO₂/CNT DEP assembly time increases, the number of CNT/SnO₂ pn hetero-junction increases, which corresponds to the tendency observed by SEM, as shown in Figures 5.2b–5.2d. The increase in the resistance of pn hetero-junction caused the high sensor response. For a higher assembly ratio, the normalized response decreased. This arose from the DEP assembly method. If SnO₂ particles attach to the CNT surface, the SnO₂ nanoparticles could form a high electric field around them. If the density of SnO₂ nanoparticles increases, additional nanoparticles could be attracted by the high electric field formed at SnO₂ nanoparticles attached on CNTs.

To confirm this phenomenon, I simulated the electric field distribution in the case of a SnO₂ nanoparticle attached on a CNT surface using COMSOL Multiphysics, as shown in Figure. 5.6. The electric field around the attached nanoparticle became high, and the high electric field attracted other nanoparticles. When the density of SnO₂ nanoparticles in the solution is increased, the probability of a SnO₂ nanoparticle attracted to the attached SnO₂ nanoparticle should be increased. Then, SnO₂ nanoparticles tended to pile up and form large SnO₂ clusters on the CNT network, as shown in Figure 5.3e. The effective number of SnO₂ nanoparticles was decreased by the formation of SnO₂ clusters for a long SnO₂ assembly time, which resulted in the low response. Therefore, this two-step DEP fabrication of the CNT/SnO₂ gas sensor has the limitation of SnO₂ decoration to CNTs. It is possible to improve the sensor response by enhancing the density of SnO₂ nanoparticles decorated on the CNT surface. In this case, the decrease in resistance, as exhibited in Figure. 5.5d, should be suppressed because the regions of bare CNTs are decreased, where the SnO₂ nanoparticles are not decorated. The DEP assembly

method should be further improved to enhance the gas response.

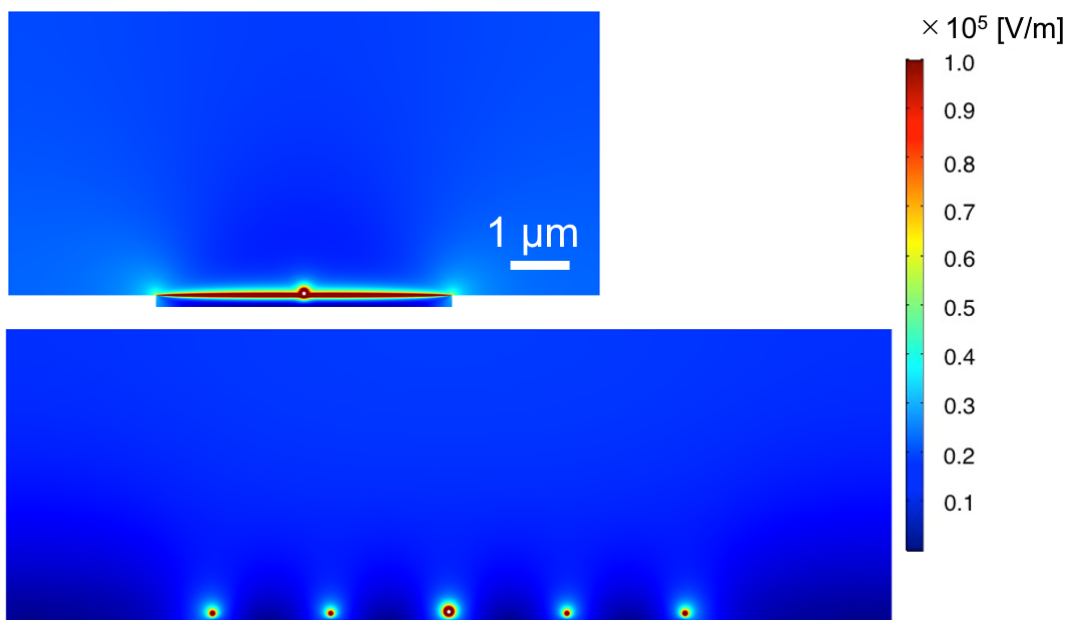


Figure. 5.6. Electric field cross-sectional images across a SnO₂ nanoparticle decorated on a CNT simulated using COMSOL Multiphysics [130].

5.5 Perspective for the detection of CF₄ and CO

I demonstrated the example of application of material combination for gas sensor fabricated by DEP techniques. While direct CF₄ detection by using a single SnO₂ nanomaterial-based gas sensor could not reach the target limit of detection. There are many researchers reported the results of combination and decoration [171-177]. To enable the high sensitivity, these studies would assist to improve my final goal in next steps.

For instance, the recent publication of CO gas sensors, Moseley [178] reports in a review research article about the combination between TiO₂ and Au, which can reach a detection limit lower than 10 ppm at operating temperature 325°C. Especially, gas responses of oxides modified by the addition of precious metals are reported. Dey [179] demonstrated that the SnO₂/Pt fabricated by the sol-gel technique shows a detection limit lower than 10 ppm at operating temperature 350°C. Gong reports a high sensitivity of Cu-doped ZnO film. The result shows the response against 6 ppm at 150°C [180].

In the case of CF₄, Nomura *et al.* [91] demonstrated the detection of fluorocarbon gases by using an SnO₂ doped with various elements. The results show that when SnO₂ doped by sulfur, tungsten and germanium, the response of the sensor is increased to 12, 4.40, and 4.00-fold of initial response, respectively.

However, as described in Chapter 4, the cross sensitivity of the sensor was seriously concerned. Again, if we need to detect CO or CO₂. After decomposition process, there were many gas species occurred, then they would affect to the sensor responses. Therefore, the cross sensitivity would be the one of important factor that we have to pay concentration in our research in future.

5.6 Summary

A CNT/SnO₂ composite gas sensor for NO₂ detection was fabricated by a two-step DEP assembly method. In the first DEP assembly, CNTs are assembled between comb-shaped electrodes, and SnO₂ is additionally assembled on the CNTs in the second DEP assembly, where the CNTs act as electrodes with a high electric field. To validate this two-step DEP assembly method, the electric field formed by the CNTs was simulated. The formed CNT/SnO₂ gas sensor exhibits a sharp increase in resistance followed by a gradual decrease upon NO₂ exposure. pn hetero-junctions are formed between the CNTs and the SnO₂ nanoparticles, and the resistance shift of the depletion region in the CNT at

the pn hetero-junction induces the sharp resistance increase.

In GIS, the choice of the different components of the hybrid materials used as CF₄, CO or CO₂ sensing materials. The most essential key that need to be paid is the cross-sensitivity with other decomposition gases.

Chapter 6

Conclusion

Improving the reliability and stability of the power system is the essential key to the success of the economy and world business. GIS is one of the main apparatuses to reach the goal. For maintaining the reliability and stability of the system, GIS diagnosis techniques have been studied widely. One of them is the chemical diagnosis technique which has a unique advantage and interesting for GIS application.

In this research, direct and indirect CF₄ detection were expected to apply for GIS diagnosis. The present study proposed to develop a detection of the residual CF₄ in GIS. The CF₄ detection method was divided into 2 cases of study. The former is direct CF₄ detection by using nanomaterial-based gas sensors. The latter is indirect CF₄ detection by CF₄ conversion, then detect the by-product of it, CO and CO₂, under dielectric barrier discharge application. We attempted to study the possibility and the limitation of the proposed methods. Finally, we could summarize it as follows.

1. Direct detection method, SnO₂ gas sensor fabricated by DEP could detect 10000-ppmCF₄ and showed the highest response among them (SnO₂, ZnO, and CNT) but demonstrated an inadequate response. It appeared that 10000-ppm CF₄ should be the detection limited.

2. Indirect detection, 100-ppmCF₄ could be converted into CO and CO₂ under dielectric barrier discharge application. A commercially CO gas sensor can detect converted CO, which was very close to the target CF₄ concentration for GIS diagnosis.

3. Detection of CF₄ and its decomposition gases, CO and CO₂, should be studied by a material combination for gas sensor fabricated by DEP.

The results show that direct and indirect CF₄ can be used for residual CF₄ diagnosis in GIS, although the proposed methods have been limited by sensitivity. When discussing the three methods described above, the first and third methods, using single and hybrid nanomaterial, can be used to direct CF₄ detection. Still, the improvement point is the sensitivity and cross-sensitivity of the selected materials for CF₄, CO, or CO₂ sensor fabrication. In the case of CF₄ conversion into CO and CO₂, there are two close attention points. The former, improvement of increasing conversion, and the latter, improvement of the small-size system.

I concluded the comparative effectiveness among methods used in the GIS field and our proposed methods in Table 6.1. However, this study was the first stage of CF₄ detection. We have known the problems, the way to solve them and any key to achieve discussed in each chapter. The proposed direct and indirect CF₄ detection needs to be improved in future work.

The novelty and strong points of the research to the GIS diagnostic engineering field are concluded below.

1. Revealed that CF₄/O₂/SF₆ gas mixture can generate CO and CO₂ by using NTP
2. CF₄ target is unique and worth observing for GIS diagnosis.
3. The CF₄ target can be applied to any compartment in GIS installed and not installed an absorbent.
4. Concepts of the research, including rapid tests, inexpensive, on-site tests, lead to the high impact of GIS diagnosis
5. Improvement of detection limitations is possible.

Additionally, I would like to list some research topics for future objectives below.

1. The study on the adsorption reaction between the metal oxide-based gas sensor and CF₄ using an atomic-scale material modeling software such as Vienna Ab initio Simulation and Atomistix ToolKit.

- 2 Single nanomaterial with their decoration and hybrid materials for increasing performance of gas sensors.

3. Downsizing of CF₄ conversion system and high CF₄ conversion ratio improvement

4. Rapid tests, inexpensive systems, and on-site tests are required for completing this study.

Finally, point of view of social and commercial aspect, world electricity consumption highly increased including industry, residential, service, transport, other final uses, and power service sector. Power system, including generation, transmission, and distribution, is the essential key for economic growth in our world. The reliability and quality of the power system indicate how is the business movement significantly. Low reliability and quality of the power system affect to mass production of any business. Especially in the industry field, the electricity outage and shutdown are not acceptable. For example, as described in Chapter 1, which explains the loose cost during electricity shutdown. GIS is one part of the power system. My research pays attention to how to

diagnose the GIS when GIS is under abnormal conditions. The research is based on rapid test, inexpensive, and on-site tests. Under these concepts of research, this technique will be highly effective in the GIS diagnosis engineering field. If we can diagnose and know the main problem fast, we will resolve the problem fast, and it issues a small impact.

Nowadays, using the power system diagnosis integrating automation, machine learning, big data analysis, and the internet of things (IoT) is high performance to maintain and recovery the power system. I believed that my research would be useful when it is integrated with the other system as described earlier. The integration concept is shown in Fig. 6.1. GIS is monitored and analyzed by the integration system. Finally, we cannot say that which part of the power system is the highest necessary. In fact, every aspect of the system needs to be developed and integrated into other systems at the same time. Recently, world electricity consumption will increase continuously and every second of the business world is high value. Therefore, the reliability and quality of the power system will be constantly improved as well.

However, this technique is under research. In the current stage, the proposed methods have not been achieved the final goal yet. Advances in the term of detection sensitivity and small-size design are required in the future study. In my opinion, the target gas, CF₄, is to be unique and different from the other decomposition gases as described in Chapter 2. The successful CF₄ detection method would be high impact and value for GIS diagnostic engineering field.

Table 6.1. Effectiveness among gas analysis methods

Effective	GC	FT-IR	SF ₆ Gas analyzer	CF ₄ Direct detection	CF ₄ Indirect detection
Measuring time (min) (not include warm-up time)	10	1	10	30	60
Sensitivity limit (ppm)	~10, Depends on detector	<1	<1 (SO ₂ , HF, H ₂ S, CO)	10000	100
On-site	No	No	Yes	Possible	Possible
Cost/unit	~2 M¥	~3 M¥	~2 M¥	~0.5 M¥	~0.5 M¥
Size	Large	Large	Compact	Need improvement	Need improvement

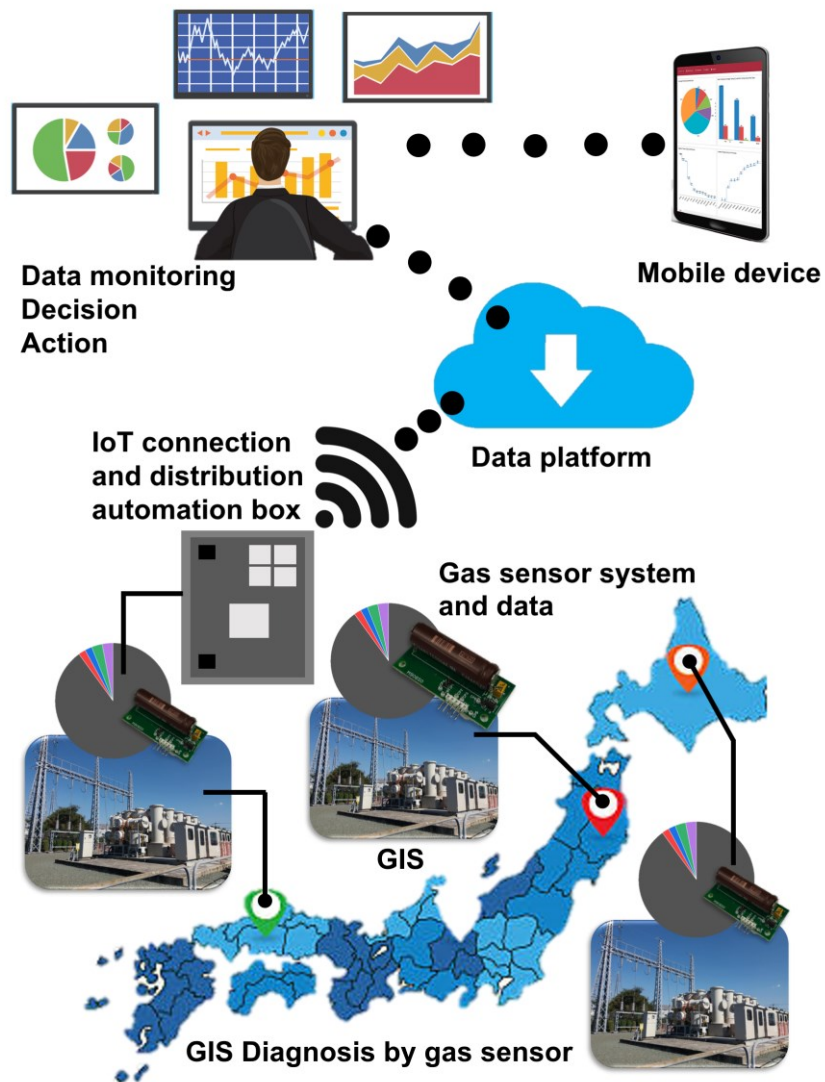


Figure. 6.1. Integration concept among GIS diagnosis by gas sensor, internet of things, big data analysis.

References

- [1] Enerdata, “Breakdown by country,” Global Energy Statistical Yearbook, 2019. <https://yearbook.enerdata.net/>.
- [2] B. Zohuri, “Application of compact heat exchangers for combined cycle driven efficiency in next generation nuclear power plants: A novel approach,” *Appl. Compact Heat Exch. Comb. Cycle Driven Effic. Next Gener. Nucl. Power Plants A Nov. Approach*, no. October, pp. 1–366, 2015, doi: 10.1007/978-3-319-23537-0.
- [3] IEA, “World Energy Outlook 2019,” *World Energy Outlook 2019*, 2019.
- [4] H. Guo, C. Zheng, H. H. C. Iu, and T. Fernando, “A critical review of cascading failure analysis and modeling of power system,” *Renew. Sustain. Energy Rev.*, vol. 80, no. May, pp. 9–22, 2017, doi: 10.1016/j.rser.2017.05.206.
- [5] H. H. Alhelou, M. E. Hamedani-Golshan, T. C. Njenda, and P. Siano, “A survey on power system blackout and cascading events: Research motivations and challenges,” *Energies*, vol. 12, no. 4, pp. 1–28, 2019, doi: 10.3390/en12040682.
- [6] O. P. Veloza and F. Santamaria, “Analysis of major blackouts from 2003 to 2015: Classification of incidents and review of main causes,” *Electr. J.*, vol. 29, no. 7, pp. 42–49, 2016, doi: 10.1016/j.tej.2016.08.006.
- [7] Toshiba Corporation, <https://www.toshiba.com/tic/product/>
- [8] G. Mauthe and K. Pettersson. “Handling of SF₆ and its decomposition products in gas insulated switchgear (GIS), 1st part”, *Electra*, Vol. 136, pp. 69-89, Jun. 1991
- [9] G. Mauthe and K. Pettersson. “Handling of SF₆ and its decomposition products in gas insulated switchgear (GIS), 2st part”, *Electra*, Vol. 137, pp. 81-106, Aug. 1991.
- [10] Gas Insulated Switchgear Market 2020-2027, Industry Report, <https://www.mordorintelligence.com/industry-reports/gas-insulated-switchgear-market>.
- [11] I. A. Metwally, “Technology progress in high-voltage gas-insulated substations,” *IEEE Potentials*, vol. 29, no. 6, pp. 25–32, Nov. 2010, doi: 10.1109/MPOT.2010.939085.

- [12] I. Metwally, "Status review on partial discharge measurement techniques in gas-insulated switchgear/lines," *Electr. Power Syst. Res.*, vol. 69, no. 1, pp. 25–36, Apr. 2004, doi: 10.1016/j.epsr.2003.07.006.
- [13] T. A. Paul, "Optical technologies in the power industry: Monitoring and diagnosis of gas-insulated electrical switchgear," ABB.
- [14] Working Group B3-03, "Improving the impact of existing substations on the environment," *CIGRÉ Tech. Broch. No. 221*, no. June, p. 68, 2003, [Online]. Available: <http://www.cigre.org>.
- [15] X. Fang et al., "Sulfur hexafluoride (SF₆) emission estimates for China: An inventory for 1990-2010 and a projection to 2020," *Environ. Sci. Technol.*, vol. 47, no. 8, pp. 3848–3855, 2013, doi: 10.1021/es304348x.
- [16] Y. Wang, D. Huang, J. Liu, Y. Zhang, and L. Zeng, "Alternative environmentally friendly insulating gases for SF₆," *Processes*, vol. 7, no. 4, 2019, doi: 10.3390/pr7040216.
- [17] A. Beroual and A. Haddad, "Recent advances in the quest for a new insulation gas with a low impact on the environment to replace Sulfur Hexafluoride (SF₆) gas in high-voltage power network applications," *Energies*, vol. 10, no. 8, 2017, doi: 10.3390/en10081216.
- [18] P. Afzali and F. Keynia, "Lifetime efficiency index model for optimal maintenance of power substation equipment based on cuckoo optimisation algorithm," *IET Gener. Transm. Distrib.*, vol. 11, no. 11, pp. 2787–2795, 2017, doi: 10.1049/iet-gtd.2016.1719.
- [19] G. Balzer, O. Schmitt, M Halfmann, A. Hoble, "Maintenance and refurbishment strategies for M.V. Substations," <http://www.cired.net/publications>.
- [20] H. M. Heise, R. Kurte, P. Fischer, D. Klockow, and P. R. Janissek, "Gas analysis by infrared spectroscopy as a tool for electrical fault diagnostics in SF₆ insulated equipment," *Fresenius. J. Anal. Chem.*, vol. 358, no. 7–8, pp. 793–799, 1997, doi: 10.1007/s002160050511.
- [21] S. Yoshida, H. Kojima, N. Hayakawa, F. Endo, and H. Okubo, "Light emission spectrum depending on propagation of Partial Discharge in SF₆," *Conf. Rec. IEEE Int. Symp. Electr. Insul.*, pp. 365–368, 2008, doi: 10.1109/ELINSL.2008.4570350.

- [22] A. Schei, S. Kyrkjeeide, and V. Larsen, "Acoustic insulation analyzer for periodic condition assessment of gas insulated substations," *Proc. IEEE Power Eng. Soc. Transm. Distrib. Conf.*, vol. 2, no. ASIA PACIFIC, pp. 919–924, 2002, doi: 10.1109/tdc.2002.1177599.
- [23] M. D. Judd, O. Farish, and B. F. Hampton, "The excitation of UHF signals by partial discharges in GIS," *IEEE Trans. Dielectr. Electr. Insul.*, vol. 3, no. 2, pp. 213–228, 1996, doi: 10.1109/94.486773.
- [24] M. Dong, C. Zhang, M. Ren, R. Albarracín, and R. Ye, "Electrochemical and infrared absorption spectroscopy detection of SF₆ decomposition products," *Sensors (Switzerland)*, vol. 17, no. 11, Nov. 2017, doi: 10.3390/s17112627.
- [25] A. Dourdour, J. Casanovas, R. Hergli, R. Grob, and J. Mathieu, "Study of the decomposition of wet SF₆, subjected to 50-Hz ac corona discharges," *J. Appl. Phys.*, vol. 65, no. 5, pp. 1852–1857, 1989, doi: 10.1063/1.342919.
- [26] J.M. Braun and F.Y. Chu, "Novel low-cost SF₆ arcing byproduct detectors for field use in gas-insulated switchgear", *IEEE Trans. Power. Syst*, vol. PWRD-1, No.2, April 1986
- [27] Q. Khan, S. S. Refaat, H. Abu-Rub, and H. A. Toliyat, "Partial discharge detection and diagnosis in gas insulated switchgear: State of the art," *IEEE Electr. Insul. Mag.*, vol. 35, no. 4, pp. 16–33, 2019, doi: 10.1109/MEI.2019.8735667.
- [28] A. Bargigia, W. Koltunowicz, and A. Pigin, "Detection of partial discharges in gas insulated substations," *IEEE Trans. Power Deliv.*, vol. 7, no. 3, pp. 1239–1249, 1992.
- [29] G. Wang, H.-E. Jo, S.-J. Kim, S.-W. Kim, and G.-S. Kil, "Measurement and analysis of partial discharges in SF₆ gas under HVDC," *Meas. J. Int. Meas. Confed.*, vol. 91, pp. 351–359, 2016.
- [30] F. Álvarez, F. Garnacho, J. Ortego, and M. Á. Sánchez-Urán, "Application of HFCT and UHF Sensors in On-Line Partial Discharge Measurements for Insulation Diagnosis of High Voltage Equipment," *Sensors (Switzerland)*, vol. 15, no. 4, pp. 7360–7387, Mar. 2015.
- [31] R. Bell, C. Charlson, S. Halliday, T. Irwin, J. Lopez-Roldan, and J. Nixon, "High-Voltage On-Site Commissioning Tests for Gas-Insulated Substations Using UHF Partial Discharge Detection," *IEEE Power Eng. Rev.*, vol. 22, no. 6, p. 61 2002.
- [32] T. Yamagiwa, H. Yamada, F. Endo, Y. Ohshita, S. Izumi, and I. Yamada,

- “Development of Preventive Maintenance System for Highly Reliable Gas Insulated Switchgear,” *IEEE Trans. Power Deliv.*, vol. 6, no. 2, pp. 840–848, 1991.
- [33] A. Bargigia, W. Koltunowicz, and A. Pigin, “Detection of partial discharges in gas insulated substations,” *IEEE Trans. Power Deliv.*, vol. 7, no. 3, pp. 1239–1249, 1992.
- [34] H. Okubo and A. Beroual, “Recent trend and future perspectives in electrical insulation techniques in relation to sulfur hexafluoride (SF₆) substitutes for high voltage electric power equipment,” *IEEE Elec. Insul. Mag.*, vol. 27, no. 2, pp. 34–42, 2011.
- [35] L. E. Lundgaard, M. Runde, and B. Skyberg, “Acoustic diagnosis of gas insulated substations: a theoretical and experimental basis,” *IEEE Trans. Power Deliv.*, vol. 5, no. 4, pp. 1751–1759, 1990.
- [36] Y. Li, D. Chen, L. Li, J. Zhang, G. Li, and H. Liu, “Study of comparison between Ultra-high Frequency (UHF) method and ultrasonic method on PD detection for GIS,” *IOP Conf. Ser. Earth Environ. Sci.*, vol. 94, p. 012086, Nov. 2017.
- [37] D. F. Binns, A. H. Mufti, and N. H. Malik, “Optical Discharge Detection in SF₆-insulated Systems,” *IEEE Trans. Electr. Insul.*, vol. 25, no. 2, pp. 405–414, 1990.
- [38] S. Yoshida, H. Kojima, N. Hayakawa, F. Endo, and H. Okubo, “Spectrum Depending on of Partial Discharge in SF₆,” in *Conference Record of the 2008 IEEE International Symposium on Electrical Insulation*, vols. 1 and 2, 2008, pp. 365–368.
- [39] H. Ji, et al, “Moving behaviors and harmfulness analysis of multiple linear metal particles in GIS,” *IEEE Trans. Dielectr. Electr. Insul.*, vol. 23, no. 6, pp. 3355–3363, 2016.
- [40] S. Okabe, S. Kaneko, T. Minagawa, and C. Nishida, “Detecting characteristics of SF₆ decomposed gas sensor for insulation diagnosis on gas insulated switchgears,” *IEEE Trans. Dielectr. Electr. Insul.*, vol. 15, no. 1, pp. 251–258, 2008.
- [41] F. Y. Chu, “SF₆ Decomposition in Gas-Insulated Equipment,” *IEEE Trans. Electr. Insul.*, vol. EI-21, no. 5, pp. 693–725, 1986.
- [42] V. M. Ibrahim, Z. Abdul-Malek, and N. A. Muhamad, “Status review on gas insulated switchgear partial discharge diagnostic technique for preventive maintenance,” *Indonesian Journal of Electrical Engineering and Computer Science*, vol. 7, no. 1, pp. 9–17, 2017.

- [43] D. Koch, "Cahier technique no. 188 SF₆ properties, and use in MV and HV switchgear." [Online]. Available: <http://www.schneider-electric.com>..
- [44] J. Tang, F. Liu, X. Zhang, Q. Meng, and J. Zhou, "Partial Discharge Recognition through an Analysis of SF₆ Decomposition Products Part 1: Decomposition Characteristics of SF₆ under Four Different Partial Discharges," *IEEE Trans. Dielectr. Electr. Insul.*, 2012.
- [45] L. G. Christophorou and D. W. Bouldin, *Gaseous dielectrics V: proceedings of the Fifth International Symposium on Gaseous Dielectrics*, Knoxville, Tennessee, U.S.A., May 3-7, 1987. Pergamon Press, 1987.
- [46] F. Zeng et al., "SF₆ fault decomposition feature component extraction and triangle fault diagnosis method," *IEEE Trans. Dielectr. Electr. Insul.*, vol. 27, no. 2, pp. 581–589, 2020, doi: 10.1109/TDEI.2019.008370.
- [47] J. Tang, F. Liu, Q. Meng, X. Zhang, and J. Tao, "Partial discharge recognition through an analysis of SF₆ decomposition products part 2: Feature extraction and decision tree-based pattern recognition," *IEEE Trans. Dielectr. Electr. Insul.*, vol. 19, no. 1, pp. 37–44, 2012, doi: 10.1109/TDEI.2012.6148500.
- [48] H. J. Koch, *Gas Insulated Substations*. Wiley, 2014.
- [49] N. K. Rajalwal and D. Ghosh, "Recent trends in integrity protection of power system: A literature review," *Int. Trans. Electr. Energy Syst.*, vol. 30, no. 10, pp. 1–43, 2020, doi: 10.1002/2050-7038.12523.
- [50] M. Elsis, M.-Q. Tran, K. Mahmoud, D.-E. A. Mansour, M. Lehtonen, and M. M. F. Darwish, "Towards Secured Online Monitoring for Digitalized GIS Against Cyber-Attacks Based on IoT and Machine Learning," *IEEE Access*, pp. 1–1, 2021, doi: 10.1109/access.2021.3083499.
- [51] X. Zhou et al., "Partial Discharge Pattern Recognition of Transformer Based on Deep Learning," *Gaoya Dianqi/High Volt. Appar.*, vol. 55, no. 12, pp. 98–105, 2019, doi: 10.13296/j.1001-1609.hva.2019.12.014.
- [52] Future Distribution Substation with Integrated IoT Connection, Siemens
- [53] D. Koch, "Cahier technique no. 188 SF₆ properties, and use in MV and HV switchgear." [Online]. Available: <http://www.schneider-electric.com>.
- [54] Techiescientist, <https://techiescientist.com/cf4-lewis-structure>, 2021.
- [55] Carbon Tetrafluoride, <https://www.americanelements.com/carbon-tetrafluoride-75-73-0>.

- [56] F. Y. Chu, "SF₆ Decomposition in gas-insulated equipment", IEEE Trans. Dielectr. Electr. Insul., vol. EI-21 No.5, October 1986
- [57] J. Manion, J. Philosophos, and M. Robinson, "Arc Stability of Electronegative Gases," IEEE Trans. Electrical Insulation, EI-1 Vol. 1, 1967.
- [58] Y. Murakami and S. Menju, "Fundamental Techniques in Gas-Insulated Apparatus," Toshiba Review, Vol.77, 23, p. 2713, 1973
- [59] J. Lampe, H. Latour-Slowikowka, and J. Slowikowska, "Study on Metal Fluoride Product Formation Caused by an Electric Arc in SF₆," Gaseous Dielectrics III, L. G. Christophorou (Ed.) Pergamon Press, p. 433, 1982
- [60] Q. Cai, A. Buts, N.A. Seaton and M. J. Biggs, "Characterization of the porosity of a microporous model carbon", Studies in Surface Science and Catalysis 160 P.L. Llewellyn, F. Rodriguez-Reinoso, J. Rouquerol and N. Seaton (Editors)
- [61] J. Duan, M. Higuchi, R. Krishna, T. Kiyonaga, Y. Tsutsumi, Y. Sato, Y. Kubota, M. Takata, and S. Kitagawa, "High CO₂/N₂/O₂/CO Separation in a Chemically Robust Porous Coordination Polymer with Low Binding Energy", Electronic Supplementary Material (ESI) for Chemical Science, this journal is © The Royal Society of Chemistry 2013
- [62] ゼオライトの吸着特性, <https://jza-online.org/about/q3>
- [63] Q. Huang, Y. Wang, J. Liu, Y. Zhang, and L. Zeng, "Study on the compatibility of Gas Adsorbents used in a new insulating Gas Mixture C₄F₇N/CO₂," Processes, vol. 7, no. 10, 2019, doi: 10.3390/pr7100698.
- [64] Q. Cai, A. Buts, N.A. Seaton and M. J. Biggs, "Characterization of the porosity of a microporous model carbon", Studies in Surface Science and Catalysis 160 P.L. Llewellyn, F. Rodriguez-Reinoso, J. Rouquerol and N. Seaton (Editors)
- [65] 電力中央研究所 2017 年度委託成果報告書, 66kV GIS のガス分析に基づく状態診断と解体調査立会いにおける内部調査
- [66] H. Shinkai, "Study of loose connection diagnosis method for SF₆ gas disconnecter using SF₆ decomposition gas," IEEJ Trans. Power Energy, vol. 137, no. 6, pp. 453–459, 2017, doi: 10.1541/ieejpes.137.453.
- [67] N. Phansiri, D. Maenosono, T. Furumoto, and M. Nakano, "Necessary Sensitivity of CF₄ Gas Sensor for Gas Insulated Switchgear Diagnosis," no. 2, p. 2019, 2019.
- [68] G. Korotcenkov, "Integrated Analytical Systems Series Editor: Radislav A. Potyrailo Handbook of Gas Sensor Materials." [Online]. Available:

- <http://www.springer.com/series/7427>.
- [69] J. Suehiro, R. Yatsunami, R. Hamada, and M. Hara, "Quantitative estimation of biological cell concentration suspended in aqueous medium by using dielectrophoretic impedance measurement method," 1999. [Online]. Available: <http://iopscience.iop.org/0022-3727/32/21/316>.
- [70] J. Suehiro, G. Zhou, H. Imakiire, W. Ding, and M. Hara, "Controlled fabrication of carbon nanotube NO₂ gas sensor using dielectrophoretic impedance measurement," in *Sensors and Actuators, B: Chemical*, Jul. 2005, vol. 108, no. 1-2 SPEC. ISS., pp. 398–403, doi: 10.1016/j.snb.2004.09.048.
- [71] J. Suehiro et al., "Dielectrophoretic fabrication and characterization of a ZnO nanowire-based UV photosensor," *Nanotechnology*, vol. 17, no. 10, pp. 2567–2573, May 2006, doi: 10.1088/0957-4484/17/10/021.
- [72] Y. Martin et al., "Detection of SF₆ Decomposition Products Generated by DC Corona Discharge Using a Carbon Nanotube Gas Sensor," *IEEE Trans. Dielectr. Electr. Insul*, 2012.
- [73] W. Ding et al., "Analysis of PD-generated SF₆ Decomposition Gases Adsorbed on Carbon Nanotubes Analysis of PD-generated SF₆ Decomposition Gases Adsorbed on Carbon Nanotubes," *IEEE Trans. Dielectr. Electr. Insul*, 2006.
- [74] W. Ding, R. Hayashi, J. Suehiro, G. Zhou, and M. Hara, "Calibration Methods of Carbon Nanotube Gas Sensor for Partial Discharge Detection in SF₆," *IEEE Trans. Dielectr. Electr. Insul*, 2006.
- [75] Z. Ding, H. Kasahara, M. Nakano, and J. Suehiro, "Bacterial detection based on polymerase chain reaction and microbead dielectrophoresis characteristics," *IET Nanobiotechnology*, vol. 11, no. 5, pp. 562–567, 2017, doi: 10.1049/iet-nbt.2016.0186.
- [76] P. Cools, N. De Geyter, and R. Morent, *Plasma-Catalytic Removal of VOCs*. 2019.
- [77] C. F. Ou Yang, S. H. Kam, C. H. Liu, J. Tzou, and J. L. Wang, "Assessment of removal efficiency of perfluorocompounds (PFCs) in a semiconductor fabrication plant by gas chromatography," *Chemosphere*, vol. 76, no. 9, pp. 1273–1277, 2009, doi: 10.1016/j.chemosphere.2009.06.039.
- [78] Z. M. El-Bahy, R. Ohnishi, and M. Ichikawa, "Hydrolysis of CF₄ over alumina-based binary metal oxide catalysts," *Appl. Catal. B Environ.*, vol. 40, no. 2, pp.

- 81–91, 2003, doi: 10.1016/S0926-3373(02)00143-1.
- [79] M. Setareh, M. Farnia, A. Maghari, and A. Bogaerts, “CF₄ decomposition in a low-pressure ICP: Influence of applied power and O₂ content,” *J. Phys. D. Appl. Phys.*, vol. 47, no. 35, Sep. 2014, doi: 10.1088/0022-3727/47/35/355205.
- [80] S. Jen Yu and M. Been Chang, “Oxidative Conversion of PFC via Plasma Processing with Dielectric Barrier Discharges,” 2001.
- [81] Y. Kim, K. T. Kim, M. S. Cha, Y. H. Song, and S. J. Kim, “CF₄ decompositions using streamer- and glow-mode in dielectric barrier discharges,” *IEEE Trans. Plasma Sci.*, vol. 33, no. 3, pp. 1041–1046, Jun. 2005, doi: 10.1109/TPS.2005.848616.
- [82] T. Kuroki, J. Mine, M. Okubo, et al., “CF₄ decomposition using inductively coupled plasma: Effect of power frequency,” *IEEE Trans. Ind.*, 2005, 41, (1), pp. 215-220, doi:10.1109/TIA.2004.840948
- [83] K.L. Pan, Y.S. Chen, M.B. Chang, “Effective removal of CF₄ by combining nonthermal plasma with γ -Al₂O₃”, *Plasma Chemistry and Plasma Processing*, 2019, 39, (4), pp. 877-896, doi:10.1007/s11090-019-09990-9.
- [84] F. J. Arregui, “Sensors Based on Nanostructured Materials”, Springer Science&Business Media, LLC 2009
- [85] X. Liu, S. Cheng, H. Liu, S. Hu, D. Zhang, and H. Ning, “A survey on gas sensing technology,” *Sensors (Switzerland)*, vol. 12, no. 7. pp. 9635–9665, Jul. 2012, doi: 10.3390/s120709635.
- [86] M. V. Nikolic, V. Milovanovic, Z. Z. Vasiljevic, and Z. Stamenkovic, “Semiconductor gas sensors: Materials, technology, design, and application,” *Sensors (Switzerland)*, vol. 20, no. 22, pp. 1–31, 2020, doi: 10.3390/s20226694.
- [87] A. Dey, “Semiconductor metal oxide gas sensors: A review,” *Materials Science and Engineering B: Solid-State Materials for Advanced Technology*, vol. 229. Elsevier Ltd, pp. 206–217, Mar. 01, 2018, doi: 10.1016/j.mseb.2017.12.036.
- [88] A. Sharma, A. Ahmed, A. Singh, S. K. Oruganti, A. Khosla, and S. Arya, “Review—Recent Advances in Tin Oxide Nanomaterials as Electrochemical/Chemiresistive Sensors,” *J. Electrochem. Soc.*, vol. 168, no. 2, p. 027505, 2021, doi: 10.1149/1945-7111/abdee8.
- [89] E. Llobet, “Gas sensors using carbon nanomaterials: A review,” *Sensors Actuators, B Chem.*, vol. 179, pp. 32–45, 2013, doi: 10.1016/j.snb.2012.11.014.

- [90] N. Phansiri, D. Maenosono, T. Furumoto, H. Sato, M. Nakano and J. Suehiro, "Detection of CF₄ gas using a nanomaterial-based gas sensor fabricated by dielectrophoresis," *ISH 2019, LNEE 598 [Proceedings of the 21st International Symposium on High Voltage Engineering, Vol. 1, pp.481-488, 2020]*.
- [91] T. Nomura, T. Amamoto, Y. Matsuura, and Y. Kajiyama, "Development of semiconductor fluorocarbon gas sensor," *Sensors Actuators B. Chem.*, vol. 13, no. 1–3, pp. 486–488, 1993, doi: 10.1016/0925-4005(93)85434-C.
- [92] L. Zhu and W. Zeng, "Room-temperature gas sensing of ZnO-based gas sensor: A review," *Sensors Actuators, A Phys.*, vol. 267, pp. 242–261, 2017, doi: 10.1016/j.sna.2017.10.021.
- [93] J. Szuber, *Semiconductor gas sensors*, vol. 30, no. 2. 1997.
- [94] G. Korotcenkov, "Metal oxides for solid-state gas sensors: What determines our choice?," *Materials Science and Engineering B: Solid-State Materials for Advanced Technology*, vol. 139, no. 1. pp. 1–23, Apr. 25, 2007, doi: 10.1016/j.mseb.2007.01.044.
- [95] N. Barsan, D. Koziej, and U. Weimar, "Metal oxide-based gas sensor research: How to?," *Sensors Actuators, B Chem.*, vol. 121, no. 1, pp. 18–35, Jan. 2007, doi: 10.1016/j.snb.2006.09.047.
- [96] N. Bârsan and U. Weimar, "Understanding the fundamental principles of metal oxide based gas sensors; the example of CO sensing with SnO₂ sensors in the presence of humidity," 2003.
- [97] I. V. Zaporotskova, N. P. Boroznina, Y. N. Parkhomenko, and L. V. Kozhitov, "Carbon nanotubes: Sensor properties. A review," *Mod. Electron. Mater.*, vol. 2, no. 4, pp. 95–105, 2016, doi: 10.1016/j.moem.2017.02.002.
- [98] A. Aqel, K. M. M. A. El-Nour, R. A. A. Ammar, and A. Al-Warthan, "Carbon nanotubes, science and technology part (I) structure, synthesis and characterisation," *Arab. J. Chem.*, vol. 5, no. 1, pp. 1–23, 2012, doi: 10.1016/j.arabjc.2010.08.022.
- [99] *LIGA and its Applications Microengineering of Metals Reliability of MEMS 3D Laser Microfabrication Microengineering of Metals*, vol. 8.
- [100] L. Camilli and M. Passacantando, "Advances on sensors based on carbon nanotubes," *Chemosensors*, vol. 6, no. 4, pp. 1–17, 2018, doi: 10.3390/chemosensors6040062.

- [101] T. B. Jones, "Electromechanics of particles", Cambridge university press.
- [102] M. Dimaki and P. Bøggild, "Dielectrophoresis of carbon nanotubes using microelectrodes: A numerical study," *Nanotechnology*, vol. 15, no. 8, pp. 1095–1102, 2004, doi: 10.1088/0957-4484/15/8/039.
- [103] D. Wang et al., "A first principles theoretical study of the adsorption of SF₆ decomposition gases on a cassiterite (110) surface," *Mater. Chem. Phys.*, vol. 212, pp. 453–460, Jun. 2018, doi: 10.1016/j.matchemphys.2018.03.084.
- [104] X. Zhang, F. Meng, and B. Yang, "Use of Hydroxyl-modified Carbon Nanotubes for Detecting SF₆ Decomposition Products under Partial Discharge," *IEEE Trans. Dielectr. Electr. Insul.*, 2013.
- [105] N. Phansiri, X. Liu, M. Inaba, M. Nakano, J. Suehiro, and H. Sato, "Indirect detection of residual CF₄ in gas-insulated switchgear via conversion under dielectric barrier discharge," *International Journal of Plasma Environmental Science and Technology (IJPEST)*, 2021.
- [106] Y. Zhuang et al., "Effects of SF₆ decomposition components and concentrations on the discharge faults and insulation defects in GIS equipment," *Sci. Rep.*, vol. 10, no. 1, pp. 1–12, 2020, doi: 10.1038/s41598-020-72187-0.
- [107] L. Kai, J. Shengchang, Z. Lipeng, and Z. Lingyu, "The mechanism of SF₆ decomposition characteristics under partial discharge at different gas pressures and voltage," *C. 2016 - Int. Conf. Cond. Monit. Diagnosis*, pp. 578–581, 2016, doi: 10.1109/CMD.2016.7757892.
- [108] S. Kusumoto, S. Itoh, Y. Tsuchiya, H. Mukae, S. Matsuda, and K. Takahashi, "Diagnostic technique of gas insulated substation by partial discharge detection," *IEEE Trans. Power Appar. Syst.*, vol. PAS-99, no. 4, pp. 1456–1465, 1980, doi: 10.1109/TPAS.1980.319569.
- [109] T. Ushio, I. Shimura, and S. Tominaga, "Practical Problem on SF₆ Gas Circuit Breaker," *IEEE Winter Power Meeting*, New York, paper 71 TP64-PWR, January 1970.
- [110] Z. Cui, X. Zhang, T. Yuan, P. Xingya, Y. Luo, and J. Tang, "Plasma-assisted abatement of SF₆ in a dielectric barrier discharge reactor: Investigation of the effect of packing materials," *J. Phys. D. Appl. Phys.*, vol. 53, no. 2, 2020, doi: 10.1088/1361-6463/ab4ba7.
- [111] M. Schmidt, R. Schneider, and H. Wagner, *Physics of Nonthermal Plasmas*. 2013.

- [112] J. R. Roth, "Industrial Plasma Engineering," *Ind. Plasma Eng.*, 2001, doi: 10.1201/9781420034127.
- [113] H. E. Wagner, R. Brandenburg, K. V. Kozlov, A. Sonnenfeld, P. Michel, and J. F. Behnke, "The barrier discharge: Basic properties and applications to surface treatment," *Vacuum*, vol. 71, no. 3 SPEC., pp. 417–436, 2003, doi: 10.1016/S0042-207X(02)00765-0.
- [114] N. Phansiri, D. Maenosono, M. Inaba, and M. Nakano, "Detection of Decomposition Products of CF₄/SF₆ Gas Mixture Generated by Partial Discharge Using a SnO₂ Gas Sensor Fabricated by Dielectrophoresis," *Proceeding of the IEEJ Technical Meeting, Kyushu, Japan, January 24-25, 2020*
- [115] N. Phansiri, D. Maenosono, M. Inaba, M. Nakano, J. Suehiro, and H. Sato, "A New Scheme for Residual CF₄ Detection in Gas-Insulated Switchgear Using Plasma-induced CF₄ Decomposition into CO₂," *8th CMD*, pp. 54–57, 2020, doi: 10.1109/cmd48350.2020.9287294.
- [116] Miwa Kohei, 三輪 航平, GIS 設備診断のための誘電体パリア放電による CF₄分解と生成 CO/CO₂の検出, 電気情報工学科, 九州大学, 令和3年2月.
- [117] J. P. Lodge, "Handbook of ozone technology and applications," *Atmospheric Environment* (1967), vol. 17, no. 5. p. 1040, 1983, doi: 10.1016/0004-6981(83)90273-1.
- [118] NIST Chemistry WebBook, SRD 69, <https://webbook.nist.gov/>
- [119] Technical Information for Carbon Monoxide Sensors TGS5042, Figaro
- [120] EM5042A - Evaluation Module for TGS5042, Figaro
- [121] S. Edition, Chapter I Theoretical Background, vol. 42. 1967.
- [122] B. C. Smith, *Fundamentals of fourier transform infrared spectroscopy*, second edition. 2011.
- [123] *LabSolutions IR Instruction Manual*, Shimadzu, 2020.
- [124] Y. A. Virolainen et al., "Introduction to Gas Phase FTIR Spectroscopy Introduction to FTIR spectroscopy," *J. Appl. Spectrosc.*, vol. 16, no. 7, pp. 12–20, 2016.
- [125] M. Alexandre and M. Gerboles, "Review of small commercial sensors for indicative monitoring of ambient gas," *Chem. Eng. Trans.*, vol. 30, no. x, pp. 169–174, 2012, doi: 10.3303/CET1230029.
- [126] T. Kuroki, J. Mine, M. Okubo, T. Yamamoto, and N. Saeki, "CF₄ decomposition

- using inductively coupled plasma: Effect of power frequency,” *IEEE Trans. Ind. Appl.*, vol. 41, no. 1, pp. 215–220, Jan. 2005, doi: 10.1109/TIA.2004.840948.
- [127] K. L. Pan, Y. S. Chen, and M. B. Chang, “Effective Removal of CF₄ by Combining Nonthermal Plasma with γ -Al₂O₃,” *Plasma Chem. Plasma Process.*, vol. 39, no. 4, pp. 877–896, Jul. 2019, doi: 10.1007/s11090-019-09990-9.
- [128] Ozonefac Limited, ceramic ozone tube, <https://www.ozonefac.com/product/Ceramic-Ozone-Tube.html>.
- [129] T. Print, “Advanced Nanomaterials for Inexpensive Gas Microsensors,” *Adv. Nanomater. Inexpensive Gas Microsens.*, 2020, doi: 10.1016/c2017-0-02009-8.
- [130] M. Inaba, M. Kono, T. Oda, N. Phansiri, M. Nakano, and J. Suehiro, “Response properties of nitrogen dioxide gas sensors with tin oxide decorated carbon nanotube channel fabricated by two-step dielectrophoretic assembly,” *AIP Adv.*, vol. 10, no. 5, 2020, doi: 10.1063/5.0008188.
- [131] D. Wang, T. Lan, A. Yang, J. Pan, J. Chu, H. Yuan, Y. Li, X. Wang, and M. Rong, “SF₆ Decomposition Gas Sensor Based on GeP,” vol. 20, no. 16, pp. 8997–9003, 2020.
- [132] Ministry of the Environment Government of Japan, “Environmental Quality Standards in Japan - Air Quality [MOE],” pp. 2–3, 2009, [Online]. Available: <https://www.env.go.jp/en/air/aq/aq.html%0Ahttp://www.env.go.jp/en/air/aq/aq.html#header>.
- [133] M. M. Rana, D. S. Ibrahim, M. R. Mohd Asyraf, S. Jarin, and A. Tomal, “A review on recent advances of CNTs as gas sensors,” *Sens. Rev.* 37, 127 (2017).
- [134] D. Kumar, P. Chaturvedi, P. Saho, P. Jha, A. Chouksey, M. Lal, J. S. B. S. Rawat, R. P. Tandon, and P. K. Chaudhury, “Effect of single wall carbon nanotube networks on gas sensor response and detection limit.” *Sens. Actuators, B* 240, 1134 (2017).
- [135] Y. Li, M. Hodak, W. Lu, and J. Bernholc, “Mechanisms of NH₃ and NO₂ detection in carbon-nanotube-based sensors: An ab initio investigation.” *Carbon* 101, 177(2016).
- [136] J. Li, Y. Lu, Q. Ye, M. Cinke, J. Han, and M. Meyyappan, “Carbon nanotube sensors for gas and organic vapor detection.” *Nano Lett.* 3, 929 (2003).
- [137] C. Cantalini, L. Valentini, I. Armentano, L. Lozzi, J. M. Kenny, and S. Santucci, “Sensitivity to NO₂ and cross-sensitivity analysis to NH₃, ethanol and humidity

- of carbon nanotubes thin film prepared by PECVD.” *Sens. Actuators, B* 95, 195 (2003).
- [138] H. Song, K. Li, and C. Wang, “Selective detection of NO and NO₂ with CNTs-based ionization sensor array,” *Micromachines*, vol. 9, no. 7, pp. 14–17, 2018, doi: 10.3390/mi9070354.
- [139] F. Mendoza, D. M. Hernández, V. Makarov, E. Febus, B. R. Weiner, and G. Morell, “Room temperature gas sensor based on tin dioxide-carbon nanotubes composite films,” *Sensors Actuators, B Chem.*, vol. 190, pp. 227–233, 2014, doi: 10.1016/j.snb.2013.08.050.
- [140] H. C. Su, M. Zhang, W. Bosze, and N. V. Myung, *J. Electrochem. Soc.* 161, B283 (2014). “Tin dioxide functionalized single-walled carbon nanotube (SnO₂/SWNT)-based ammonia gas sensors and their sensing mechanism,”
- [141] A. Sharma, M. Tomar, and V. Gupta, *J. Mater. Chem.* 22, 23608 (2012). “Room temperature trace level detection of NO₂ gas using SnO₂ modified carbon nanotubes based sensor.”
- [142] R. Leghrib, A. Felten, J. J. Pireaux, and E. Llobet, *Thin Solid Films* 520, 966 (2011). “Gas sensors based on doped-CNT/SnO₂ composites for NO₂ detection at room temperature.”
- [143] Q. T. Minh Nguyet, N. Van Duy, N. T. Phuong, N. N. Trung, C. M. Hung, N. D. Hoa, and N. Van Hieu, “Superior enhancement of NO₂ gas response using n-p-n transition of carbon nanotubes/SnO₂ nanowires heterojunctions,” *Sens. Actuators, B* 238, 1120 (2017).
- [144] Q. T. M. Nguyet, N. Van Duy, C. Manh Hung, N. D. Hoa, and N. Van Hieu, “Ultrasensitive NO₂ gas sensors using hybrid heterojunctions of multi-walled carbon nanotubes and on-chip grown SnO₂ nanowires.” *Appl. Phys. Lett.* 112, 153110 (2018).
- [145] N. Zhao, G. Wang, Y. Huang, B. Wang, B. Yao, and Y. Wu, “Preparation of Nanowire Arrays of Amorphous Carbon Nanotube-Coated Single Crystal SnO₂,” *Chem. Mater.* 20, 2612 (2008).
- [146] B.-Y. Wei, M.-C. Hsu, P.-G. Su, H.-M. Lin, R.-J. Wu, and H.-J. Lai, “A novel SnO₂ gas sensor doped with carbon nanotubes operating at room temperature.” *Sens. Actuators, B* 101, 81 (2004).
- [147] V. Srivastava and K. Jain, “At room temperature graphene/SnO₂ is better than

- MWCNT/SnO₂ as NO₂ gas sensor,” *Mater. Lett.* 169, 28 (2016).
- [148] A. Star, V. Joshi, S. Skarupo, D. Thomas, and J.-C. P. Gabriel, “Gas Sensor Array Based on MetalDecorated Carbon Nanotubes,” *J. Phys. Chem. B* 149, 21014 (2006)
- [149] T. Print, “Advanced Nanomaterials for Inexpensive Gas Microsensors,” *Adv. Nanomater. Inexpensive Gas Microsens.*, 2020, doi: 10.1016/c2017-0-02009-8.
- [150] S. Park, S. An, Y. Mun, and C. Lee, “UV-Enhanced NO₂ Gas Sensing Properties of SnO₂-Core/ZnO-Shell Nanowires at Room Temperature,” *ACS Appl. Mater. Interfaces* 5, 4285 (2013).
- [151] A. Abdelhalim, M. Winkler, F. Loghin, C. Zeiser, P. Lugli, and A. Abdellah, “Highly sensitive and selective carbon nanotube-based gas sensor arrays functionalized with different metallic nanoparticles,” *Sens. Actuators, B* 220, 1288 (2015).
- [152] T. Zhang, M. B. Nix, B.-Y. Yoo, M. A. Deshusses, and N. V. Myung, “Electrochemically functionalized single-walled carbon nanotube gas sensor,” *Electroanalysis* 18, 1153 (2006).
- [153] K. H. An, S. Y. Jeong, H. R. Hwang, and Y. H. Lee, “Enhanced Sensitivity of a Gas Sensor Incorporating Single-Walled Carbon Nanotube-Polypyrrole Nanocomposites,” *Adv. Mater.* 16, 1005 (2004).
- [154] T. Helbling, R. Pohle, L. Durrer, C. Stampfer, C. Roman, A. Jungen, M. Fleischer, and C. Hierold, “Sensing NO₂ with individual suspended single-walled carbon nanotubes,” *Sens. Actuators, B* 132, 491 (2008).
- [155] M. Mattmann, C. Roman, T. Helbling, D. Bechstein, L. Durrer, R. Pohle, M. Fleischer, and C. Hierold, “Pulsed gate sweep strategies for hysteresis reduction in carbon nanotube transistors for low concentration NO₂ gas detection,” *Nanotechnology* 21, 185501 (2010).
- [156] J. Suehiro, G. Zhou, and M. Hara, J. “Fabrication of a carbon nanotube-based gas sensor using dielectrophoresis and its application for ammonia detection by impedance spectroscopy,” *Phys. D: Appl. Phys.* 36, L109 (2003).
- [157] J. Suehiro, G. Zhou, H. Imakiire, W. Ding, and M. Hara, “Controlled fabrication of carbon nanotube NO₂ gas sensor using dielectrophoretic impedance measurement,” *Sens. Actuators, B* 108, 398 (2005).
- [158] S. MacNaughton, S. Sonkusale, S. Surwade, S. Ammu, and S. Manohar, “Carbon

- nanotube and graphene based gas micro-sensors fabricated by dielectrophoresis on siliconin,” Proceedings of the IEEE Sensors (IEEE, 2010), p. 894.
- [159] M. Nakano, M. Fujioka, K. Mai, H. Watanabe, Y. Martin, and J. Suehiro, “Dielectrophoretic Assembly of Semiconducting Carbon Nanotubes Separated and Enriched by Spin Column Chromatography and Its Application to Gas Sensing,” *Jpn. J. Appl. Phys., Part 1* 51, 045102 (2012).
- [160] S. Inoue, Y. Nanba, M. Nakano, and J. Suehiro, “Dielectrophoretic modification of carbon nanotube with ZnO nanoparticles for NO₂ gas sensingin,” IEEE Region 10 Annual International Conference, Proceedings/TENCON (IEEE, 2017), p. 3054.
- [161] H. Hayashi, M. Nakano, and J. Suehiro, “Detection of acetylene dissolved in insulation oil using pt-decorated ZnO gas sensor,” in IEEE Region 10 Annual International Conference, Proceedings/TENCON (IEEE, 2017), p. 1485.
- [162] K. Ellmer and R. Mientus, “Carrier transport in polycrystalline transparent conductive oxides: A comparative study of zinc oxide and indium oxide,” *Thin Solid Films* 516, 4620 (2008).
- [163] B. Ruhland, T. Becker, and G. Muller, “Gas-kinetic interactions of nitrous oxides with SnO₂ surfaces,” *Sens. Actuators, B* 50, 85 (1998).
- [164] A. Maiti, J. A. Rodriguez, M. Law, P. Kung, J. R. McKinney, and P. Yang, “SnO₂ Nanoribbons as NO₂ Sensors: Insights from First Principles Calculations,” *Nano Lett.* 3, 1025 (2003).
- [165] S. Maeng, S.-W. Kim, D.-H. Lee, S.-E. Moon, K.-C. Kim, and A. Maiti, “SnO₂ nanoslab as NO₂ sensor: identification of the NO₂ sensing mechanism on a SnO₂ surface,” *ACS Appl. Mater. Interfaces* 6, 357 (2014).
- [166] P.-M. Lee, C.-H. Liao, C.-H. Lin, and C.-Y. Liu, “Photocurrent generation in SnO₂ thin film by surface charged chemisorption O ions,” *Appl. Surf. Sci.* 442, 398 (2018).
- [167] K. G. Godinho, A. Walsh, and G. W. Watson, “Energetic and Electronic Structure Analysis of Intrinsic Defects in SnO₂,” *J. Phys. Chem. C* 113, 439 (2009).
- [168] J. Prades, J. Arbiol, A. Cirera, J. Morante, M. Avella, L. Zanotti, E. Comini, G. Faglia, and G. Sberveglieri, “Defect study of SnO₂ nanostructures by cathodoluminescence analysis: application to nanowires,” *Sens. Actuators, B* 126, 6 (2007).

- [169] Y. Porte, R. Maller, H. Faber, H. N. AlShareef, T. D. Anthopoulos, and M. A. McLachlan, "Exploring and controlling intrinsic defect formation in SnO₂ thin films," *J. Mater. Chem.* C4, 758 (2015).
- [170] M. Epifani, P. Siciliano, J. D. Prades, E. Pellicer, A. Cirera, J. R. Morante, E. Comini, G. Faglia, R. Scotti, F. Morazzoni, and M. Avella, "The role of oxygen vacancies in the sensing properties of SnO₂ nanocrystals," in *2008 IEEE Sensors (IEEE, 2008)*, p. 110.
- [171] J. Haeng Yu and G. Man Choi, "Electrical and CO gas sensing properties of ZnO-SnO₂ composites," *Sensors and Actuators B: Chemical*, 52 3, pp. 251-256 1998.
- [172] B. Mondal, B. Basumatari, J. Das, C. Roychaudhury, H. Saha, and N. Mukherjee, "ZnO-SnO₂ based composite type gas sensor for selective hydrogen sensing," *Sensors Actuators, B Chem.*, vol. 194, pp. 389–396, 2014, doi: 10.1016/j.snb.2013.12.093.
- [173] S. B. Rudraswamy and N. Bhat, "Optimization of RF Sputtered Ag-Doped BaTiO₃-CuO Mixed Oxide Thin Film as Carbon Dioxide Sensor for Environmental Pollution Monitoring Application," *IEEE Sens. J.*, vol. 16, no. 13, pp. 5145–5151, 2016, doi: 10.1109/JSEN.2016.2567220.
- [174] Q. Qi et al., "Electrical response of Sm₂O₃-doped SnO₂ to C₂H₂ and effect of humidity interference," *Sensors Actuators, B Chem.*, vol. 134, no. 1, pp. 36–42, Aug. 2008, doi: 10.1016/j.snb.2008.04.011.
- [175] A. Kolmakov, D. O. Klenov, Y. Lilach, S. Stemmer, and M. Moskovitst, "Enhanced gas sensing by individual SnO₂ nanowires and nanobelts functionalized with Pd catalyst particles," *Nano Lett.*, vol. 5, no. 4, pp. 667–673, Apr. 2005, doi: 10.1021/nl050082v.
- [176] T. Hyodo, Y. Baba, K. Wada, Y. Shimizu, and M. Egashira, "Hydrogen sensing properties of SnO₂ varistors loaded with SiO by surface chemical modification with diethoxydimethylsilane," 2000. [Online]. Available: www.elsevier.nl/locatersensorb.
- [177] Z. S. Hosseini, A. Mortezaali, A. Iraj Zad, and S. Fardindoost, "Sensitive and selective room temperature H₂S gas sensor based on Au sensitized vertical ZnO nanorods with flower-like structures," *J. Alloys Compd.*, vol. 628, pp. 222–229, 2015, doi: 10.1016/j.jallcom.2014.12.163.
- [178] P. T. Moseley, "Progress in the development of semiconducting metal oxide gas

- sensors: A review,” *Meas. Sci. Technol.*, vol. 28, no. 8, 2017, doi: 10.1088/1361-6501/aa7443.
- [179] A. Dey, “Semiconductor metal oxide gas sensors: A review,” *Mater. Sci. Eng. B Solid-State Mater. Adv. Technol.*, vol. 229, no. July 2017, pp. 206–217, 2018, doi: 10.1016/j.mseb.2017.12.036.
- [180] H. Gong, J. Q. Hu, J. H. Wang, C. H. Ong, and F. R. Zhu, “Nano-crystalline Cu-doped ZnO thin film gas sensor for CO,” *Sensors Actuators, B Chem.*, vol. 115, no. 1, pp. 247–251, 2006, doi: 10.1016/j.snb.2005.09.008.

Acknowledgements

First of all, I have to thank my research supervisor, Prof. Junya Suehiro, for his guidance, encouragement, and gracious support throughout my research. While I have studied at Kyushu University, I have many ideas since the first day that I became Prof. Suehiro's student, the academic things and everything of daily life in Japan from him. Thank you very much again.

I would like to thank Prof. Michihiko Nakano for valuable guidance and discussion in every step of my research. Moreover, some advice about how to survive as an academic professional.

I am also grateful to Asst. Prof. Masafumi Inaba for every support and helpful advice during the weekly seminar. Especially, the encouragement.

I would like to thank Prof. Kazunori Koga for being my dissertation committee.

I would like to thank Prof. Boonchai Techaumnat for recommendation to Prof. Suehiro and Prof. Nakano Laboratory, Kyushu University.

I would like to thank Kyushu Electric Power CO., INC, for financial support for this research project and fruitful discussion.

I would like to thank Mr. Xulin Liu and Mr. Kohei Miwa for my research team and our lab members.

I would like to thank the graduate program for power energy professionals (PEP) program organized by Waseda University for best practice and wonderful experience.

Especially, I would like to thank Royal Thai Government for full scholarship.

I would like to thank all the people who contributed somehow to work described in this thesis.

During three and half years, I have learned and lived in Japan, sometimes it takes me down, but every message from everyone that I get makes me feel better and move on.

Finally, I would like to acknowledge friends and family who supported me during my time here.

Nisarut Phansiri

29 June 2021